The application of advanced oxide scale failure diagrams to curved surfaces during high-temperature processing: a case study of conveyance tube manufacturing

KENDALL, Megan <http://orcid.org/0009-0009-6327-9321>, AUINGER, Michael <http://orcid.org/0000-0001-8726-6511>, TRUMAN, Christopher E and SACKETT, Elizabeth <http://orcid.org/0000-0002-5975-6967>

The Application of Advanced Oxide Scale Failure Diagrams to Curved Surfaces During High-Temperature Processing: A Case Study of Conveyance Tube Manufacturing

Megan Kendall [1,*], Michael Auinger [2], Christopher E. Truman [3] and Elizabeth Sackett [2]

[1] School of Engineering and Built Environment, Sheffield Hallam University, Howard Street, Sheffield, S1 1WB, UK; m.kendall@shu.ac.uk
[2] WMG, University of Warwick, Coventry CV4 7AL, UK; m.auinger@warwick.ac.uk
[3] School of Electrical, Electronic and Mechanical Engineering, University of Bristol, Queen's Building, University Walk, Clifton, Bristol, BS8 1TR, UK; c.e.truman@bristol.ac.uk
[4] Department of Materials Science and Engineering, Swansea University, Swansea SA1 8EN, UK; e.sackett@swansea.ac.uk
* Correspondence: m.kendall@shu.ac.uk

Abstract

Conveyance tube manufacturing is an energy-intensive process which promotes rapid surface oxidation of curved surfaces. Previous works used computational, experimental, and theoretical techniques to assess oxidation of curved surfaces. Fast, flexible computational predictions of oxide thickness can provide the continuous data necessary to generate a spatiotemporal stress profile for application to the high-level Advanced Oxide Scale Failure Diagram (**AOSFD**) developed in this work. To demonstrate the application of the **AOSFD** to conveyance tube normalisation, the oxide states after induction vs. gas-barrel heating were compared. Induction heating technology is an example of a current technological development in high-temperature steel processing which offers improved operational control and suitability for decarbonised steel processing. Current frequency control during induction heating decreases the resultant strain magnitude in the oxide thereby eliminating the compressive failure modes observed during gas-barrel heating. Higher-than-typical temperatures result in an increased tensile strain component, increasing interfacial failure probability during induction heating. However, the advantages of induction heating technology, in terms of oxide failure management, can only be achieved with sufficient electromagnetic design controls. This conclusion agrees with purely temperature-based studies of oxide failure, but the **AOSFD** approach accommodates the mechanical and kinetic phenomena of the oxide by combining diffusion and fracture mechanics analyses into a single diagram which is quick and simple to apply to industrial contexts which demand oxidation control on curved surfaces.

Keywords: oxidation; steel; heat treatment; modelling; geometric effects; advanced oxide scale failure diagram

Statements & Declarations

Competing Interests: The authors have no relevant financial or non-financial interests to disclose.

Funding Statement: This research was funded by COATED M2A from the European Social Fund via the Welsh Government (c80816), the Engineering and Physical Sciences Research Council (Grant Ref: EP/S02252X/1), and Tata Steel UK Ltd.

Data Availability Statement: Any additional data relevant to this article will be supplied in an associated repository.

TITLE PAGE

Acknowledgments: With thanks to Chris Owen, formerly at Tata Steel UK Ltd, for their assistance in sample acquisition. Electron microscopy was supported by the Advanced Imaging of Materials (AIM) core facility at Swansea University (EPSRC Grant No. EP/M028267/1) and the Welsh Government Enhancing Competitiveness Grant (MA/KW/5554/19).

Author Contributions: Conceptualization, M.K., E.S., and M.A.; methodology, M.K. and C.E.T.; software, M.K.; validation, M.K.; formal analysis, M.K.; investigation, M.K.; resources, C.E.T. and E.S.; writing—original draft preparation, M.K.; writing—review and editing, M.A., C.E.T., and E.S.; visualization, E.S.; supervision, M.A. and E.S.; funding acquisition, E.S. All authors have read and agreed to the published version of the manuscript.

1 Introduction and Background

1.1 Conveyance Tube Manufacturing

Curved surfaces and geometries are integral to the key shapes used in engineering [1] and are prevalent in several engineering applications involving high-temperature ‘fire-side’ oxidation during manufacturing, installation, and/or service, e.g., heating, ventilation, and air-conditioning (**HVAC**) systems and petrochemical transport, where high pressures, e.g., refrigeration, and temperatures, e.g., steam system, are possible [2]-[6]. The manufacturing process must be designed to achieve the material and mechanical properties necessary for these service conditions. A summary of the tube manufacturing process is shown in Figure 1, the full details of which have been discussed by Kendall et al [7]. During tube manufacturing, a multi-phase oxide, typically comprising 95% wüstite phase [8]-[12], grows on the outer tube surface at a rate aligned with standard linear-to-parabolic oxidation kinetics [12]-[16]. Kendall et al. demonstrated, using computational predictions of oxide thickness, that for thin-walled ($\boldsymbol{r_{wall}} \leq$ 5.4mm), hot finished conveyance tubes with an outer diameter, $\boldsymbol{OD}$, of less than 200mm, oxidation kinetics are sensitive to the radial term associated with cylindrical diffusion phenomena [7]. In Figure 1, $\boldsymbol{t}$ is equivalent to $\boldsymbol{r_{wall}}$.

Component damage and failure due to surface defects associated with phenomena such as oxidation has consequences, such as losses of up to 3% by weight occur due to scaling alone (equivalent to approximately 600 tonnes of feedstock loss per warehouse batch) [17]. There are also aesthetic implications due to either the compaction of oxide (‘scale’) on the substrate surface (‘rolled-in effect’) and/or the inadequate adherence of value-added coatings, e.g., anti-corrosion paint, and in-service surface performance problems [18]. The resulting inconsistent scale adhesion not only appears to give a poor surface finish but also may lead to complications for those customers who wish to apply additional paint or coat the tubes. Additionally, the constrained nature of oxide growth on non-planar geometries increases the resultant stress in the oxide, making damage and failure more likely [19]-[21]. Furthermore, scale removed either by descaling and/or spalling tends to disperse into the manufacturing environment, causing damage and contamination to product and plant alike via oxide particle entrainment and third-body abrasion [22]-[24]. However, it is a challenge for plants to optimise their processes to maximise product quality, capacity, process flexibility, and cost-effectiveness whilst high-temperature oxidation on curved surfaces is still poorly understood. Beyond the conveyance tube manufacturing process, there are several future steel-based technologies whose success will depend on adequate oxide control, e.g. electric arc furnace (**EAF**) steelmaking [25], hydrogen conveyance [26], and induction heating technology [27].

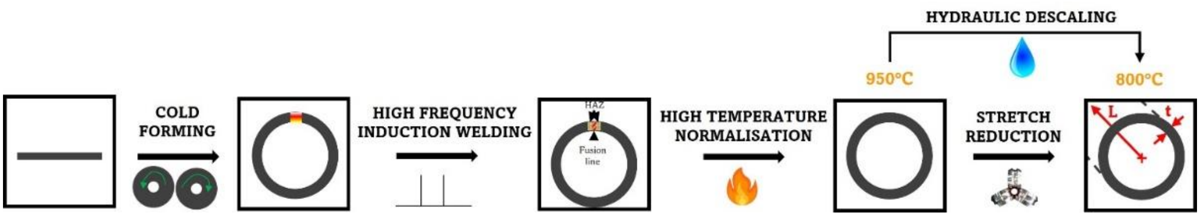

Figure 1.1: The schematic sequence of the conveyance tube-manufacturing process (figure reproduced from work by Kendall et al [7]).

1.1.1 Heating Technology Selection for Conveyance Tube Manufacturing

Normalisation, in the context of conveyance tube manufacturing, is typically performed by gas-barrel furnaces [17] with the gaseous alkane requiring no fuel preparation, ensuring good air-fuel mixing, and promoting a rapid combustion reaction. Normalisation demands a batch process so that soaking temperatures can be maintained for an extended period to ensure full microstructural homogenisation and internal stress relief [28]. The fast-evolving industrial world paradoxically demands higher product quality at a lower cost [29].

In the tube normalisation scenario, temperature is a key parameter, but high efficiency is also generally associated with minimised excess air and/or oxygen levels. This can be achieved by operating as close to the stoichiometric air-fuel mixture as possible. In addition to the air and fuel, reducing atmospheres can be introduced in scenarios such as tube manufacturing to minimise scale formation. Such an atmosphere can be generated via intentional sub-stoichiometric combustion to generate carbon monoxide, or via supply of special atmospheres such as hydrogen [30]. However, there are additional risks associated with these techniques including increased atmospheric toxicity and explosion risk respectively [31].

Furthermore, in the energy-intensive steel industry not only are the conventional gas-barrel reheat furnaces expensive energy consumers but also sources of material yield [32] and product quality [33]-[36] loss due to scale growth. Different reheating technologies have been considered to tackle environmental and economic issues associated with traditional fossil-fuel based combustion furnaces. Schluckner et al [37] explored both oxygen-enriched air-fuel (**OAF**) and oxy-fuel combustion (**OC**) processes designed to improve combustion efficiency via a reduction in flue gas losses and increase in maximum flame temperature via changes in partial pressures of oxidising species e.g., CO_2, H_2O, N_2 etc. Like Jang et al [16], they argue that previous studies were restricted on flow-chemistry interaction, temperature distribution, and scale formation details by the limitations of computational power accessibility. With the continued growth of computational power availability, Schluckner et al [37] proposed that there were now sufficient resources within workplace computers to fully consider the specifics of scale formation and how the atmosphere evolved (and the local concentration of individual atmospheric components) alters its kinetics and mechanisms e.g. ion diffusion. They demonstrated the importance of controlling the furnace atmosphere, via stack oxygen concentration, if scale kinetics is to be controlled.

Furnace atmosphere composition can vary significantly and Schluckner et al. [37] remark on the importance of considering furnace atmosphere and the effect of individual atmospheric component species. Abuluwefa et al. also conducted a two-part study [38], [39] investigating the effect of binary, ternary, and quaternary gas atmospheres on scale kinetics, morphology, and phase composition. When considering gas atmosphere alongside the issue of spalling effects, several studies have highlighted that the two are intrinsically linked [40], [41]. For example, both Basabe et al. [40] and Sheasby et al. [41] demonstrated the correlation between higher levels of water vapour and increased adhesion due to increased scale plasticity and creep [10] which could ultimately reduce the number of parabolic oxidation-inhibiting scale-steel gaps evolved i.e. **SSI** adhesion was prolonged. Hence why despite the effect of manufacturing parameters, such as atmospheric composition, once scale integrity is compromised, its own effects will control oxide behaviour, especially kinetics [37], [42].

Furthermore, stricter safety regulations will be incurred by the increased upper flammability limit associated with increased oxidisability within the furnace atmosphere. Hence, application of combustion technologies discussed by Schluckner et al. [37] during conveyance tube manufacturing is confined to pre-heating stages which do not reach oxidising temperatures (T < 750°C [37]) so that the faster heating properties can be exploited without creating a high-temperature scale-favouring atmosphere.

However, controlled atmosphere furnaces are expensive and induction furnaces, which can achieve accelerated heating at a lower cost and higher efficiency [43], are the favoured potential development in conveyance tube manufacturing and broader decarbonised steel industry goals [25], [29], [44]. Unver et al [43], highlight several advantages to induction technology as a proven technology in metal production. These include reasonable maintenance costs, compact installation, localised heating capacity i.e. higher energy efficiency, product purity via vacuum or inert atmosphere-based working, and, on average, higher heating efficiency (dependent on material) [43], [45], [46]. The ability to precisely regulate heating conditions, via control of electrical (e.g. current frequency), thermal (e.g. cooling conditions), and geometric (e.g. coil geometry) input parameters, is a key advantage of induction technology in scale management efforts (provided electrical load capacity [47] and magnetic shielding [48] demands can be met) [49]. However, work has not been performed on the effect of changing from gas-barrel to induction heating, specifically that of accelerated heating and atmospheric differences, on oxidation kinetics and adhesion, with the exception of Krzyzanowski and Beynon [50] who simulated induction heating by stipulating a time and space function fixed temperature boundary condition at the steel-scale interface (**SSI**).

Zhao et al explored the effect of variable pipe wall thickness on the heating efficiency of induction heating used for heat treatment of pipes for thermomechanical applications [36]. They emphasise that soak times using induction heating are susceptible to extension by the need to achieve a uniform heat distribution throughout the pipe section under the action of the induction coil. This could undermine the time-saving qualities of induction heating highlighted by Unver et al [33]. Zhao et al also argue that non-uniform heating could also lead to loss of heating efficiency and workshop capacity, increase in energy consumption and ultimately delay progress in automated production in large-scale manufacturing processes [36]. Although they focus on the microstructural consequences for the steel, changes to soak time have already been shown to affect oxide kinetics and adhesion, as well as the effect of adhered oxide scale on thermal emissivity and absorption [10], [42], [51]. They highlight that the complex interaction of electromagnetic and heat transfer phenomena during induction heating results in a strong influence of the induction coil by: shape (the oval coil as the best for achieving uniform magnetic flux distribution), current (adjustments to both density and frequency), air gap (a narrower air gap will promote faster temperature rise), and component feed rate (a faster feed will improve temperature uniformity across the component). They also highlight the challenge of a narrow processing window in controlling temperature distribution, which also applies for the conveyance tube manufacturing process at only ~15 mins [52]. Two key assumptions by Zhao et al [36] were made which would be invalidated by the presence of oxide scale when compared to conveyance tube manufacturing. Firstly, fluctuations in workpiece density were neglected. Secondly, constant workpiece emissivity was assumed. Neither of these assumptions are true when an oxide scale dynamically forms on the workpiece [10], [16], [40], [53]. However, since coil geometry is designed to match a specific product specification, it is possible that the effect of oxide scale could be incorporated into future coil design and electromagnetic parameters, for components such as steel tubes. Furthermore, the anticipated changes in average density are not large compared to tube wall thickness in an industrial process context and can therefore be reasonably ignored.

Overall, Zhao et al [36] used a finite element approach to demonstrate that increasing the current from 3000A to 5500A can increase heating efficiency and in turn reduce heating time by a factor of four, using an equal or variable cross-section coil. However, they remarked on the limitations of benefits beyond the Curie temperature where an unavoidable loss in magnetic permeability reduces the heating rate. However, increasing current has a negative impact on heating quality, with large difference in temperature exhibited by the inner and outer walls on the pipe (up to 12.5% and 14.2% using 5500A on a variable and equal cross-section coil respectively). In the variable cross section coil, this difference resulted in a 50°C 'overshoot' in the temperature of the higher wall thickness part, whilst the thinner wall thickness part simultaneously failed to reach the target temperature range. Although conveyance tubes do not have a variable wall thickness once the manufacturing process is complete, the effect of coil cross-section geometry shown by Zhao et al is still relevant when considering the stretch reduction process used to alter wall thickness, as well as the wide range of tube dimensions, manufactured i.e. resulting air gaps. Dynamic power control is a potential solution and Drobenko et al [49] argue that models for ferromagnetic materials undergoing high temperature induction heating should account for the temperature dependence of material properties (particularly electrical conductivity) and elastic-plastic deformation, and non-linear dependencies of magnetic properties [49]. For a thermo-sensitive, ferromagnetic, long, cylindrical solid under high temperature induction heating, they numerically predicted temperature, electromagnetic field parameters, and deformation. One use of their approach was to ensure a predefined residual stress level by minimising the heat treatment duration. Residual stresses were partially controlled by electric current frequency (the other control function being related to cooling conditions) varied in the range 0.05-8kHz. This is an example of dynamic power control, a technique also employed by Zhao et al to manage overheating of thinner wall thickness sections of their variable cross-section pipe [36].

Overall, electric current frequency has a non-linear relationship with the time taken to reach the target temperature (970°C) [49]. For example, Drobenko et al demonstrated that increasing the frequency from 0.3kHz to 0.8kHz decreases the time taken to heat the tube surface region to target temperature from 15.5s to only 1s. Hence, an appropriate selection of electric current frequency will aid in minimising the heating period within the allowable residual stress limits. Their study demonstrated that, for a maximum allowable residual stress of 100MPa, the maximum allowable electric current frequency is 530Hz. Assuming that the tubes in Drobenko et al's study are scale-free and not subjected to any external mechanical stresses from manufacturing, the maximum allowable residual stress stipulated can be set equivalent to the thermally induced stress component during conventional gas-barrel heating.

However, all studies cited neglected to address Torres et al.'s [10] original adhesion-related assumptions of perfect scale-substrate contact and absence of microstructural defects. Another key assumption in Torres et al.'s study was plastic behaviour of the steel and scale above 560°C. This is an acceptable assumption based on the dominance of plastic wüstite and magnetite but Abuluwefa et al. [39] argue that magnetite is brittle and prone to spalling, and that variations in furnace atmosphere which affect phase composition could also alter heat transfer. A brittle magnetite model was used to apply worst case scenario strains and hence the steepest thermal gradients. Overall, differences in approach often stem from a difference in investigative focus, e.g. Abuluwefa et al. [39] consider only the effects of furnace atmosphere on scale whereas Torres et al. [10] consider heat transfer and its interaction with specific phase composition at a given temperature (scale, steel, and environmental). Therefore, microstructural integrity and material deformability are key considerations during adhesion considerations within this work.

1.1.2 Oxide Failure During Conveyance Tube Manufacturing

There are five (I-V) stages of oxide degradation comprising oxide mechanical failure (I), healing by continuing reaction (II), protective potential plateau (III), surface crack initiation and/or material consumption (IV), and crack propagation and/or accelerated material consumption (V - end-of-life) [54]. Overall, the steps described highlight how the cycle of failure and repletion of oxide scale will eventually be exhausted as the substrate subsurface zone becomes depleted below critical oxidation levels. Further oxidation can then induce surface crack growth and material consumption to an extent that the load-bearing cross-section is decreased. Oxidation can also assist crack propagation and accelerate material consumption which ultimately leads to component failure [54]. Hence, oxidation is as much a problem mechanically as it is kinetically and once an oxide has reached stage III without a sufficient material design reservoir, the component is no longer suitable for safe operation.

1.1.2.1 Industrial Impact

It was highlighted in 1.1 that losses of up to 3% by weight occur during conveyance tube manufacturing due to oxidation alone. Therefore, not only does a reduction in material loss contribute to business operations impact including improved product quality, faster process speed, extended plant and product life, and decreased process cost, but also has a further reaching impact on the success of manufacturing operations adversely affected by oxidation. Conventionally, the delaminated oxide from downstream steel manufacturing operations is collected in a crucible [9] and returned to the start of the steelmaking process for reduction in the blast furnace to recover the steel content [9]. However, blast furnace technology is being decommissioned [55] in line of decarbonisation goals [25], [29], [44], and replaced with electric arc furnace (**EAF**) technology, a technology which depends on steel scrap and slag rather than iron ore (oxide) [56]. Furthermore, whilst oxide scale is a suitable raw material for blast furnace-based steelmaking, the role of scale as an oxidiser during **EAF**-based steelmaking is made redundant by the introduction of oxygen lancing technology which achieves large electrical energy savings [57]. Disposal of scale into landfill also carries risk of heavy metal leaching into soil and groundwater [57]. Therefore, the waste associated with oxidation will no longer be readily recyclable and oxidation kinetic and adhesion control will aid in reducing steel waste in the absence of the conventional recycling process.

Oxide adhesion control could reduce, or potentially eliminate, the need for additional resources to process spalled oxide and repair associated damage to plant tooling. De Oliveira Junior et al. showed how the entrainment of iron oxide particles could increase counter-body wear rate (assuming the

conveyance rolls used are harder than the conveyance tubes themselves) by 65% and 15% when considering haematite and magnetite respectively [22]. Vergne et al. later addressed wüstite, as the dominant oxide phase formed on low carbon steel work rolls, but highlighted that cubic oxides exhibit greater ductility and a lower contribution to abrasion, which is prominent when oxide particles become entrained in the tube-roll contact and enable third-body abrasion [23], [24]. Hence, a reduction in oxide brought about by a change in parameters informed by an **AOSFD**, since thicker oxides have a greater negative impact on roll wear rate by dispersing more spalled oxide particles into the environment to become entrained in the tube-roll contact, will contribute to plant life extension. Dubar et al.'s recent study also highlights the need to consider the effect of oxide at the workpiece-tool interface during manufacturing operations [58] in terms of its effect on forming conditions, contact pressure (they observed a potential reduction of 40%), material flow, and thermal conditions.
Furthermore, Dubar et al. [58] highlighted how oxide scale could improve contact pressure distribution owing to the wear-changes in geometry. For example, convex surfaces see a greater increase in oxide thickness, compared to flat and concave surfaces, near the end of tool life but also showed a 23% drop in contact pressure, compared to 30% and 10% for flat and concave surfaces respectively. This is reflective of the conclusions of Kendall et al.'s work [7], that geometry is a critical parameter affecting oxide kinetics and mechanics and directly impacts manufacturing operations such as conveyance tube production.
Induction heating technology has been identified as a suitable technology for decarbonised steelmaking during high temperature operations, such as normalisation within conveyance tube manufacturing. However, the manufactured conveyance tubes will also contribute to new decarbonisation-friendly technologies when in service. A key example for a conveyance tube context is the introduction of hydrogen into energy infrastructure [44]. Current research in this area includes the need to assess existing steel infrastructure for its suitability for hydrogen conveyance [26], [59], [60]. Understanding oxide kinetics and adhesion is considered an integral element of protecting conveyance infrastructure steels from hydrogen permeation and embrittlement [61], [62] as hydrogen diffusion through an iron oxide is approximately eight times slower than steel [63], [64]. This work can contribute to this technology shift by offering an insight into oxidation kinetics and oxide mechanics specifically for curved surfaces, and at the accelerated rate required via the use of computational resources as discussed.
Finally, Stylidis et al. argue that the greatest commercial advantage is reached by capitalising on the customer quality perception [65]. Although spalled oxide does not affect the mechanical strength of the tube products, it creates a perception of reduced product quality and safety in service, as it is proposed that perception of incident severity carries more weight than perception of incident probability [66], [67]. Furthermore, Cai et al. cite perceived risk concerning safety, reputation, aesthetics, and performance as key considerations during customer purchase [68], all of which are shown to be negatively impacted by oxide scale and its inconsistent spalling profile.

1.1.2.2 Failure Mechanisms

Broadly, oxide failure can be assigned to one or more of the following categories tensile (+) or compressive (-) state categories: through-thickness cracking (+), interfacial separation (+/-), buckling (-), crack deflection (-), spalling (-), and shearing (-) [69].
Imbrie and Lagoudas [70] hypothesise that for the oxidation of a solid cylinder surface, short oxidation times yield a compact, well-adhered scale, similar to that observed on a 1D planar sample, i.e. curvature has no effect. However, longer oxidation times (>18hr) generated deviation of the cylindrical geometry from the flat plate. The compact layer thins as its boundary at the **SSI** moves towards the **SGI** and a porous, layered oxide structure is left in its wake. In the case of conveyance tubes, which are thin-walled tubes rather than solid cylinders, the **SSI** already has proximity to the **SGI** so is already thinned and affected by the evolution of pores. Therefore, surface curvature cannot be neglected in thin-walled cases, even if the radial curvature is large and/or oxidation time is short.
Unlike planar specimens, failure is most often observed as radial cracks with the circumferential cracks associated with **SSI** failure more likely attributed to cooling. The details concerning failure are summarised in Krzyzanowski and Beynon's study of oxide failure during tensile loading for two different grades of mild steel [50]. A transition temperature exists where the separation stress for the oxide scale overtakes its oxide-metal interface counterpart, i.e. oxide cohesion is greater than oxide-metal adhesion and failure mode transitions from Mode I to II accordingly. Mode I failure described by

Krzyzanowski and Beynon, albeit for planar surfaces [50], is associated with a higher adhesive strength between the substrate and scale than the cohesive strength of the oxide itself. This is in contrast with flat plate specimens where failure is more often observed as Mode II, i.e. longitudinal cracks due to SGI failure and the higher cohesive strength than adhesive strength. This supports anecdotal industrial observations where oxide formed during ultra-high temperature processing operations, e.g. hot rolling at >1200ºC, fails as large sheets [71], suggesting higher levels of ductility and cohesion, whereas spalled oxide from the lower temperature conveyance tube manufacturing process forms more brittle, disparate particles [17], [72], suggesting more brittleness and less cohesion.

Oxidation introduces two additional interfaces for consideration: the steel and scale interface (**SSI**) and the scale and tool interface (**STI**). As previously discussed, scale deformation, fracture, delamination, and spalling, are partially caused by the mechanical loading evolved during stretch reduction. However, once the metal substrate is exposed by scale spalling, the thermomechanical scenario is altered again as tool-metal contact leads to increased friction and heat transfer [73], [74].

When considering hot strip rolling, Jiang et al. [75] developed a finite element analysis (**FEA**) model of the surface asperity profiles of both the steel and scale before rolling and hypothesised that complete scale failure under the shear friction imposed by scale-roll contact (modelled by a modified Coulomb law) would proceed via a raft sliding mode [118] due to the absence of the weakest planes associated with the three-phase layer and scale-steel interfacial weakness at high temperatures. Also, additional added-value protective and/or aesthetic coatings, e.g. galvanic, polymer [76], are often applied to conveyance tubes at the end of the manufacturing line which introduces a further interface between the scale and coating (**SCI**). These coatings will be less robust if adhered to a failure-prone oxide layer rather than the steel substrate [17].

Given the strong influence of porosity level on scale failure mode, Krzyzanowski and Beynon [74] reasoned that the individual phase layers within the scale, and the potential for their interfaces to be mode II failure sites (see Figure 1.21), should be considered separately. Differences in porosity and crystal morphology were observed and attributed to inward oxygen transport and metal cation diffusion dependency respectively [77], with the inner layer containing many uniformly distributed pores whilst the outer layer was notable for its larger, less equiaxed crystals. The inner-outer layer interface was proposed as a potential delamination site [74].

This sort of failure was observed in non-homogeneous scales formed above 1150°C, with evidence of a much more porous (up to 1mm void) and thicker spalled outer layer. The inner layer was minimally porous and well-adhered even after large strain application at this temperature. It was at lower temperatures (<850-900°C) that mode I failure was observed in all scale thicknesses and morphologies. Thus, initially brittle mode I scale failure is defined by Linear Elastic Fracture Mechanics (LEFM), assuming small defects, and brittle phenomena. As temperature increases, ductile mode II failure is observed and defined by stress distribution and interfacial cohesion strength, before differences at a phase level led to mode II-style failure at the inner-outer scale layer interface beyond 1150°C. In their assessment of steel grade composition effects, Krzyzanowski and Beynon [74] provide further evidence for these effects, and for the need for further work focusing on quantitative relationships between failure mode transition and the deeper understanding of slipping mechanism at the delamination zone (**SSI** or otherwise) as a physical basis for micro-modelling [50].

The effect of strain was highlighted by the fact that higher temperature, thicker, and higher strain rate scales delaminated more than their lower temperature, thinner counterparts, even if they were less homogenous. This demonstrated that ultimately, temperature, strain, and strain rate were the most influential parameters when defining how scale cracking, slipping, and adherence. Lee et al. [78] comment that, although spalling is attributed to the fracture of the **SSI**, the process is accelerated by microstructural damage and the related influence of several factors including deformation dimensions, e.g. bending curvature (or wall thickness change in the conveyance tube application context), volume fraction, residual stress, defect dimensions, e.g. porosity diameter, crack length, scale thickness, and interfacial roughness. Kalasin et al. [79] looked specifically at the adhesion behaviour and surface quality of the thinner and less pure scales evolved on Electric Arc Furnace-heated (**EAF**) low carbon rolled steel samples and, crucially, did not assumed a defect-free scale microstructure. Mechanical adhesion testing revealed transverse cracking followed by complete localised spalling, with thicker slabs showing a lower spalling ratio and, although they proved that scale thickness was independent of slab thickness, this was not the case for adhesion phenomena.

Krzyzanowski and Beynon also highlighted, in their computational hot rolling model [50], that temperature-dependent functions are the only way to acquire accurate information about transient axisymmetric metal-scale flow, viscous sliding, and failure in tension. Crucially, their approach couples the macro-model of the external mechanical loading with the micro-model of scale failure to reveal how the former influences the latter. However, they also emphasised the importance of the consideration of the thermal behaviour of the **SSI**, citing the 10-15 times lower thermal conductivity of scale compared to steel as a source of **SSI** weakening at high temperatures leading to fracture and slipping phenomena defined by interfacial cohesive and adhesive strengths and stress distribution. Lee et al's scale failure map demonstrated how an increased scale thickness can trigger wedging failure solely due to internal growth and thermal stresses, therefore thicker scales are associated with a weaker interface (due to higher internal stresses) and more pre-bending fracture [78]. Thus, oxide descalability must account not only for the external loads which evolve during TMP, but also the scale's own natural tendency to spall due to the thermal and growth stresses which depend on manufacturing parameters. Matsuno et al. [77] specifically explored the impact of growth (oxidation) stress on descalability during a high-temperature hydraulic descaling operation. However, during descaling, water pressures only reached 15% of those used in industry, and for a much shorter seconds-long period. More attention could be paid to the effect of fully industrial scale-up and its effect on scale behaviour, utilising the scope available via a computational approach [7], [80]. However, they were still able to show how blister formation, which precedes spalling, occurs in a defined temperature-time envelope which can be expanded, thus increasing the likelihood of spalling, by application of mechanical (high-pressure water) or thermal (cold shock) stress. However, it was highlighted that blistering (when not caused by gas-based processes such as decarburisation) still occurred prior to the introduction of thermal stresses, i.e. oxidation stress must ultimately control blistering. Matsuno et al. suggested that oxidation stress puts adhered scale into a state of compression which generates the blister and subsequent plastic deformation of the detached scale drives blister growth. Whilst the former is easy to prove given the high plasticity of wüstite at high temperatures [10], spalling is more complex. Early hypotheses suggested oxidation stress-induced wüstite plastic slip generates clefts between slipped scales and the steel, leading a loss of **SSI** contact and blister-initiating pores. However, scale-steel adhesion is also clearly important and shown to be dependent on temperature and scale thickness. In particular, Hulley and Rolls' [81] conclusion of cohesive strength being three times higher than adhesive strength supports Krzyzanowski and Beynon [50] comments regarding the temperature-critical transition of scale failure mode from cracking to spalling where interfacial weakening means scale cohesive strength is dominant. Ultimately, Matsuno et al. also proposed that oxidation stress is the dominant cause of adhesive failure within the combined effect of stress and adhesion vs. cohesion strength dominance, since temperature will accelerate oxidation and cause greater compressive volume dilatation [77]. The effect of such mechanisms, alongside thermal effects and manufacturing-induced stress, are considered in this work.

1.1.2.3 Mechanical Causes of Failure

It has been established that, aside from the mechanical state of the substrate itself [82], simultaneous high-temperature oxidation and manufacturing processes will generate stresses in the oxide due to thermal deformation, mechanical loading, and growth stress due to oxidation itself [4]. Huntz and Schütze highlight that determination of residual stress at room temperature does not provide much information about the stress state of the system at oxidation temperature [83]. Furthermore, they highlighted the need to distinguish between evolved growth, $\boldsymbol{\sigma_{ox,g}}$, and thermal, $\boldsymbol{\sigma_{ox,T}}$, stresses, which are often dealt with separately [83]. This is important as they argue that experimental data reveals that stresses generated by oxidation are dominated by thermal stress (see Equation 7.1) and the majority of spalling occurs during cooling, as well as stress relaxation via microcracking (fast cooling) or creep (slow cooling). Furthermore, Samal and Mitra also highlight that any measured stress associated with adhesion analysis is not equivalent to true adhesion stress due to the residual compressive stress in the oxide associated with the thermal expansion differential between the substrate and scale [84]. Including the thermal stress in the resultant stress state of the oxide is therefore essential to obtain an accurate value. The continuous data from Kendall et al's model [7] also allow an insight into the instantaneous stress state of the oxide across its entire thickness during growth.
For a low oxygen solubility scenario as is found in austenitic steels in conveyance tube manufacturing

[85], the oxide will develop a compressive growth stress as it increases in volume compared to the substrate [86]. This is true provided that the oxide grows at the interface so that stress cannot be relaxed by movement of the free surface [86]. This is the case for curved surfaces. It has already been highlighted that such stress, when it exceeds the critical value for buckling, plays an important role in oxide spalling phenomena which plague tube manufacturing (although it should be noted that, at high temperatures, oxides with a yield stress lower than their buckling stress are more likely to fail via relief by plastic flow) [20], [87]-[89]. Although in situations where oxide formation on the outermost surface of the free layer favours stress relaxation by accommodating volumetric changes normal to the free surface, even in this case the presence of macroscopic and/or microscopic curvature will induce stress. Furthermore, for curved surfaces, even with an unconstrained free surface, the introduction of new oxide between the metal and existing oxide, leads to stresses and strains at the surface radii as the metal retreats, as it is consumed by oxidation, and loses contact with the existing oxide. In other words, any surface curvature (where the minimum ratio between the grain size and surface curvature is 1:20 [90]) will inhibit the oxide from following volume changes in the oxidising substrate, leading to elastic and creep deformation [20].

Lee et al. [78] comment that shear interfacial stress has previously been ignored but demonstrated its relevance by showing how inflections within high-frequency roughness were dominated by the shear stress component. Krzyzanowski and Beynon [50] agree that a critical shear stress value, and its transmission from the substrate to adherent scale, was responsible for transition scale sliding from a viscous to frictional mode. Again, this demonstrates the complexity of the mechanical situation of the **SSI**. Also, although it was agreed that roughness-free interfaces were also stress-free, this is an unrealistic scenario in practice where constant interaction with mill conveyance equipment will inevitably incur roughness. Furthermore, both Lee et al. [78] and Noh et al. [91] found that thicker scales experienced lower normal interfacial stress due to a reduction in longitudinal stress attributed to increased proximity to the zero-strain neutral axis of bending. However, inspection of industrial data by Lee et al. [78] revealed the opposite phenomenon, i.e. increased spalling for thicker scales. Whilst this could be a stress-related phenomenon, it was attributed to the assumption of defect-free scale [92].

Although in-situ experiments are possible, Huntz and Schütze also emphasise that several factors can promote data scatter, namely oxidation conditions, oxide thickness, substrate initial surface condition, impurities (type and concentration), and microstructural features. Furthermore, tensile strains are anticipated when it is recognised that oxygen diffusion is a non-negligible phenomenon which generates compressive stress at the metal-scale interface. Experimental methods for determining stress state are limited by the equipment's geometric and thermal limitations as ideally the selected method would be capable of through-thickness measurements at high temperatures. Few techniques can satisfy all these requirements. Clarke also highlighted that typically successful methods used to directly measure growth stress or strain, namely cantilever beam deflection and X-ray diffraction (**XRD**) respectively, encounter significant uncertainties in key mechanics and materials parameters, e.g. linear coefficient of thermal expansion [89]. These include measurement uncertainties, variations across the sample as well as interplay in lattice expansion as a function of temperature and pressure (local stress state), when employed to determine growth stress [89]. Furthermore, if high temperature predictions are based on extrapolation of ambient measurements, in addition to parametric uncertainties, it is near-impossible to account for stress relaxation during cooling in the form of diffusional creep and intra-oxide plastic deformation (regardless of whether the substrate thickness is great enough to prevent its own plastic deformation, and even this technique is limited in the cantilever beam technique by the need to minimise thickness to achieve observable deflection) [90]. The global data which can be provided from the Thermo-Calc© computational domain [7], including the interfacial and bulk states, offer a more accurate insight into the stress state of the metal and/or oxide during heat treatment and how likely this is to lead to the failure and damage described above.

1.1.2.4 Advanced Oxide Scale Failure Diagrams

The current state of the art highlights the complexity of the causes and mechanisms of oxide failure, often considering them in separate studies. It is therefore difficult to perceive how a manufacturing change, such as heating technology change from gas-barrel to induction, will affect oxide behaviour during industrial processes such as conveyance tube manufacturing. In this work, the impact of the

high level of electromagnetic control available using induction heating technology is quantified using an Advanced Oxide Scale Failure Diagram (**AOSFD**). The continuous oxide thickness gain data necessary to generate this diagram, and the necessary stress analysis, are available via Kendall et al's validated predictive computational model of oxidation of curved surfaces [7], [80], [89], [90].
Advanced Oxide Scale Failure Diagrams (**AOSFD**s) were identified as crucial in accounting for not only the critical strain for different oxide scale failure mechanisms (covered by Oxide Scale Failure Diagrams (OSFDs)), but also the considerable impact of physical defects (pores, cavities, and microcracks). Schütze summarised much of this failure information in an Advanced Oxide Scale Failure Diagram (**AOSFD**) relating failure mechanism susceptibility based on strain, $\boldsymbol{\varepsilon}$, and defect size, $\boldsymbol{c}$, and operation parameter, $\boldsymbol{\omega_{o,\phi}}$, where $\boldsymbol{\phi}$ reflects the specific failure mode described. Schütze highlighted that the mechanical properties of an oxide scale refer to all the parameters which characterise its cohesion, adhesion, and deformation [93]. However, at high temperatures especially, failure analysis of oxide cannot be limited to conventional elastic (elastic and shear modulus, Poisson ratio) and plastic/creep (ductile-brittle transition temperature, stress-strain and stress-strain rate relationships) properties. Analysis should ideally include oxidation-related properties which characterise pseudoplasticity associated with simultaneous brittle microcracking and continuous healing via oxidation. Hancock et al also highlighted the need to consider fracture mechanics phenomena within their works on oxide stability and failure [94], [95]. To perform this analysis, oxidation-related properties comprise the distribution and orientation of physical defects (at the metal-scale interface or within the scale), interface geometry, and scale fracture toughness [69]. The change in temperature across the normalise-cool cycle ($\boldsymbol{\Delta T_{norm} - \Delta T_{cool}}$) is too large to neglect temperature effects on elastic modulus. Schütze [69] highlighted the need to select an appropriate level (1, 2, 3…$\boldsymbol{n}$) of **AOSFD** to reflect the impact of relevant parameters. A higher-level diagram is associated with a greater number of parameters with a high level of impact on scale failure probability and mode [69].

2 Methodology

The theory presented below is appropriate for a 'Level 3' **AOSFD** which can incorporate the high impact parameters of conveyance tube manufacturing into a comprehensive operation parameter, $\boldsymbol{\omega_{o,\phi}}$, for assessing the failure of wüstite. Poisson ratio is unlikely to change during conveyance tube manufacturing so is a low impact parameter favouring a Level 1 or 2 **AOSFD**. However, oxide scale fracture toughness will have temperature dependency since the tube normalisation temperature is above 600°C [69]. Chemical composition is less problematic if there is no oxide lattice structure or composition change but this is not the case during tube manufacturing where there is a heat treatment with a temperature high enough to cycle the steel between its ferritic (BCC) and austenitic (FCC) states [69]. Therefore, it becomes necessary to apply the full operation parameter ($\boldsymbol{\omega_0}$) concept and a level 3 **AOSFD** is required.
The computational oxide thickness gain data obtained in Kendall et al's work [7] for a 15 **n.b.** sample, and its derived parabolic rate coefficient, can be used to predict the exact oxide thickness, due to its continuous nature, after the average normalisation soak time of 180s. As a result, a 1s resolution is sufficient for this application where heating periods are at least minutes, or often hours, long [73]. Linear interpolation was used, with a window of 3 datapoints, to increase the resolution of the **SSI** position where a mathematical description was not possible [96]. This increased resolution data set can also be used to improve the **AOSFD** precision.
There is a critical strain energy achieved at a certain extent of scale deformation which is sufficient for separation along the scale-metal interface i.e. critical spallation strain $\boldsymbol{\varepsilon_c^s}$ [50], [93]. This critical value is a function of the scale thickness, $\boldsymbol{\delta_{ox}}$, and the scale-metal interface fracture energy, $\boldsymbol{\gamma_o}$. However, since metallographic preparation challenges make it challenging to eliminate surface roughness [75], [78], [91], interfacial fracture energy must be modified to account for the height, $\boldsymbol{r}$, and length, $\boldsymbol{\lambda}$, of the oxide roughness, $\boldsymbol{\gamma_r}$ (see Equation 2.1 and Equation 2.2 – note that $\boldsymbol{E_{ox}}$ should be given in GPa for the latter equation).

$$\frac{1}{\varepsilon_c^s} = \omega_{o,s} = \left(\frac{\delta_{ox} \cdot E_{ox} \cdot (1 - v)}{2\gamma_r}\right)^{1/2}$$

Equation 2.1

$$\gamma_r = \gamma_0 \left(1 + \frac{0.1 E_{ox}}{2\gamma_0} \frac{r}{\lambda}\right)$$

Equation 2.2

Buckling is anticipated to precede through-thickness cracking i.e. spallation, a conservative buckling criterion, ε_c^b, introduces the initial radius of the zone of local decohesion, R_{dec} (see Equation 2.4). Observation of local decohesion, characterised by small regions of elastic debonding between the metal and oxide, precedes buckling for an oxide layer under compression [97]. R_{dec} is defined by Equation 2.3 and depends of several mechanical properties of the oxide including elastic modulus, E, Poisson's ratio, v, critical fracture toughness, K_{Ic}, and tensile strength, σ_{UTS} [98]. The latter parameter is challenging to measure for brittle ceramics. However, wüstite exhibits plasticity at high temperatures [10], [40], [41]. σ_{UTS} was evaluated using Hidaka's high-temperature tensile data [99] and assigned a maximum value of 5MPa for temperatures greater than 1000ºC. This yielded R_{dec} values in the order of 10^{-3}mm, which is in line with the order reported by Sabau et al [100].

$$R_{dec} = \frac{\pi}{8} \frac{E}{1 - v^2} \frac{K_{Ic}}{{\sigma_{UTS}}^2}$$

Equation 2.3

Initiation of through-thickness crack deflection, ε_c^{cd} from the interface towards the scale surface can follow buckling and precede spallation. There is an alternative criterion based on the assumption that plastic oxide yield strength, σ_Y, is 10% of its elastic modulus ($\sigma_Y \approx 0.1 E_{ox}$).

$$\frac{1}{\varepsilon_c^{b/cd}} = \omega_{o,b} = \omega_{o,cd} = \frac{1 - v^2}{k_{\omega_o}} \cdot \left(\frac{R_{dec}}{\delta_{ox}}\right)^2$$

$$\left(k_{\omega_{o,b}} = 1.22\ for\ buckling, k_{\omega_{o,cd}} = 3.75\ for\ crack\ deflection\right)$$

Equation 2.4

Interfacial cracking is another precursor to spallation when there is stress (compressive or tensile) acting on an interfacial defect-containing system in the direction parallel to the scale-metal interface and at the interfacial location with peak roughness amplitude. Equation 2.5 uses a local tensile stress intensity factor, i.e. fracture toughness, K_{Ic}, based on the half-length of the critical defect, c, and geometrical parameter, f^*, and highlights how a thinner scale with greater surface roughness and smaller defects can tolerate greater compressive strain before failure.

$$\frac{1}{\varepsilon_c^{if}} = \omega_{o,if} = \frac{f \cdot (\pi c)^{1/2}}{K_{Ic}} \cdot \frac{2E}{(1 + r/\delta_{ox}) \cdot (1 + v)}$$

Equation 2.5

Finally for compressive scenarios, the case of shear stress (see Equation 2.6) is relevant if it is necessary to take an actual stress situation into account at failure initiation site i.e. spalling as a result of stress components evolved from a physical defect being in a shear stress situation like at an oxide grain boundary or dislocation movement plane and also that the defect is large enough to reduce the shear failure criterion to a value that preceded interfacial failure [69]. Although ultimately dependent on shear orientation, a good approximation is $\sigma = \tau\sqrt{3}$ (61). Crucially, the most conservative criterion can be obtained using shear deformation fracture toughness, K_{IIc} or K_{IIIc}, if available, otherwise the K_{Ic} value gives the least conservative criterion. As a non-stoichiometric compound [101], wüstite shear response is defect-driven [102] and therefore sensitive to temperature and partial pressure [103]. Wüstite also exhibits high-temperature plasticity [10], [40], [41] making plastic shear deformation more likely than pure brittle sliding [104]. Therefore, shear response is challenging to isolate and measure [105]. Accurate and precise shear fracture toughness evaluation therefore requires extensive diffusion measurements [26] and successive microstructural observations [106] constituting an entirely separate study which is beyond the scope of this work.

$$\frac{\mathbf{1}}{\boldsymbol{\varepsilon}_{\mathbf{c}}^{sh}} = \boldsymbol{\omega}_{o,sh} = \frac{\mathbf{2}\boldsymbol{K}_{\mathbf{Ic}}}{\boldsymbol{f}\boldsymbol{E}_{\mathbf{ox}}\sqrt{\boldsymbol{\pi}\boldsymbol{c}}}$$

Equation 2.6

Tensile failure analysis is simpler by comparison and based on a conventional fracture mechanics (see Equation 2.7). Oxide fracture toughness is calculated either based on crack geometry (see Equation 2.8) or oxide surface fracture energy (see Equation 2.9).

$$\frac{\mathbf{1}}{\boldsymbol{\varepsilon}_{\mathbf{c}}^{t}} = \boldsymbol{\omega}_{o,t} = \frac{\boldsymbol{f}\cdot\boldsymbol{E}(\boldsymbol{\pi}\cdot\boldsymbol{c})^{1/2}}{\boldsymbol{K}_{Ic}}$$

Equation 2.7

$$\boldsymbol{K}_{\mathbf{I}} = \boldsymbol{\sigma}_{\mathbf{if}}\sqrt{\boldsymbol{\pi}\boldsymbol{c}}\boldsymbol{f}$$

Equation 2.8

$$\boldsymbol{K}_{\mathbf{Ic}} = \sqrt{\mathbf{2}\boldsymbol{\gamma}_{\mathbf{0}}\boldsymbol{E}_{\mathbf{ox}}}$$

Equation 2.9

It should be noted that individual failure modes may combine under certain loading conditions and some failure modes, such as interfacial cracking, can exist in both tensile and compressive stress states [107]. The standard 15 nominal bore (**n.b.**) tube investigated had an outer diameter, $\boldsymbol{OD}$, of 21.9mm and wall thickness, $\boldsymbol{r}_{wall}$, of 3.0mm. The operation parameters, $\boldsymbol{\omega}_{\mathbf{0},\boldsymbol{\phi}}$, encompass the oxide thickness gain, $\boldsymbol{\delta}_{ox}$, dataset when the 15 **n.b.** tube was heated to 1000°C for 22 hours (the maximum period before the entire tube wall thickness of steel was consumed) [69]. Table 2.1 outlines the parameters used to develop a level 3 **AOSFD** for oxidation during conveyance tube manufacturing. The composition of the conveyance tube grade steel and the oxide formed at typical normalisation temperatures is identical by that used in previous author works [7], [80]. It is noted that although a curved geometry is present, which will change the contact dimensions of the spalled section of oxide, the dimensions of the spalled section are negligible compared to the overall radius of the tube (<0.2% in the 15 **n.b.** tube case for mean oxide thickness, $\overline{\boldsymbol{\delta}}_{ox}$, vs. inner radius, $\boldsymbol{IR}$, where the inner radius is 7.5mm). For example, even if the entire section of oxide visible in a x1000 magnification field emission gun electron microscopy (**FEGSEM**) image (using an accelerating voltage of 12 kV and a probe current of 8 nA) were delaminated (which has not been observed to be the case in this work), the arc length, $\boldsymbol{L}_{frame}$, 116.8±3.4μm, for the sample shown in Figure 2.1, for a segment of that size would only subtend an angle, $\boldsymbol{\theta}$, of 0.90±0.03° (see Figure 2.1). The calculations of the values in Table 2.2 are based on **FEGSEM** image analysis using Equation 2.11 [108] and Figure 2.1. The mean arc length of spalled oxide, $\boldsymbol{L}_{spall}$, based on measurements at locations A, B, and C, at equidistant locations around the sample (see in Figure 2.1), was 21.8±0.6μm, which is only a fifth of the mean arc length of oxide per microscope frame.

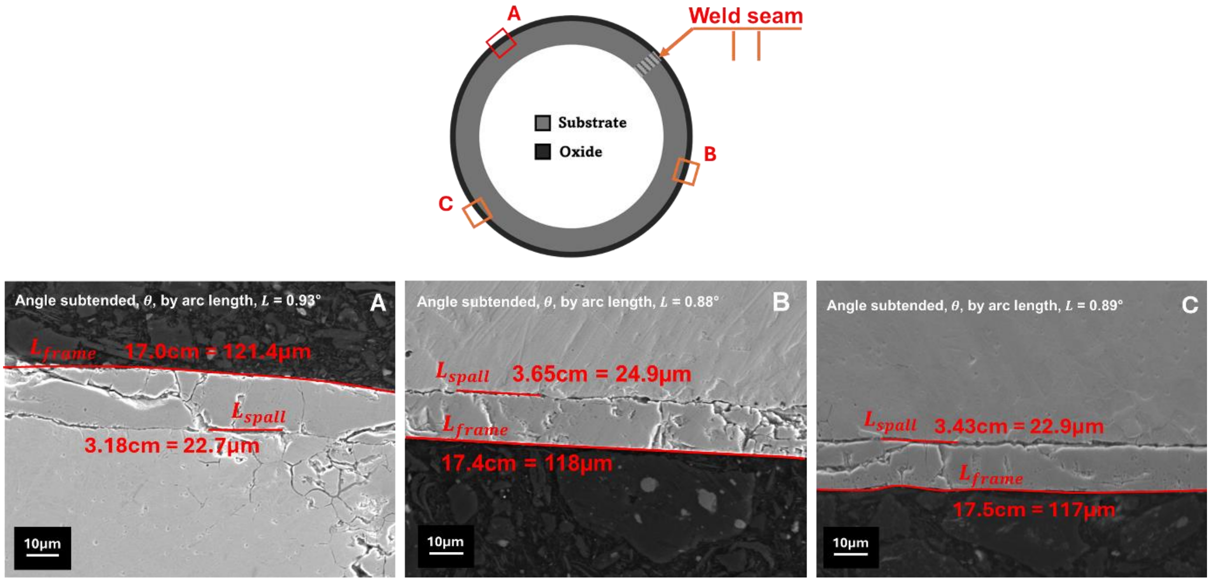

Figure 2.1: Measurement of typical radius of decohesion, $\boldsymbol{R_{dec}}$, at three different circumferential locations on a 15 nominal bore (**n.b.**) post-normalised tube.

The through-scale cracking equation represents the depth of the defect, $\boldsymbol{c}$, so is analogous to the oxide thickness [41]. Murakami's stress intensity factor handbook was used to determine the necessary geometric values for "a circular ring with a radial crack under external tension or internal pressure" [109]. To obtain an initial estimate for defect size, $\boldsymbol{a}$, its value was set at 10% of the instantaneous scale thickness, based on visible cracks during field emission gun scanning electron microscopy (**FEGSEM**) imaging. Since the geometric parameter is determined via an empirical graph relating the ratio $\frac{a}{r_i}$, and radial ratio, $\boldsymbol{\beta} = \frac{r_o}{r_i}$, the worst case scenario value was used, i.e. maximum geometric factor when $\boldsymbol{r_i}$ is minimised and the crack dimension, $\boldsymbol{a}$, is maximised (at maximum oxide thickness) where $\boldsymbol{r_o}$ is dependent on the instantaneous oxide thickness. This yielded a geometry factor, $\boldsymbol{f^*}$, of 0.95, which could then be used in Griffith's fracture theory [110] (see Equation 2.10) to determine the minimum initial defect size under an applied stress to propagate. Even under the minimum possible stress (from a thermal source), the estimated initial defect size was greater than this minimum value.

$$\boldsymbol{a} = \frac{1}{\pi}\left(\frac{K_{Ic}}{f^*\sigma}\right)^2$$

Equation 2.10

The porosity volume fraction, $\boldsymbol{p}$, contributes to the calculation of the high impact, temperature-dependent parameter elastic modulus, $\boldsymbol{E_{ox}}$, which has been measured in the literature [50], [111], [112]. Porosity volume fraction was set at 25% in line with the results of porosity volume assessment of optical micrographs of samples of oxide grown in lab conditions (see Appendix 2). Micrographs were assessed using the open source image processing software, ImageJ [113]. Each image was converted to its **RGB** form and split into its constituent channels to select the highest quality image. Each image was cropped into smaller sections to improve accuracy and a mean porosity value of 25.040% was obtained for the wüstite phase across the 5 samples (as only wüstite phase in the model) and ignoring 'pull-outs' (anomalously large pores) associated with metallographic preparation and transit damage. This value of porosity agreed with Sabau and Wright's estimation [41]. However, estimations of porosity in wüstite vary between 10 and 44% [41], [114]-[116] and this range of values was also observed during the porosity volume assessment for this work (see Appendix 2).
The overall objective of Schutze et al.'s AOSFD framework is to provide a fuller description of oxide tolerance against mechanical straining via different failure types by incorporating parameters into the

critical failure strain which oxide thickness cannot provide. That is, the state of the oxide accounts for additional operational parameters such as the temperature dependence of mechanical properties e.g. elastic modulus, coefficient of thermal expansion. At level 3, this dependence is expanded e.g. an equation to incorporate porosity into estimations of elastic modulus. This work seeks to build on the level 3 framework by incorporating Schutze's suggestions for higher level models. For example, porosity, amongst other microstructural defects e.g. grain boundaries, carbide dispersion, can be incorporated into the Thermo-Calc© model used to predict oxide thickness [7]. Adaption of this diffusion coefficient often requires knowledge of grain boundary volume fraction, grain size, diffusing cation valency, and carbide volume fraction. Diffusion is then fundamental in defining kinetic response and oxide thickness therefore the AOSFD is elevated to level 4 and beyond.

Within the use of this thickness data, and the calculation of other parameters, consideration is given to the effect of geometry. Furthermore, by using Griffiths fracture mechanics theory to calculate defect size based on specifically selected geometry factors and material specific properties (tensile strength), the failure mode can be made geometry specific and is again elevated to level 4 and beyond. Finally, this work not only seeks to create an AOSFD, but also to demonstrate how it can be applied to save resources when making technology changes to active manufacturing processes. As previously stated, the factors affecting oxide failure, and its impact on manufacturing, are numerous and interlinked but often considered in separate studies. This work aims to demonstrate how the AOSFD can bring together these complexities into a single tool which quickly assesses the estimated stress state associated with a manufacturing process (whether that be assessed analytically e.g. solid mechanics, experimentally e.g. XRD, or computationally, FEA) against critical failure strain to predict failure mode and effects in applied scenarios.

Table 2.1: Definition of parameters used to construct an Advanced Oxide Scale Failure Diagram (**AOSFD**) for wüstite on a curved surface. Fields marked with an asterisk (*) are geometrically dependent and require revision if the tube sample is changed. Each parameter is assigned a numerical level in accordance with those defined by Schutze et al. [69].

Parameter	Value (for wüstite on a curved surface)	Units	Level
$\boldsymbol{K_{Ic}}$	0.9	$MPa.\sqrt{m}$	4
$\boldsymbol{f^*}$	0.95	-	3
$\boldsymbol{c}$	$\boldsymbol{\frac{1}{\pi}\left(\frac{0.9}{0.95\sigma}\right)^2}$	m	4
$\boldsymbol{E_{ox}}$	133	GPa	3
$\boldsymbol{v_{ox}}$	0.36	-	3
$\boldsymbol{\delta_{ox}}$	≤200	μm	4+
$\boldsymbol{R_{dec}}^*$	$\boldsymbol{\frac{\pi}{8}\frac{E}{1-v^2}\frac{K_{Ic}}{\sigma_{UTS}^2}}$	μm	3
$\boldsymbol{\gamma_0}$	3	$\mathrm{J.m^{-2}}$	3
$\boldsymbol{r}$	14.3μm	μm	3
$\boldsymbol{\lambda}$	143μm	μm	3

Table 2.2: Arc length of spalled oxide, ***L_{spall}***, measured on the outer edge of three 15 nominal bore (**n.b.**) conveyance tube samples normalised in industry (Tata Steel UK Ltd). The radius of decohesion, ***L_{spall}***, is therefore 21.8±0.6μm. The ratio between the mean oxide thickness, ***δ_{ox}***, are also presented to show the overall

arc length of the oxide captured in the electron micrograph frame, L_{frame}, and the angle subtended, $\boldsymbol{\theta}$, by the total thickness of oxide captured in each frame.

Location	$\overline{\delta}_{ox}$ (μm)	$\frac{\overline{\delta}_{ox}}{IR}$	L_{frame} (μm)	θ (°)	L_{spall} (μm)
A	16.6	0.002	121.4	0.93	22.7
B	14.5	0.002	115.6	0.89	21.6
C	13.5	0.002	113.3	0.87	21.2

$$\boldsymbol{\theta} = \frac{\mathbf{360}\boldsymbol{L}}{\mathbf{2}\boldsymbol{\pi}.\boldsymbol{IR}}$$

Equation 2.11

Interfacial scale separation energy, $\boldsymbol{\gamma_0}$, was calculated using first principles of Coulombic potential and crystal face orientation described by Robertson and Manning [93], [117]. Surface topography data were previously collected during previous White Light Interferometry (WLI) studies on tube-grade steels performed by Grant [17]. Grant noted that previous research has shown that high temperature treatments can enhance surface roughness by several hundred percent [78], [100], [118]. Oxide surface roughness length, $\boldsymbol{\lambda}$, is typically 10 times the oxide roughness amplitude, $\boldsymbol{r}$, for oxide formed on low carbon steel samples investigated by Noh et al [91] and Lee et al [78] in controlled gas atmosphere furnaces. However, the roughness amplitude is still low enough to make decohesion radius evaluation valid (see Equation 2.3) [98].

The Thermo-Calc© oxide kinetic model developed by Kendall et al [7] contributes at several stages of defining the **AOSFD**. The geometrical parameter, $\boldsymbol{f}^*$, is dependent on (i) the ratio of the defect size, $\boldsymbol{c}$, and **SSI** position and (ii) $\boldsymbol{\beta}$, the ratio of the **SGI** and **SSI** positions [109]. A methodology for calculating these positions was developed Kendall et al [7]. The scale thickness itself, $\boldsymbol{\delta_{ox}}$, with a normalising value, $\boldsymbol{\delta_{ox_0}} = \mathbf{1}\boldsymbol{\mu m}$ [69], was also determined from the Thermo-Calc© model data [7]. Finally, mode I fracture toughness, $\boldsymbol{K_{IC}}$, is a material constant quoted from the literature [19], [93].

2.1 Quantifying Stress in the Oxide

The stress state in the oxide comprised thermal, growth, and manufacturing sources, based on discussions by Huntz and Schutze [83]. A summary of the values of stress and strain evolved during conveyance tube normalisation is given in Table 2.3 and the full details of each source of stress are described and analysed in Appendix 1 including their conversion to strain values using Equation 7.12. However, it should be noted that stress characterisation of each of these phenomena is an area of research in its own right and the purpose of this paper is not to provide a comprehensive stress analysis of oxide during conveyance tube manufacturing but to demonstrate the framework for applying dynamic oxide thickness from a non-planar geometry to a higher level **AOSFD** to allow informed manufacturing decisions for heating technology which mitigate the failure impact of oxidation. Thermal stress was calculated numerically using Equation 7.1 [83], whilst analytical solutions in Equation 7.10 and Equation 7.11 were used to calculate growth stress (11). Manufacturing-induced stress was evaluated using the X-ray diffraction (**XRD**) data from pre-normalised samples to account for the combined effect of the forming and stretch reduction operations within conveyance tube manufacturing. The maximum permissible stress criterion defined by Drobenko et al. [49] was selected as a realistic value of thermal stress induced in the oxide as their numerical simulation worked with a low carbon steel tube with appropriate dimensions for conveyance tube applications ($\boldsymbol{OD}$ = 110mm, $\boldsymbol{r_{wall}}$ = 5mm) to a temperature (1050ºC) in the same range as presented in this work. The current frequency used to achieve this stress value, out of those investigated by Drobenko et al.[49], also offered the best temperature distribution across the tube wall thickness, allowing localised thermal variation phenomena to be neglected. Additionally, the **XRD** data used to validate this work and determine residual stress yield stress of a similar order (see Appendix 1).

Table 2.3: Comparison of gas-barrel ('gas') and ('ind') and induction heating methods for normalisation in terms of their effect on stress, $\boldsymbol{\sigma}$, and strain, $\boldsymbol{\varepsilon}$, components evolved from oxidation- (thermal and growth) and manufacturing- (forming and drawing) related sources.

Stress Source		$\boldsymbol{\sigma_{gas}}$ **(GPa)**	$\boldsymbol{\sigma_{ind}}$ **(GPa)**	$\boldsymbol{\varepsilon_{gas}}$ **(-)**	$\boldsymbol{\varepsilon_{ind}}$ **(-)**
Oxidation-induced	Thermal	-13.11	-0.10	-0.0988	-0.0008
	Growth	0.62	0.62	0.0047	0.0047
Manufacturing-induced	Forming	-0.09	-0.09	-0.0007	-0.0007
	Drawing				

Overall, the compressive thermal stress observed is due to the higher coefficient of thermal expansion of the steel substrate, allowing it to contract a greater rate and place any adhered oxide under compression. In contrast, the tensile nature of the oxide growth stress reflects the formation of new oxide underneath the existing surface oxide as the oxidation reaction proceeds. Using linear superposition [119], the resultant strain in the oxide can be calculated to be -0.0948 and 0.0032 for the gas-barrel and induction heating cases respectively. These values are used in the **AOSFD**.
It should be noted that, throughout this paper, '2D' refers to the consideration of the two dimensions (radial, $\boldsymbol{r}$, and circumferential, $\boldsymbol{\theta}$) of the tube cross-section [3], [5], [26], [45], [120] as opposed to 2D oxidation phenomena [121]-[124].
Wüstite creep response is a driven by a diffusion-controlled recovery mechanism [102], thereby making it sensitive to temperature and partial pressure [103]. Evaluating constants for even the most fundamental creep expression, e.g. Norton's law [125], therefore requires diffusion measurements and successive microstructural observations [106] which constitute an entirely separate study beyond the scope of this work. The complexity of wüstite's creep response means it is often neglected from mechanical models [100], [126] and where empirical measurement of wüstite's high-temperature creep response has been achieved [106], [127], the reported contribution of creep stress (<20MPa) represents only a fraction of the total stress (~10GPa) experienced during high-temperature deformation, therefore minimising the effect of any potential overestimation within this work. Finally, in this work the length of heat treatment (~15mins) is not sufficient for the onset of plasticity to cause significant relaxation [127]. However, the authors recognise that this is a limitation of this study, and an avenue for further work in the field.

2.2 AOSFD Validation

Samples of 15 nominal bore (**n.b.**) P235GH conveyance tubes ($\boldsymbol{OD}$ = 21.9 mm, $\boldsymbol{r_{wall}}$ = 3.0 mm, $\boldsymbol{L}$ = 25 mm) in an as-welded and post-normalised state were supplied by Tata Steel UK Ltd. The possible range of conveyance tube dimensions is wide depending on intended service application [36], but using the 15 **n.b.** sample allowed for unrestricted movement within the furnace work tube's 90 mm inner diameter and was suitable for conventional 30–32 mm diameter mounting moulds and scanning electron microscopy sample holder limits. Samples were mounted transversely in electrically conductive thermosetting resin (Bakelite). It was anticipated that oxidised samples may experience embrittlement, delamination, and spallation due to thermal stresses evolved during resin thermosetting. Consequently, the oxidised sample was therefore mounted in cold-setting resin before mounting in Bakelite to reinforce the oxide integrity during subsequent mechanical metallographic preparation. The fully mounted sample was ground to 1200 grit using silicon carbide (SiC) grinding paper and then polished using 50 nm colloidal silica solution, which was sufficient to reveal the substrate and scale microstructure without the need for chemical etching. Imaging was performed using optical light microscopy on Zeiss Primotech (Jena, Germany) and field-emission gun scanning electron microscopy (**FEGSEM**) where the optimal settings were an accelerating voltage of 12 kV and a probe current of 8 nA. The industrial samples were compared with the samples generated as part of the authors' previous work demonstrating the methodology for an electromagnetic, air-based normalisation replication cycle in a Carbolite Gero Ltd. (Hope Valley, UK) high-temperature **TGA** tube furnace (model TF1 16/100/450) in the Simulation and INtegrity Testing in Extreme Conditions (SINTEC) laboratory within the Steels and Metals Institute (SaMI) at Swansea University [80]. These data act as a representation of induction heating due to the absence of combustion elements. As industrial samples can only be provided for the actual manufacturing process, i.e. normalisation at 1000ºC, laboratory samples are only made for 1000ºC. The laboratory samples were prepared and analysed using the same methodology as for the industrial samples.

3 Results and Discussion

For most failure modes, an increase in the operation parameter (by only increasing oxide thickness) leads to a decrease in the critical failure strain (see Figure 3.1 and Figure 3.2). Buckling and crack deflection are an exception to this trend as the reciprocal nature of the oxide thickness term $\left(\frac{1}{\delta_{ox}^{2}}\right)$ in their governing equation means that the greatest value of operation parameter is associated with the thinnest oxide (see Equation 2.4). The mathematical trend in critical failure strain change is dependent on the failure mode and its associated governing equation but for all failure modes the majority of change in critical failure strain occurs at $\boldsymbol{\omega_{0,\phi} \leq 100}$. Figure 3.2 highlights how even by constraining the thickness to only the extent grown during normalisation, i.e. maximum 4 minutes of heating at 1000°C, very low critical failure strains are predicted for buckling and/or crack deflection failure. This is again due to the exceptional nature of Equation 2.4 which predicts a higher critical failure strain for thinner scales, in direct contrast to all other failure modes. Figure 3.3 plots the same critical strain values against only oxide thickness gain highlights the same trends. However, all interpretations of the data (Figure 3.1 and Figure 3.3) highlight how the probability of oxide failure increases dramatically during the first 5 mins of normalisation as the critical failure strain in most failure modes decreases rapidly. Conversely, the probability of oxide failure by buckling and/or deflection is highest when the oxide is thinnest.

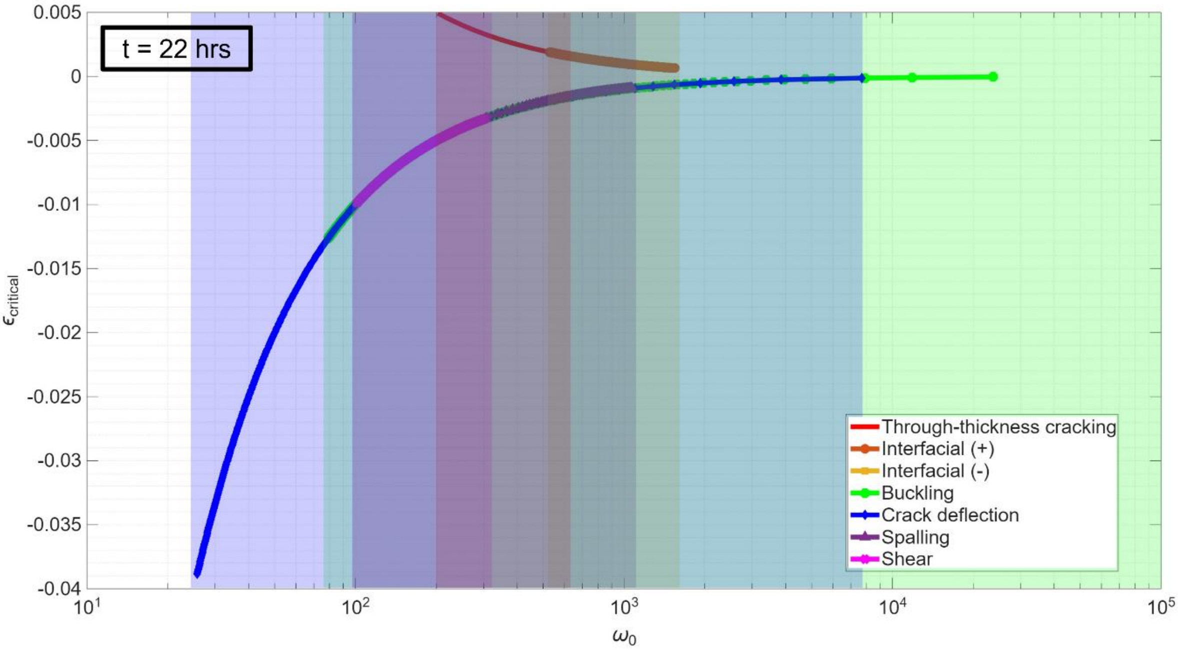

Figure 3.1: Advanced Oxide Scale Failure Diagram (critical failure strain, $\varepsilon_{critical}$, against failure mode-based, $\boldsymbol{\phi}$, operation parameter, $\boldsymbol{\omega_{0,\phi}}$) for a 15 nominal bore (**n.b.**) conveyance tube after normalisation using the full range of oxide thicknesses predicted, heated for 22 hours at 1000°C, by the Thermo-Calc© model developed by Kendall et al [7].

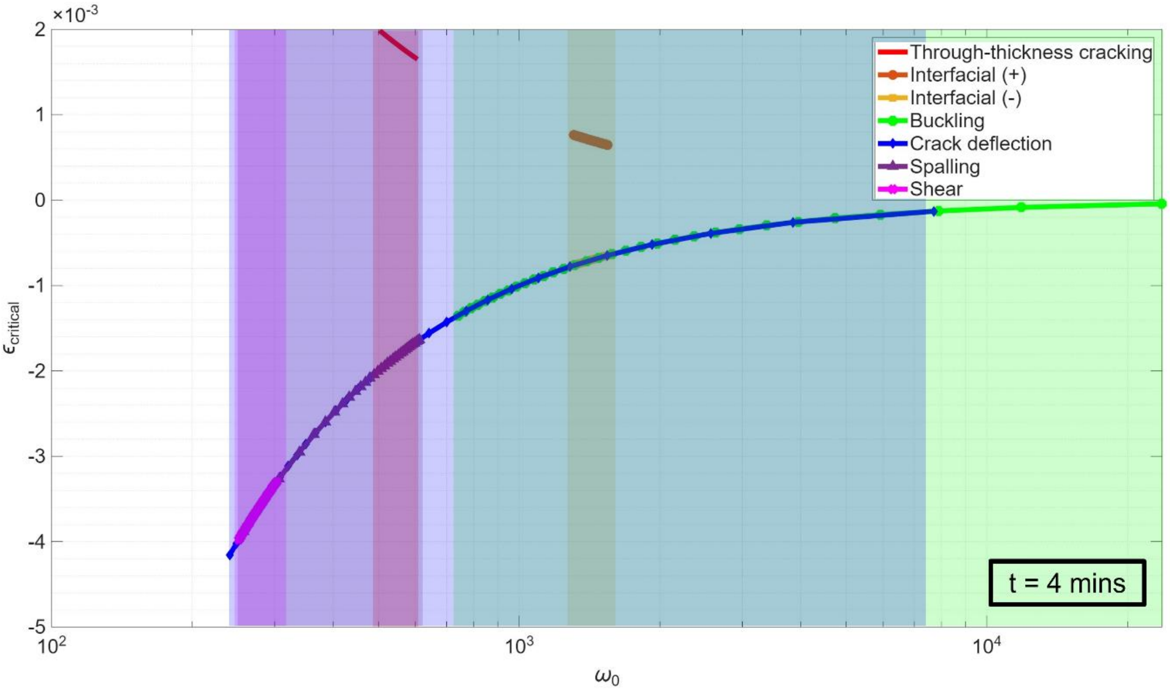

Figure 3.2: Advanced Oxide Scale Failure Diagram (critical failure strain, $\varepsilon_{critical}$, against failure mode-based, $\boldsymbol{\phi}$, operation parameter, $\boldsymbol{\omega_{0,\phi}}$) for a 15 nominal bore (**n.b.**) conveyance tube after normalisation using the full range of oxide thicknesses predicted, heated for 4 minutes at 1000°C, by the Thermo-Calc© model developed by Kendall et al [7].

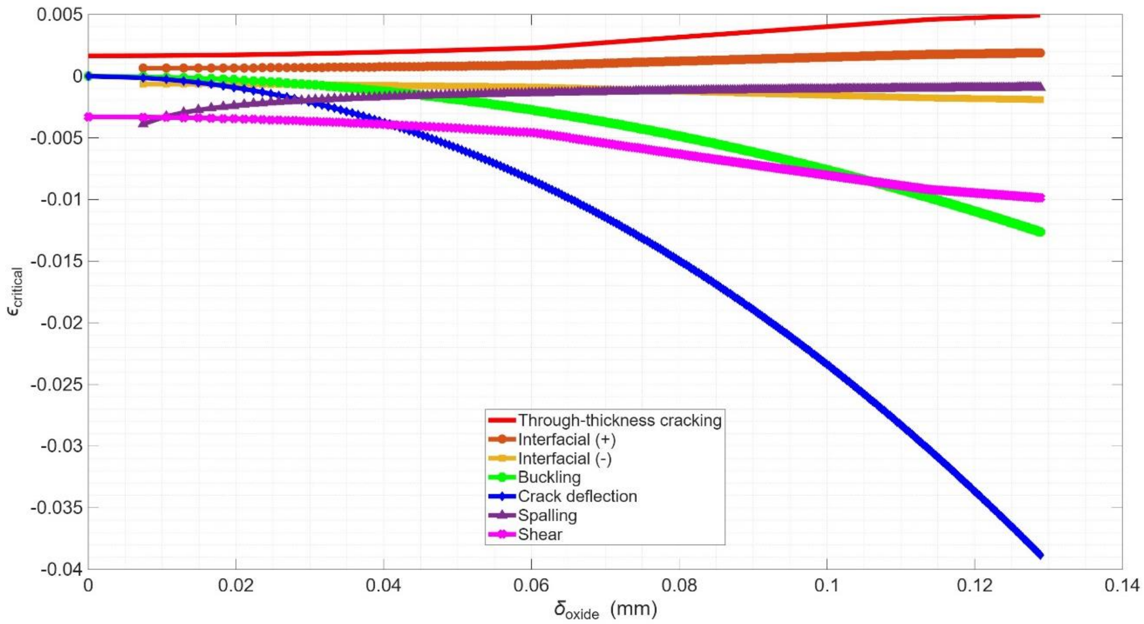

Figure 3.3: Plot of critical failure strain, $\boldsymbol{\varepsilon_{critical}}$, against oxide thickness, $\boldsymbol{\delta_{ox}}$, for a 15 nominal bore (**n.b.**) conveyance tube after normalisation up to the oxide thickness gain associated with normalisation heat treatment (99.7μm after 4 mins) predicted, at 1000°C, by the Thermo-Calc© model developed by Kendall et al [7].

Figure 3.1 also shows how the datasets for each failure mode vary greatly in range for both critical failure strain and operation parameter. The governing equations for the operation parameter, and subsequently critical failure strain, of each failure mode are independent of each other and dependent on different mechanical parameters in addition to oxide thickness. Not only is a mathematical operation applied to oxide thickness data to obtain the abscissa but also the ordinate value range. Each equation varies in terms of the mathematical operation applied to oxide thickness, e.g. raised to a half power for interfacial cracking (see Equation 2.5) vs. the reciprocal of its square for buckling and crack deflection (see Equation 2.4). Hence, even for the same range of oxide thicknesses assessed, each failure mode analysis will map the operation parameter on to the critical failure strain in a different manner. It is recognised that the most comprehensive study would investigate the relationship between oxide thickness and every other parameter used in each failure mode assessment. However, obtaining data sets for such a wide range of parameters is beyond the scope of this work whose focus is the application of dynamic oxide thickness data from computational modelling of curved surface oxidation, and the associated data generated from it, to assess failure modes and effects.

Aside from general trends concerning how the likelihood of failure changes as oxidation proceeds, the **AOSFD** can also offer insight into the effect of changes in oxide stress state, due to manufacturing operation history changes such as the transition from gas-barrel to induction heating technology, on the likelihood and mode of failure. Table 3.1 presents the critical strains for each failure mode for a ~100μm scale when strain is at the level associated with gas-barrel vs. induction heating. The critical strains calculated for each failure mode account for the entire operation parameter history during the formation of a specific thickness of oxide scale. This serves to further highlight how certain failure modes, namely shear, buckling, and crack deflection, are eliminated by transitioning to fully induction-based heating technology. Figure 3.4 highlights the presence of several compressive failure modes, namely shear cracking (1A, 1C, 2A, 2C, 3A, 3B, 3C), buckling (2B, 2C, 3A, 3B), crack deflection (1A, 1C, 2A, 2C, 3A), and spalling (1A, 1B, 2B, 3C), on all industrial samples. There is also limited evidence of interfacial failure but this is more likely with lower levels of strain than estimated during conveyance tube manufacturing (see Table 3.1).

Table 3.1: Comparison of strain, $\boldsymbol{\varepsilon}$, evolved in a ~100μm oxide scale formed using normalisation with gas-barrel ('gas') vs. induction ('ind') heating, to critical strain ('crit') for each potential failure mode.

Failure Mode	$\boldsymbol{\varepsilon_{crit}}$ **(-)**	$\boldsymbol{\varepsilon_{gas} \geq \varepsilon_{crit}}$**?** **(**$\boldsymbol{\varepsilon_{gas}}$ **= -0.0948)**	$\boldsymbol{\varepsilon_{ind} \geq \varepsilon_{crit}}$**?** **(**$\boldsymbol{\varepsilon_{ind}}$ **= 0.0032)**
Buckling	-0.0140	✓	x
Crack deflection	-0.0431	✓	x
Interfacial cracking	-0.0025	✓	N/A
(Tensile or compressive)	0.0025	N/A	✓
Shear	-0.0041	✓	x
Spalling	-0.0011	✓	✓
Through-thickness cracking	0.0020	✓	✓

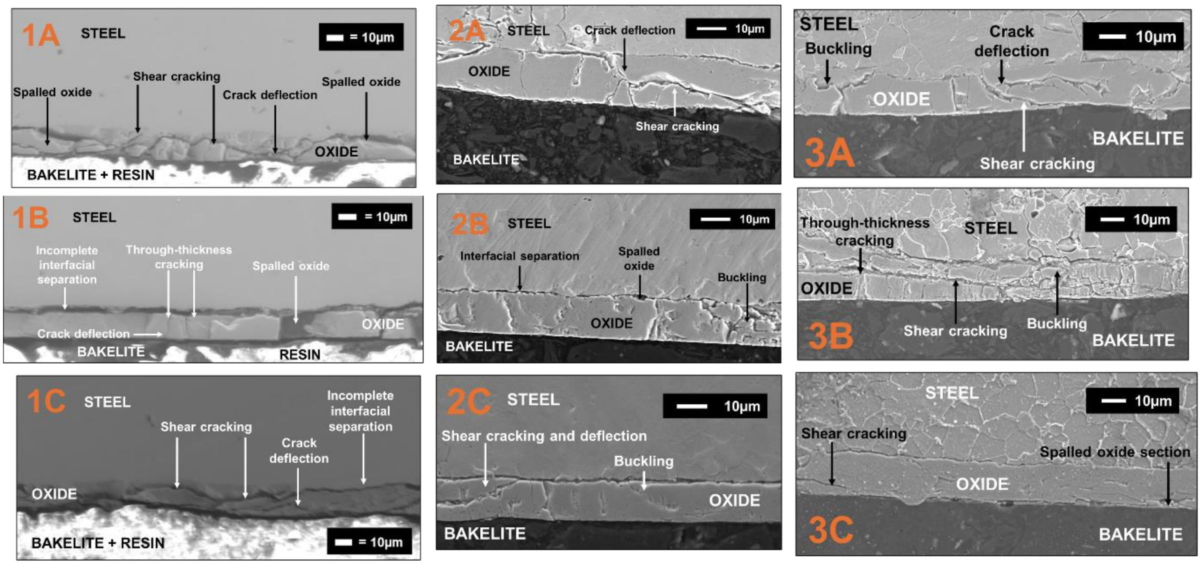

Figure 3.4: Annotated field emission gun scanning electron micrographs for three (1-3) 15 nominal bore (**n.b.**) conveyance tubes after their complete manufacturing process. Key manufacturing process steps include normalisation at 1000°C for 15 mins and hydraulic descaling. Oxide images were taken at three approximately equidistant locations around each tube circumference (A-C).

The oxide thickness gain predicted by Kendall et al's Thermo-Calc© model after 180s at 1000°C is 99.7µm [7]. Figure 3.6 demonstrates how an **AOSFD** can be used to predict how this specific oxide thickness is likely to fail after gas-barrel vs. induction heating. Crucially, the transition from gas-barrel to induction heating, and the increased process control associated with the latter technique, leads to a transition in the oxide from a compressive to tensile state, as well as a 30-fold decrease in strain magnitude (see Figure 3.6). As a result, compressive failure modes like spalling and through-thickness cracking are eliminated and replaced by interfacial cracking (see Figure 3.5).

For the sample 4 (the induction heating case - see Figure 3.5), the oxide phases closest to the oxide–air boundary displayed evidence of delamination at all locations (A, B, C, D) and the lowest interfacial strength and cohesion remained adhered to the steel, suggesting high metal–oxide interfacial strength and adhesion. Sample 4B highlights how the higher porosity, thicker, outer oxide layers delaminate along an oxide phase boundary, indicating lower interfacial strength and cohesion, whilst the most compact, thinner, innermost layers remain adhered to the steel, suggesting high metal–oxide interfacial strength and adhesion. Also, samples 4A and 4B exhibit higher levels of interfacial roughness for the two outermost oxides, which are ultimately spalled. This has also been shown to negatively affect both kinetic and adhesion behaviour with thicker, defect-containing oxides showing greater evidence of interfacial separation [78], [79], [91], [128]. Furthermore, roughness amplitude and period were core parameters when calculating critical spallation strain (see Equation 2.2) therefore reinforcing the importance of accurate roughness assessments. It has already been reported that varying surface condition is associated with inconsistent oxide spalling, arising from the oversimplification of the scale to a single body that can also be mechanically removed as a single body. In reality, the multi-phase nature of the scale is more accurately represented as multiple bodies whose adhesive and cohesive properties vary in the same way as their intrinsic mechanical properties [128]. Several authors have alluded to the importance of the interaction of phase transformations and descaling processes that were limited to planar samples, with the exception of Jiang et al. [75], and focused on other aspects of oxidation such as mechanical response [74], heat transfer behaviour [10], [75], and microstructural characterisation [129]. However, since Kendall et al's model is limited to a single moving phase, and the biggest challenge arguably arises from the adhered inner layer that is evidently resistant to hydraulic descaling, further uses of the model with respect to stress analysis should be limited to a compact layer of homogeneous oxide. It is still valid to assume that this homogeneous phase will be an oxide as it is typically found closest to the metal–oxide reaction interface as it has the lowest oxygen content of the three phases typically detected in an oxide formed on low-carbon steel [130]. The oxide is therefore assumed to have already been exposed to descaling-related stresses, as described by Basabe and Szpunar [40], during stress analysis, rather than adding further complexification. However, this highlights a key application of the curved surface AOSFD to improve understanding of hydraulic descaling efficiency changes during technological changes e.g. both heating technology cases (gas-barrel vs. induction) there will be a retained layer of well-adhered oxide after descaling but, should this layer be successfully descaled with technological advances in hydraulic descaling, oxide descaled after induction-based normalisation will be easier to process due to the spalling of larger, delaminated layers (compared to disparate powder-like oxide from gas-barrel-based heating).

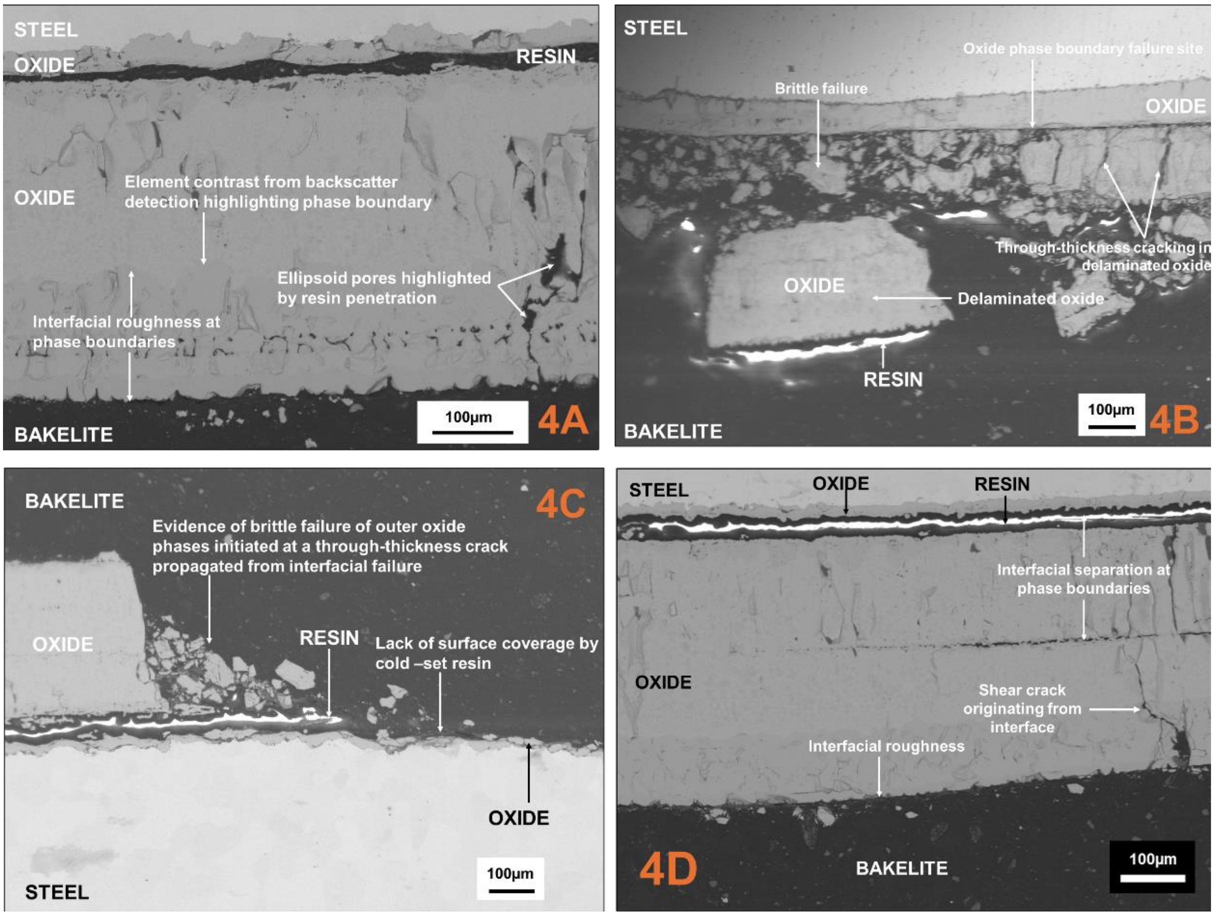

Figure 3.5: Annotated field emission gun scanning electron micrographs for a 15 nominal bore (**n.b.**) conveyance tube after a normalisation replication cycle in an ambient thermogravimetric tube furnace and subsequent metallographic preparation. Oxide images were taken at four approximately equidistant locations around each tube circumference (A-D).

This highlights one of the main secondary challenges of oxide failure as to whether the ideal scale should be perfectly adhered (to act as passive corrosion prevention [131]) or highly descalable (to optimise surface finish), to only the outer tube surface. However, it should be noted that proposals for a thick (several millimetres [130]) but highly descalable oxide are undesirable during tube manufacture, not least due to the associated material yield loss, but also due to the poorer surface quality, increased asset contamination, and slower line speed resulting from increased descaled volume. Therefore, optimal scale behaviour during tube manufacture would be perfect adherence or interfacial failure as large sheets, as in the manner referred to in 1.1.2.1, to minimise its damaging dispersal into the environment. Therefore, both the **AOSFD** computationally driven and experimental validation results demonstrate how the electromagnetic control associated with induction heating result in a reduction in thermal stress which promotes tensile failure modes, especially interfacial failure and through-thickness cracking, which achieve a more process-friendly oxide failure. However, this phenomenon is limited to the outer phases of oxide, with existing hydraulic descaling technology, both gas-barrel and induction normalised samples exhibit a retained layer which could still be rolled-in due to the high-temperature plasticity of wüstite. Abuluwefa et al. [38] remarked that spalling can also be accelerated by geometry, dimensions, and service environments which intensify stress fields, e.g. corners, mechanical vibrations, thermal stress, and surface defects. This is particularly important for the tube geometry considered in this project where forming procedures inherently introduce internal and external stresses. Hence, understanding of the scale morphology and kinetics, how it is adhered, and its likelihood of spalling both prior to and during descaling can help inform models of scale formation and descaling as well as optimise processes such as tube production.

The challenge of porosity has already been discussed by other authors [132]-[134], and was addressed by Kendall et al. [80], in particular how pores become larger and non-uniformly distributed as the oxide grows on a curved geometry and the outermost oxide moves further from the metal–oxide reaction interface, thus making the model less accurate [133]. Samples 4A and 4D (induction heated) in particular show evidence of large, randomly distributed pores, highlighted by infiltration with the cold-set mounting resin. This observation agrees with the trend proposed by Entchev et al. that thicker scales exhibit higher levels of large, non-uniformly distributed pores [133]. Entchev et al. [133] highlighted how porosity becomes less uniform and pores become larger as the oxide thickens and preceding oxide layers expand. Pores can act as points of stress concentration and therefore promote the growth of the cracks (shear and through-thickness) observed at all locations of sample 4 (A, B, C, D) [135]. The mechanical issues associated with porosity are also compounded by the defect-sensitive nature of non-stoichiometric wüstite where pores are liable to develop as a result of vacancy migration and diffusive processes [30], [92].

Much of the microstructural and microtextural properties of the induction samples, e.g., ridges, roughness, through-thickness cracking, interfacial cracking, and severe spalling, are typical of oxide formed in air, i.e., heating atmosphere has been shown to be important [74], [136], [137]. Wang et al. highlighted that electrochemically grown oxides, i.e., oxides with limited exposure to air, are far more likely to be compact, homogeneous, uniform, and intact [132]. Hence, the oxide of the same description found in industrial samples (1, 2, 3) can only have grown with limited access to air caused by the existing layers of oxide above its outer surface. Furthermore, plastic deformation during the conveyance tube manufacturing process can contribute to pore elimination. This further supports the idea that descaling causes delamination as opposed to any spalling during the oxidation reaction itself, since then the lost outer layers of oxide on the industrial sample would begin to show characteristics of air-based oxidation. Previous work has highlighted that poor scale adhesion is ultimately a combination of kinetic and mechanical phenomena [138], and the kinetic phenomena that propagate circular pore formation are deformed to ellipsoids (observed in Figure 9) under compressive thermal and growth stresses [77], [132].

Although, changes to oxide failure mode can be correctly attributed to temperature, as was seen in the work of Krzyzanowski and Beynon [50], the use of the **AOSFD** in this way highlights the importance of considering the effect of mechanical phenomena. As previously discussed in 1.1, the conveyance tube manufacturing process is short and fast with a high feed rate. Hence, high levels of thermomechanical stress are expected and should be considered in parallel when attempting to proactively control scale. The **AOSFD** offers additional mechanical insight based on the kinetic data and allows for a degree of this parallel consideration.

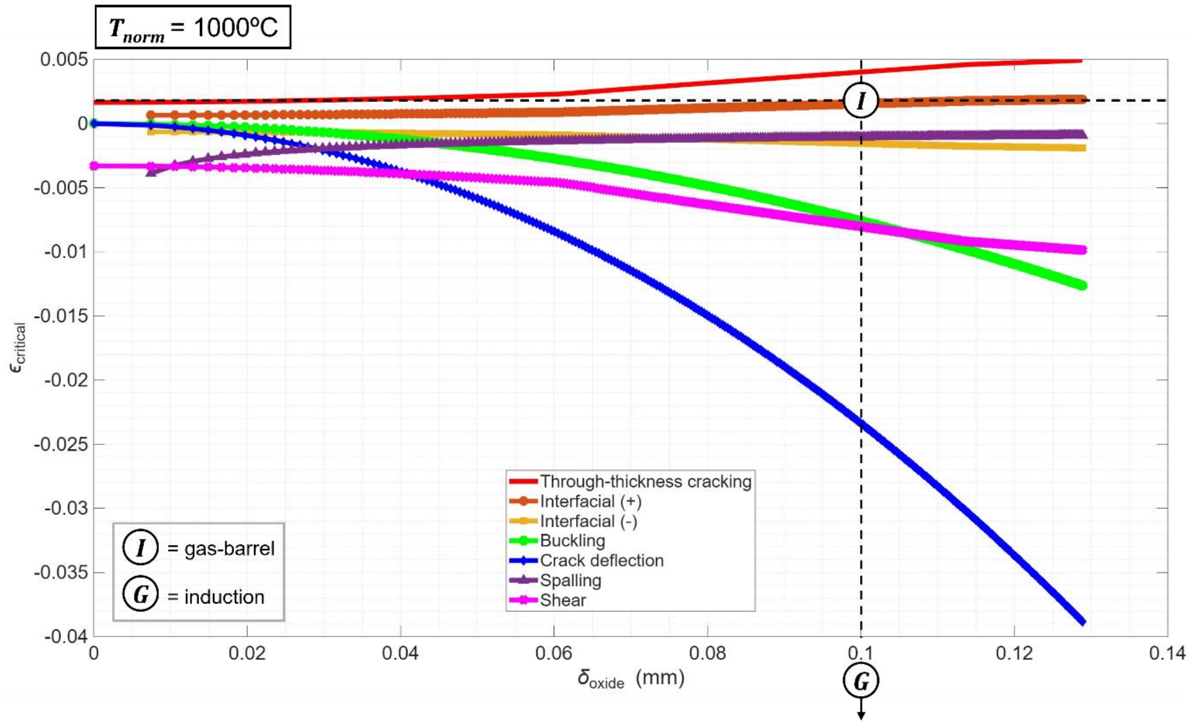

Figure 3.6: Advanced Oxide Scale Failure Diagram (Plot of critical failure strain, $\boldsymbol{\varepsilon_{critical}}$, against oxide thickness, $\boldsymbol{\delta_{ox}}$,) for a 15 nominal bore (**n.b.**) conveyance tube normalised at 1000°C ($\boldsymbol{T_{norm}}$) for 3 mins, forming 99.7μm of oxide. For identical thermal conditions, 'A' represents the resultant strain for 99.7μm of gas-barrel furnace-grown oxide, while 'B' represents the resultant strain for 99.7μm of induction-grown oxide. For accessibility, each failure mode boundary is denoted by both colour and symbols indicating their start and end datapoint.

As previously demonstrated, the implementation of fully induction-based heating technology offers greater manufacturing control and the opportunity to proactively manage scale kinetics and adhesion via increased heating speed and electromagnetic operation parameter adjustment respectively. Consequently, the success of induction heating as a technique depends on strategic selection of the combination of coil structure, current levels, and heating times, especially in the case of curved geometries where these parameters will be dependent on cross-sectional profile consistency and curvature radius [46]. Good heating efficiency is essential to maximise heat dispersion and prevent overheating in certain regions of the tube [45]. In the initial stages of implementation of induction technology, temperature control must be investigated to mitigate against the risk of workpiece overheating. The low carbon region (≤0.2wt%) [139] of the Fe-C phase diagram [140], derived using Thermo-Calc©, can be used to identify the melting point of the steel at 1475°C for the upper wt% C limit defined by BS EN 10217-2 [141]. This temperature is still within the upper temperature limits of the data used to develop the thermodynamic and kinetic databases described by Kendall et al [7]. The austenitic region encompasses the entire temperature range investigated, and the validity of the austenite-based thermochemical model used to generate oxide thickness data [7] is not undermined. The model was therefore employed for a normalisation temperature, $\boldsymbol{T_{norm}}$, range of 1000-1400°C, in 100°C intervals, to evaluate the potential effect of normalisation temperature instability by induction heating on oxide kinetics and adhesion. However, the increased rate of oxidation associated with higher temperatures [130] is a significant enough change, combined with a comparatively low wall thickness of 3mm, that the total normalisation temperature soak time was decreased to ensure the substrate material was not used up before the end of the soak period leading to simulation failure. However, in all cases the simulation could still be run for long enough to obtain sufficient data points to accurately assess parabolic rate coefficient, $\boldsymbol{k_p}$, based on the rate of in-situ oxide thickness gain, and maintain a constant time increment. Table 3.2 shows the maximum soak time, $\boldsymbol{t_{norm,max}}$, possible for at each temperature (1000-1400°C), $\boldsymbol{T_{norm}}$, and the associated number of datapoints, $\boldsymbol{N}$, before the steel substrate was completely consumed at $\boldsymbol{t_{fail}}$ (where 'fail' refers to numerical failure of the

Thermo-Calc© model due to diffusion-driven elimination of the steel domain, rather than physical oxide failure).

Table 3.2: Time, t_{fail}, and number of datapoints, N, at which the Thermo-Calc© oxide kinetic model failed for each temperature, T_{norm}, due to complete consumption of the steel substrate. The maximum soak time for each temperature before complete consumption of the substrate, $t_{soak,max}$, is also shown.

T_{norm} (°C)	t_{fail} (hrs)	N (-)	$t_{soak,max}$ (hrs)
1000	-	121	24
1100	-	121	24
1200	15.1	88	15
1300	8.5	63	8
1400	5.2	52	5

The data for a typical three minute normalisation soak time, $t_{norm,min}$, were used for all analyses below. Figure 3.7 shows that, for a constant tube geometry, an increase in normalisation temperature, T_{norm}, will cause a linear increase in oxide thickness. The same is true for the mass-, $k_{p,mass}$, and thickness-, $k_{p,thickness}$, based parabolic rate coefficients, which follow an Arrhenius-type exponential increase [11] (see Figure 3.8 and Figure 3.9). This supports the physical validity of Kendall et al's Thermo-Calc© model [7], as it is originally numerically derived from a diffusion-based partial differential equation (**PDE**) [142], [143] but still agrees with typical analytical temperature trends for oxide kinetics [8], [14], [37].

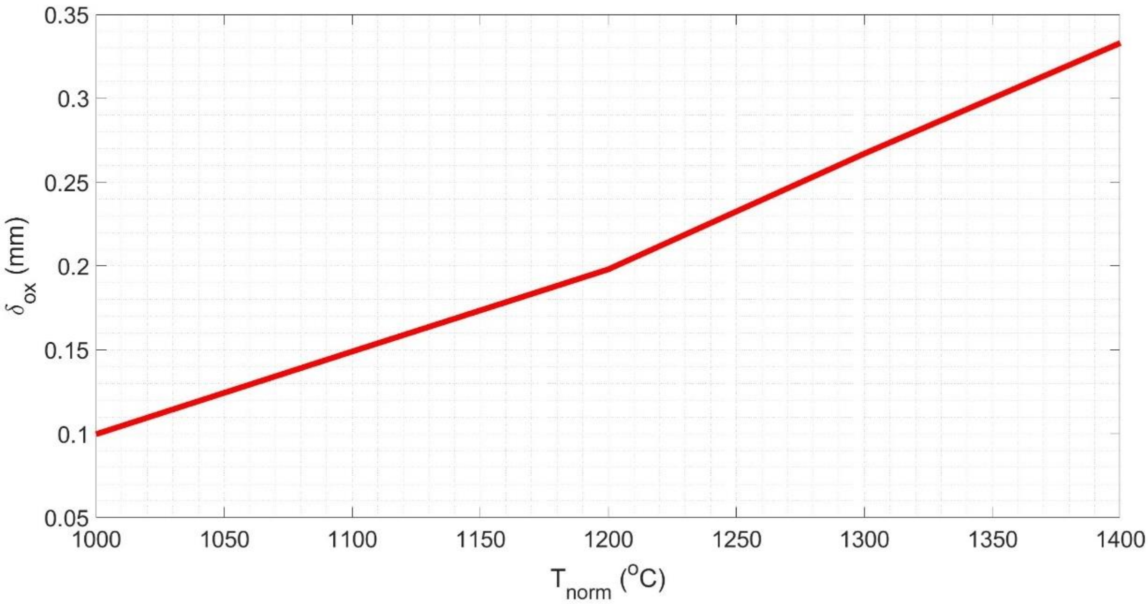

Figure 3.7: Plot of oxide thickness, δ_{ox}, against normalisation temperature, T_{norm}, for a 15 nominal bore (**n.b.**) conveyance tube normalised at 1000°C for 3 mins. The temperature range used is 1000-1400°C with 100°C increments in datapoints.

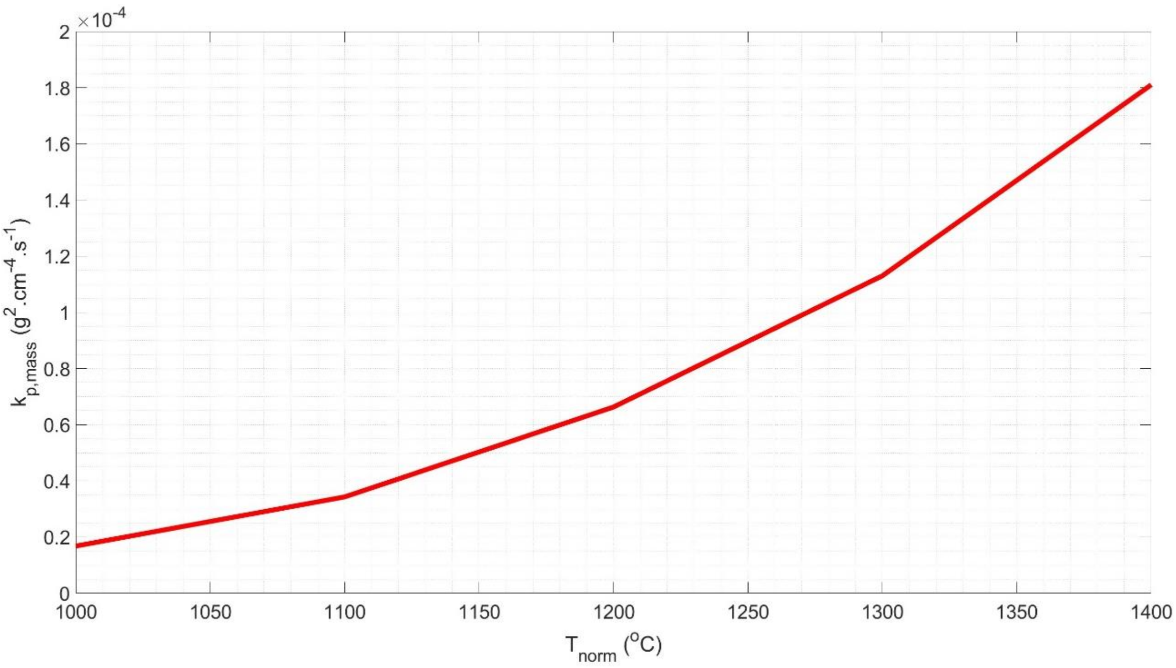

Figure 3.8: Plot of mass-based parabolic rate coefficient, $\boldsymbol{k_{p,mass}}$, against normalisation temperature, $\boldsymbol{T_{norm}}$, for a 15 nominal bore (**n.b.**) conveyance tube normalised at 1000°C for 3 mins. The temperature range used is 1000-1400°C with 100°C increments in datapoints.

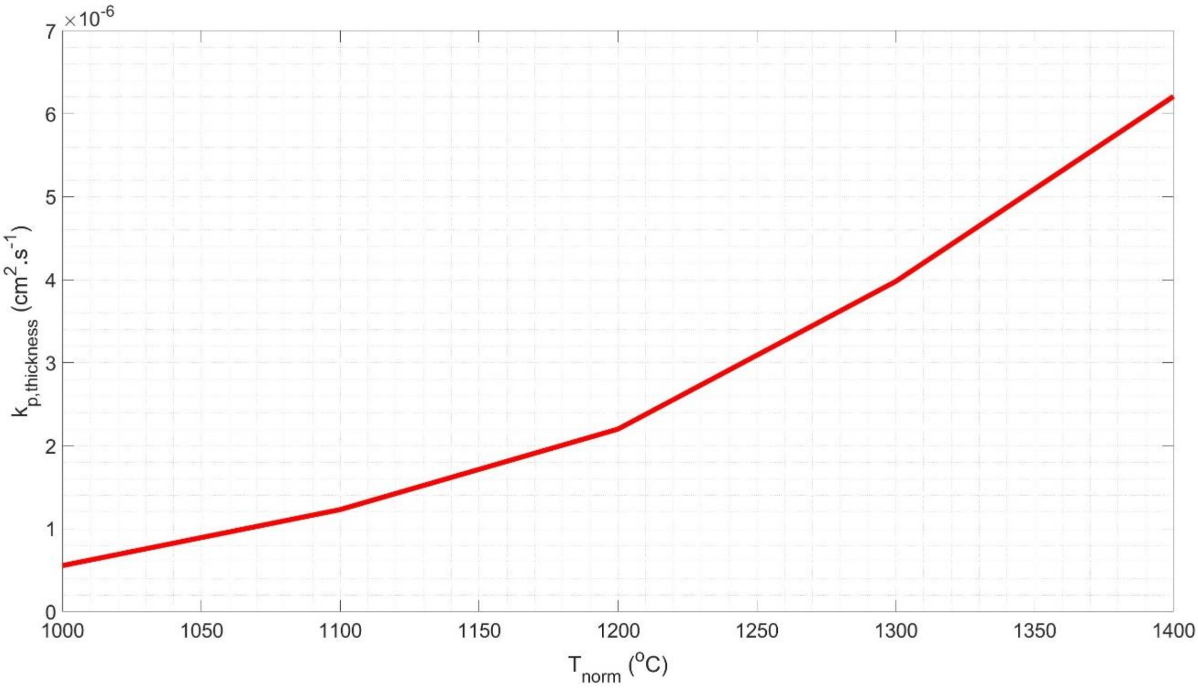

Figure 3.9: Plot of thickness-based parabolic rate coefficient, $\boldsymbol{k_{p,thickness}}$, against normalisation temperature, $\boldsymbol{T_{norm}}$, for a 15 nominal bore (**n.b.**) conveyance tube normalised at 1000°C for 3 mins.

In the case of gas-barrel heating, there is an overall linear decrease in compressive thermal strain magnitude associated with an increase in temperature (and therefore oxide thickness) (see Figure 3.10). At 1400°C, there is an exception to this trend as strain increases. This temperature lies on the upper bound of validity of expressions for expressions of elastic modulus [111] and linear coefficient of thermal expansion [144]. Anderson concluded that Wachtman's equation [145] for the temperature dependence of elastic modulus is only valid when the variation of Poisson ratio with temperature is negligible [146]. Vigilante et al measured the variation in Poisson ratio of steel over a temperature range of 25-400°C and observed a less than 0.1 change in Poisson ratio [147]. However, extrapolation of the linear trend observed would lead to a physically invalid value of Poisson ratio at temperatures >1000°C and indicates that there is a different relationship for temperature and Poisson ratio in this temperature range. However, assuming a general decrease with increasing temperature, based on Vigilante et al's work [147], a decrease in Poisson ratio would cause an overall decrease in lateral strain magnitude [119]. Furthermore, a decrease in Poisson ratio would have the inverse effect on thermal stress and increase its magnitude (see Equation 7.1). Additionally, the rate of increase in the linear coefficient of thermal expansion shows an anomalous acceleration at temperatures close to its melting point. Drebushchak attributed this to the increase in mean interatomic distance at higher temperatures, compared to changes at lower temperatures even with same energy change [148]. Hence, the difference between the linear coefficient of thermal expansion between the metal and oxide is expected to increase and overall increase the magnitude of stress in the oxide due to thermal expansion mismatching. Finally, at a temperature between 1300ºC and 1400ºC, depending on its stoichiometry, wüstite will undergo a phase change at the onset of melting [149]. This phase change will be preceded by a period of softening characterised by substantial weakening of the crystalline structure and grain reorganisation. As a non-stoichiometric compound [103], wüstite will also exhibit atomic diffusion and defect clustering [150]. Due to these effects, there is a significant increase in compressive thermal strain i.e. shrinkage.

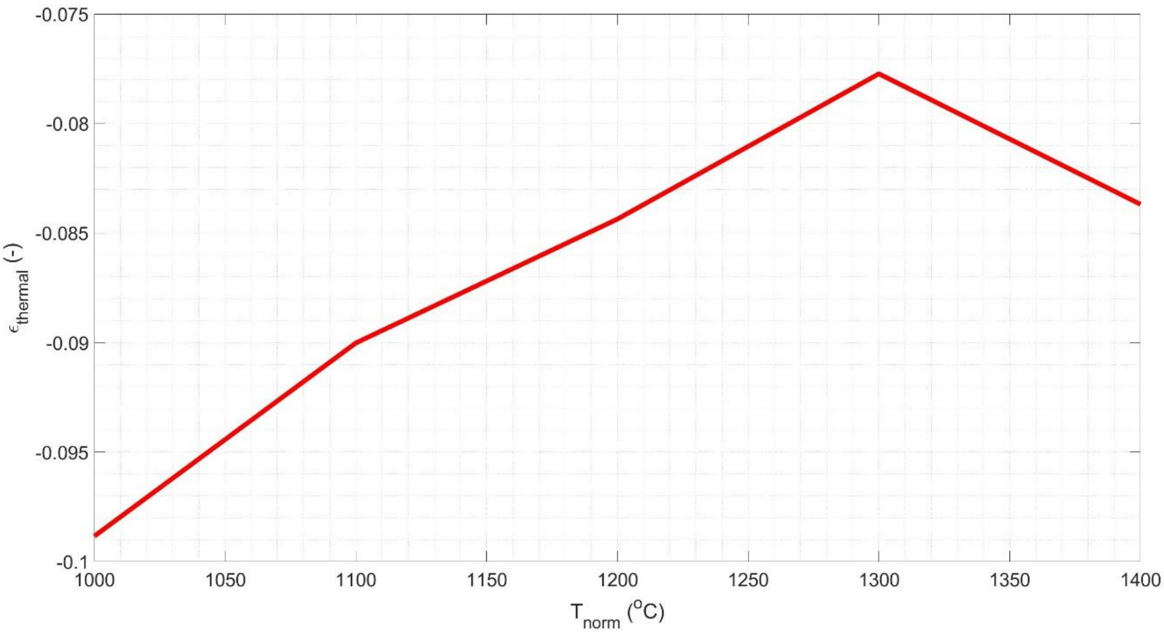

Figure 3.10: Plot of thermal strain, $\boldsymbol{\varepsilon_{thermal}}$, against normalisation temperature, $\boldsymbol{T_{norm}}$, for a 15 nominal bore (**n.b.**) conveyance tube normalised at 1000°C for 3 mins.

Similarly, growth strain increases linearly with temperature and oxide thickness but does not display an anomaly at 1400°C (see Figure 3.11). Growth stress is calculated based on ambient temperature values of elastic modulus and does not depend on Poisson ratio or the linear coefficient of thermal expansion. Therefore, the observation in Figure 3.11 supports the hypothesis that the anomalous increase in thermal stress at high temperatures is due to the temperature-dependent nature of thermal expansion and crystallinity changes close to a phase change i.e. melting. Interestingly, a three times thicker scale by increasing normalisation temperature by 400°C, leads to a two-fold increase in growth strain. This is greater than the change elicited in thermal strain by the same temperature and oxide thickness increase, at a factor of only 1.2.

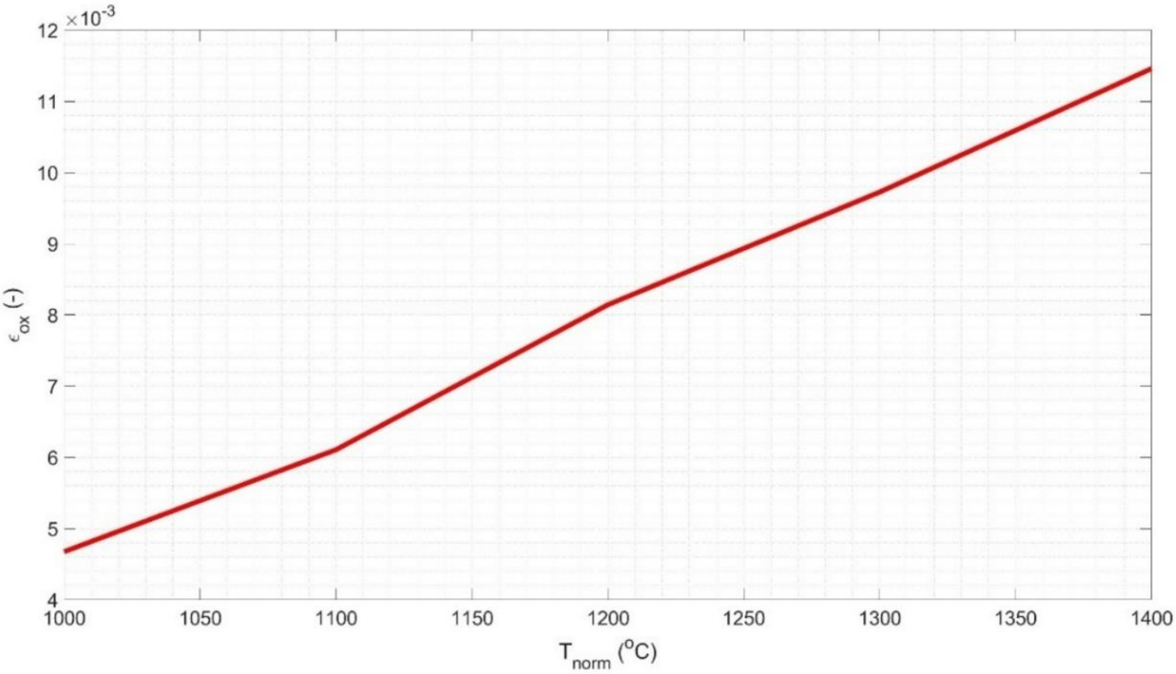

Figure 3.11: Plot of growth strain, ε_{ox}, against normalisation temperature, T_{norm}, for a 15 nominal bore (**n.b.**) conveyance tube normalised at 1000°C for 3 mins.

Figure 3.14 highlights how an increase in normalisation temperature leads to an increase in the contribution of tensile strain to the overall state of the oxide, regardless of whether it was formed under gas-barrel or induction heating technology. However, the thermal stress can be maintained at a constant value by appropriate current frequency control [49], thus reducing its compressive contribution and making the overall stress state tensile. Where the gas-barrel formed oxide is in an overall compressive state, the effect of the increase in temperature within the two heating techniques has opposing effects. The introduction of additional tensile growth stress, and oxide thickness which increases the critical failure strain for each mode, serves to decrease the strain magnitude in the gas-barrel grown oxide, to the extent that the **AOSFD** shows that beyond 1300°C the strain is low enough to eliminate failure by crack deflection. In contrast, although the absence of any increase in thermal stress, via operational control, limits the overall strain magnitude increase, the introduction of additional tensile growth strain increases the overall strain magnitude and makes the critical failure strain for interfacial cracking much more likely to be exceeded. In light of the inner oxide descaling challenges [36], [73], [128], this phenomenon could be advantageous in ensuring that oxide is more likely to be fully descaled as the stress applied during descaling will be more likely to result in a critical failure strain being exceeded. However, there is still a balance to be struck between effect of temperature increase on oxide behaviour, mechanical properties, component-tooling interaction and component softening [151]. The **AOSFD** developed has the ability to encapsulate all the information in a single graph. The output of each AOSFD for temperatures in the range 1000-1400ºC is summarised in Figure 3.12 and Figure 3.13.

Figure 3.12 shows that as temperature increases, oxide thickness increases (as dictated by kinetics) and this is accompanied by an increase in critical strain magnitude for all failure modes as more material can accommodate more bending and/or buckling stress [119]. Lee et al.'s scale failure map [78] also demonstrated how an increased scale thickness can trigger wedging failure solely due to internal growth and thermal stresses, therefore thicker scales are associated with a weaker interface (due to higher internal stresses) and more pre-bending fracture.

This increase in critical strain associated with higher temperatures is favourable for the gas-barrel heating case, as the increase in resultant strain associated with a thickening oxide does not match the rate of critical strain increase. However, this is not the case for the induction-heating case as the oxide's tensile state increases (due to the increased contribution of growth stress) and critical strains for interfacial failure and through-thickness cracking are exceeded as supported by evidence in Figure 3.5.

Therefore, the control over tensile failure modes achieved by transition to induction heating technology can only be capitalised upon if there is sufficient electromagnetic control to prevent overheating. A key feature of induction heating is that the part becomes its own heating element wherein the highest temperature is generated, controlled, and confined to the region in direct proximity to the coil. Thus, induction heating is a fast and accurate localised heating technique. Current is the most influential variable during induction heating, although heating rate and depth can also be adjusted by changes to the coil turn number and spacing, and part-coil coupling distance [108]. The ability to precisely regulate heating conditions, via control of electrical (e.g. current frequency), thermal (e.g. cooling conditions), and geometric (e.g. coil geometry) input parameters, is a key advantage of induction technology in scale management efforts (provided electrical load capacity demands can be met) [49]. Zhao et al. [46] highlight that the complex interaction of electromagnetic and heat transfer phenomena during induction heating results in a strong influence of the induction coil not only by the current frequency, as investigated in this paper, but also by shape (the oval coil as the best for achieving uniform magnetic flux distribution) air gap (a narrower air gap will promote faster temperature rise), and component feed rate (a faster feed will improve temperature uniformity across the component). They also highlight the challenge of a narrow processing window in controlling temperature distribution, which also applies for the conveyance tube manufacturing process, which totals only ~15 mins. It is possible that the effect of oxide scale could be incorporated into future coil design and electromagnetic parameters, when using induction technology for heat treatment of components such as steel tubes.

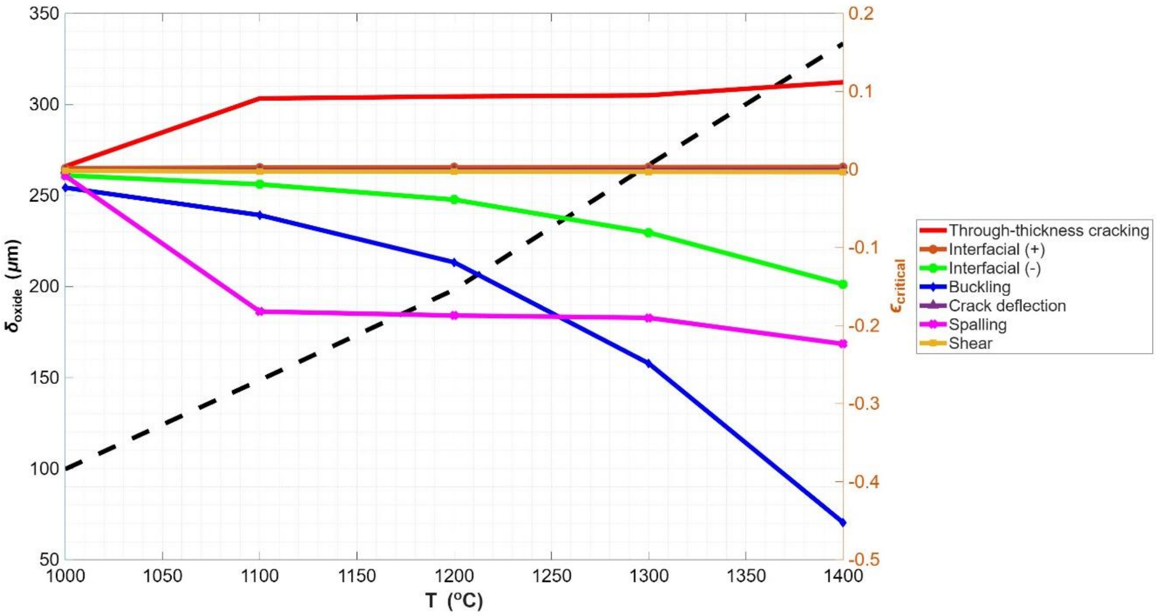

Figure 3.12: Dual plot of critical failure strain, $\varepsilon_{critical}$, and oxide thickness, δ_{ox}, against temperature, T, for a 15 nominal bore (**n.b.**) conveyance tube with critical failure strains for each failure mode calculated using an **AOSFD**.

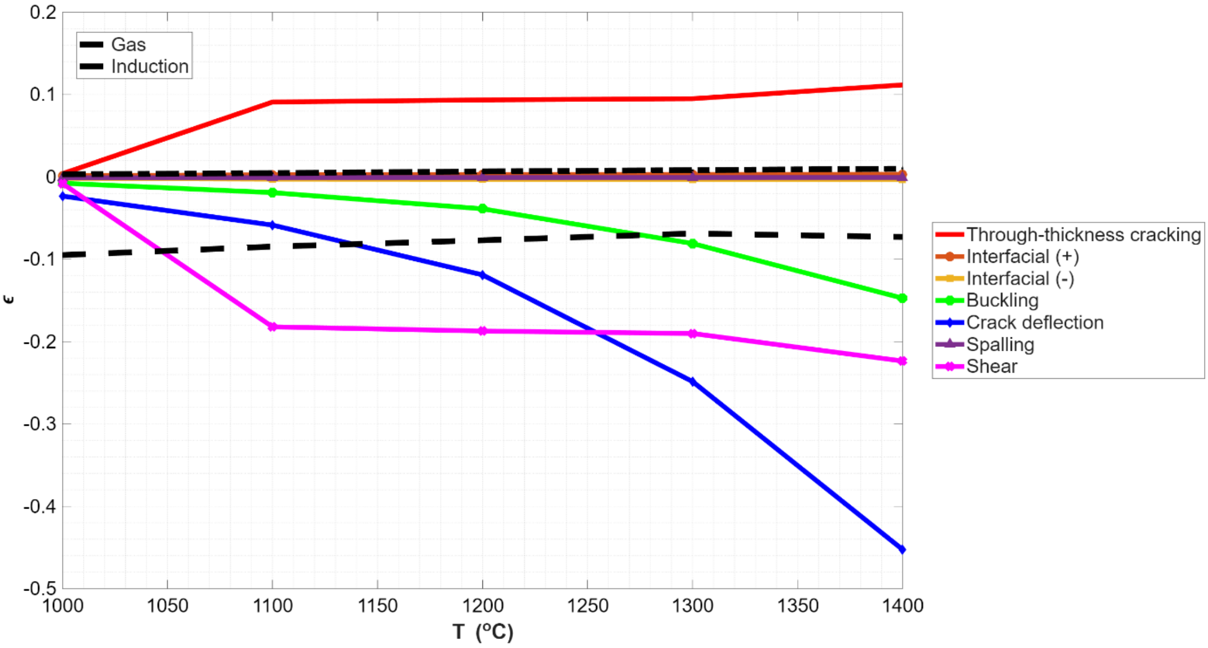

Figure 3.13: Plot of critical failure strain, $\boldsymbol{\varepsilon_{critical}}$, against temperature, $\boldsymbol{T}$, for a 15 nominal bore (**n.b.**) conveyance tube with critical failure strains for each failure mode calculated using an **AOSFD**.

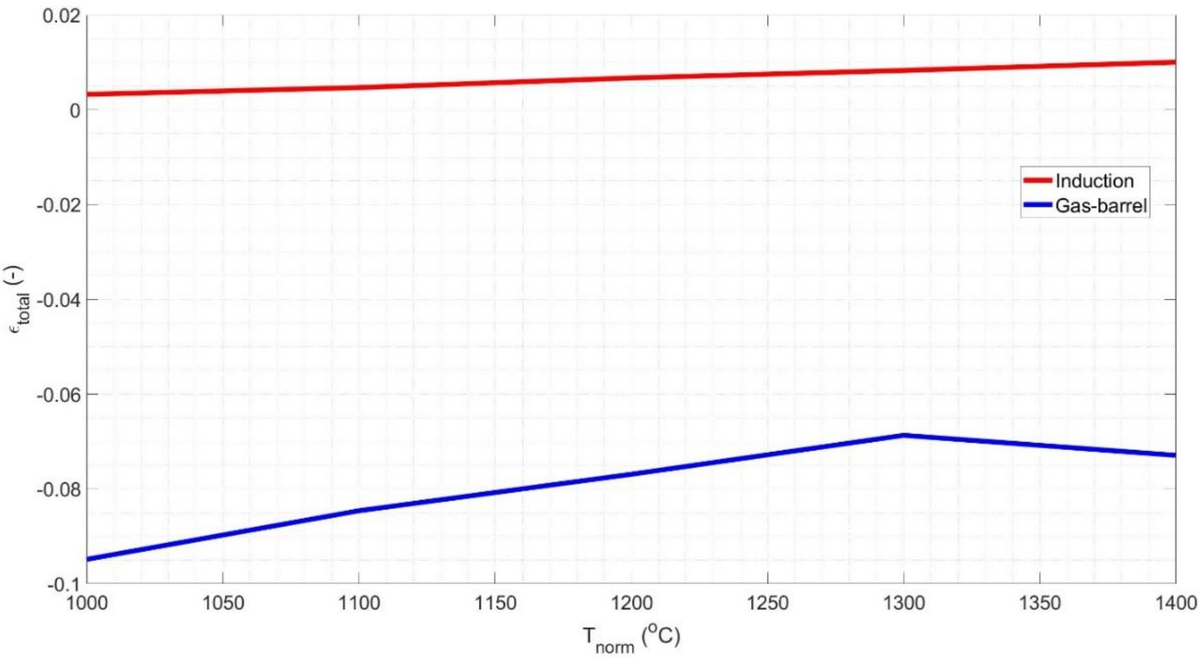

Figure 3.14: Plot of resultant strain, $\boldsymbol{\varepsilon_{total}}$, against normalisation temperature, $\boldsymbol{T_{norm}}$, for a 15 nominal bore (**n.b.**) conveyance tube normalised at 1000°C for 3 mins under induction (*red*) and gas-barrel (*blue*) heating.

Overall, the conclusions of the **AOSFD** agree with Krzyzanowski and Beynon's findings about increased temperature being associated with a higher probability of Mode II failure, i.e. interfacial cracking and raft slip, where it is easier to achieve consistent delamination. However, the **AOSFD** is supported by evidence in addition to experimental observation, and compromises information from manufacturing operation history, physics-based modelling, and analytical fracture mechanics. Crucially, the **AOSFD** expresses the complex technicalities of oxidation on a curved surface in a single diagram which is quick and easy to interpret when applied to industrial scenarios comprising a range of thermomechanical processing conditions. It requires only an estimate of oxide thickness, which can be predicted by computational thermochemistry [7], and its associated resultant strain to predict failure probability and mode. Also, individual operation history parameter inputs, e.g. surface

roughness, radius of decohesion can easily be updated to regenerate a new **AOSFD** as the defining equations are consistent for each failure mode. A contemporary potential application example would be the wider implementation of electric arc furnaces [25] in the steel sector, which introduce different steel compositions [152], [153] and lower tolerance for spalled oxide reprocessing [56]. More detail on how an AOSFD could be applied to the scenarios discussed in 1.1.2.1 is given in Table 3.3.
It should be noted that the effect of gas impurities, such as water and other oxidation-enhancing or -inhibiting species [8], [40], [154], on parabolic rate coefficient cannot be quantified within the model or **AOSFD** at this stage. These gas impurities can also affect mechanical properties [128] and porosity [37]. However, as both heating techniques occur in air, the degree to which these species vary should not be as significant as in the case of fossil fuel-based heating [37]. This aspect of work is better suited to future experimental work where controlled atmosphere furnaces can be used.

Table 3.3: Examples of manufacturing scenarios where an AOSFD could be applied to aid manufacturing change or improvement.

Scenario	Objective	Rationale	AOSFD Strategies
Electric Arc Furnace (**EAF**) steelmaking	Lower oxide reprocessing and recycling demands	Minimise volume of spalled oxide as not suitable for reprocessing via **EAF** steelmaking and environmental concerns for metal-based waste disposal	• Use induction heating to obtain a tensile state oxide which is more likely to undergo interfacial failure as larger pieces which are easier to process. • Change manufacturing parameters, e.g. component dimensions, component surface finish, temperature, to reduce resultant strain in component to value below critical failure strain for all failure modes (indicated by AOSFD)
Manufacturing tool wear	Extend tool life	Enable oxide failure in large, compact sheets which can be removed from the manufacturing line quickly and easily to prevent particle entrainment	• Use induction heating to obtain a tensile state oxide which is more likely to undergo interfacial failure as larger pieces. • Redesign induction coil with suitable geometry and air gap to optimise electromagnetic (and subsequently) temperature control
Hydrogen conveyance for energy applications	Protection against hydrogen permeation and embrittlement	Maximise thickness and integrity of adhered oxide along tube inner surface length as hydrogen	• Change manufacturing parameters, e.g. component dimensions, component surface finish, temperature, to

		diffusion slower in oxide than steel	reduce resultant strain in component to value below critical failure strain for all failure modes (indicated by AOSFD) • Redesign induction coil with suitable geometry and air gap to optimise electromagnetic control (and subsequently) and temperature distribution across component wall thickness and/or length. • Use AOSFD to assess sensitivity of failure mode and effect to temperature changes to establish level of electromagnetic control needed.

4 Conclusions

Analysis of the stress state of the oxide following the tube manufacturing process and computationally derived predictions of oxide thickness allowed the development of an Advanced Oxide Scale Failure Diagram (**AOSFD**) specifically for oxide growing on a curved surface. In particular, this work demonstrates the development of a higher level ($\boldsymbol{n} > 3$) AOSFD than those presented in existing literature. This is deemed a necessary development due to the effect of non-planar geometry on oxide microstructure, kinetics, and integrity, and the complexities of the use of computational thermochemistry to derive dynamic oxide thickness data. To demonstrate the translatable application of the **AOSFD**, a comparison was drawn between the oxide state after induction vs. gas-barrel heating. High temperature steel processing is increasingly dependent on induction-based heating technologies due to global decarbonisation efforts. Current frequency control during induction heating can elicit a 30-fold decrease in strain magnitude, by minimising thermal residual stress to 100MPa, and lead to a tensile resultant strain which eliminates compressive failure modes, e.g. shearing, buckling, observed during gas-barrel heating. Tensile failure modes, namely through-thickness cracking and interfacial failure, are more probable during induction heating. The outcomes predicted by the AOSFD were supported by post-normalisation microscopy of small conveyance tubes normalised in gas-barrel vs. induction furnaces. It was also demonstrated that higher than expected temperatures (1100-1400°C), associated with the steep thermal gradients evolved by induction heating technology, eliminated compressive failure modes such as buckling but increased the likelihood of interfacial failure. This is reflective of the three-fold increase in oxide thickness and associated increase in strain magnitude by a factor of 2.33 when temperature is increased from 1000°C to 1400°C. The developed **AOSFD** highlights the shift from compressive to tensile failure modes when transitioning from gas-barrel to induction-based heating technology. However, the advantages of induction heating, with respect to oxide failure mode and effects, can only be retained if there is sufficient electromagnetic control to prevent ultra-high temperatures beyond the level required for the manufacturing process. Achieving electromagnetic control not only depends on electrical control, but also coil geometry, air gap width, and component feed rate which can be incorporated into future conveyance tube manufacturing system designs. The investigations in this work agree with purely temperature-based studies of oxide failure mode, but also account for mechanical response of the oxide, derived from conveyance tube manufacturing, in parallel with kinetic phenomena by combining diffusion- and fracture-mechanics based analyses into a single diagram which can be applied to industrial contexts quickly and flexibly to inform manufacturing decisions. This is important for existing technological challenges, such as oxide descaling efficiency and oxide-induced tool wear, but also future steel-based technologies where oxide control will affect performance, e.g. **EAF** steelmaking, hydrogen conveyance for energy.

5 Abbreviations

The following abbreviations are used in this manuscript:

Abbreviation	Meaning
AOSFD	Advanced Oxide Scale Failure Diagram
EAF	Electric Arc Furnace
FEA	Finite Element Analysis
FEGSEM	Field Emission Gun Scanning Electron Microscopy
HVAC	Heating Ventilation and Air Conditioning
n.b.	Nominal Bore
OAF	Oxygen-enriched Air-Fuel
OC	Oxy-fuel Combustion
PDE	Partial Differential Equation
RGB	Red-Green-Blue
SCI	Scale-Coating Interface
SGI	Scale-Gas Interface
SSI	Steel-Scale Interface
STI	Scale-Tool Interface
TGA	Thermogravimetric Analysis
XRD	X-ray Diffraction

6 References

[1] C. H. Simmons, N. Phelps and D. E. Maguire, "CAD organization and applications," in *Manual of Engineering Drawing: Technical Product Specification and Documentation to British and International Standards,* 4th ed.Anonymous 2012, Available: https://ifind.swansea.ac.uk/permalink/44WHELF_SWA/1jlslid/alma998192368202417.

[2] M. Hosseinzadeh, N. Kasiri and M. Rezaei, "A comprehensive multiscale review of shaft furnace and reformer in direct reduction of iron oxide," *Minerals Eng,* vol. 222, 2025. Available: https://internal-pdf://3476537216/310] 1-s2.0-S0892687524005521-main.pdf https://doi.org/10.1016/j.mineng.2024.109123.

[3] G. G. Goviazin, D. Rittel and A. Shirizly, "Achieving high strength with low residual stress in WAAM SS316L using flow-forming and heat treatment," *Materials Science and Engineering: A,* vol. 873, 2023. Available: https://internal-pdf://0354176833/267] 1-s2.0-S0921509323004677-main.pdf https://doi.org/10.1016/j.msea.2023.145043.

[4] M. SchÃ¼tze, "The Role of Stresses in High-Temperature Corrosion: The Potential of Quantitative Approaches," *High Temperature Corrosion of Materials,* vol. 100, pp. 365–397, 2023. Available: https://internal-pdf://1348827531/209] s11085-023-10191-1.pdf https://doi.org/10.1007/s11085-023-10191-1.

[5] N. Shajan *et al*, "Role of residual stress in the failure of HF-ERW welded tubes," *Eng. Failure Anal.,* vol. 161, 2024. Available: https://internal-pdf://3384123654/264] 1-s2.0-S1350630724003881-main.pdf https://doi.org/10.1016/j.engfailanal.2024.108342.

[6] A. Wassilkowska and D. Wojciech, "Silicon as a component of ferric oxide scale covering ductile iron pipes after annealing," *Eng. Failure Anal.,* vol. 125, 2021. Available: https://internal-pdf://2134297349/202] 1-s2.0-S1350630721002417-main.pdf https://doi.org/10.1016/j.engfailanal.2021.105381.

[7] M. Kendall *et al*, "Computational Thermochemistry for Modelling Oxidation During the Conveyance Tube Manufacturing Process," *Metals,* vol. 14, *(12),* 2024. Available: https://doi.org/10.3390/met14121402.

[8] W. Sun *et al*, "Oxide scales growth of low-carbon steel at high temperatures," *J. Mater. Process. Technol.,* vol. 156, pp. 1300–1306, 2004. Available: https://internal-pdf://0759781654/22] 1-s2.0-S0924013604005497-main.pdf. DOI: 10.1016/j.jmatprotec.2004.04.172.

[9] D. P. Burke and R. L. Higginson, "Characterisation of multicomponent scales by electron back scattered diffraction (EBSD)," *Scr. Mater.,* vol. 42, *(3),* pp. 277–281, 2000. Available: https://internal-pdf://3357916349/23] 1-s2.0-S1359646299003413-main.pdf https://doi.org/10.1016/S1359-6462(99)00341-3.

[10] M. Torres and R. Colas, "A model for heat conduction through the oxide layer of steel during hot rolling," *J. Mater. Process. Technol.,* vol. 105, *(3),* pp. 258–263, 2000. Available: https://internal-pdf://3413146395/21] 1-s2.0-S0924013600005690-main.pdf. DOI: 10.1016/S0924-0136(00)00569-0.

[11] N. Birks and G. H. Meier, "Mechanisms of oxidation," in *Introduction to High Temperature Oxidation of Metals*Anonymous 1983, .

[12] M. Krzyzanowski, J. H. Beynon and D. C. J. Farrugia, "Scale growth and formation of subsurface layers," in *Oxide Scale Behaviour in High Temperature Metal Processing*Anonymous 2010, Available: https://in HT behaviour processing.pdf metal internal-pdf://3019694615/Scale. DOI: 10.1002/9783527630318.

[13] M. Trull and J. H. Beynon, "High temperature tension tests and oxide scale failure," *Materials Science & Technology,* vol. 19, *(6),* pp. 749–755, 2003. Available: https://failure Tension Trull.pdf https://doi.org/10.1179/026708303225003072 internal-pdf://0202103074/24].

[14] I. Iordanova *et al*, "High-temperature surface oxidation oflow-carbon rimming steel," *Surf. Interface Anal.,* vol. 30, pp. 158–160, 2000. Available: https://internal-pdf://1704818585/7] 1096-9918(200008)30_1_158__AID-SIA744_3.0.pdf https://doi.org/10.1002/1096-9918(200008)30:1%3C158::AID-SIA744%3E3.0.CO 2-6.

[15] W. Sun *et al*, "Surface characteristics of oxide scale in hot strip rolling," *J. Mater. Process. Technol.,* vol. 140, *(1-3),* pp. 76–83, 2003. Available: https://doi.org/10.1016/S0924-0136(03)00823-9.

[16] J. H. Jang *et al*, "Investigation of the slab heating characteristics in a reheating furnace with the formation and growth of scale on the slab surface," *Int. J. Heat Mass Transfer,* vol. 53, *(20),* pp. 4326–4332, 2010. Available: https://internal-pdf://3115888112/30] j.ijheatmasstransfer.2010.05.061.pdf http://dx.doi.org/10.1016/j.ijheatmasstransfer.2010.05.061.

[17] J. Grant, "The Development of Novel Coating Solutions for the Improvement of Pre/Post Heat Treatment Performance Properties of Carbon Steel Conveyance Tubes." , Swansea University, Swansea, Wales, UK, 2024.

[18] S. Hallstrom *et al*, "High temperature oxidation of chromium: Kinetic modeling and microstructural investigation," *Solid State Ionics,* vol. 240, pp. 41–50, 2013. Available: https://internal-pdf://3641621279/66] 1-s2.0-S016727381300115X-main.pdf http://dx.doi.org/10.1016/j.ssi.2013.02.017.

[19] H. E. Evans, "Stress effects in high temperature oxidation of metals," *International Materials Reviews,* vol. 40, *(1),* pp. 1–40, 1995. Available: https://in o.pdf effects oxidation https://doi.org/10.1179/imr.1995.40.1.1 temperature internal-pdf://3415911911/Stress high.

[20] M. I. Manning, "Geometrical effects on oxide scale integrity," *Corros. Sci.,* vol. 21, *(4),* pp. 301–316, 1981. Available: https://internal-pdf://3284552196/131] 1837534554000735118375345540007351GEOMET.pdf https://doi.org/10.1016/0010-938X(81)90005-6.

[21] H. Steiner, J. Konys and M. Heck, "Growth Stresses in Oxidized Tubes Under Uni- and Multi-Axial Oxidation Strain," *Oxidation Metals,* vol. 66, pp. 37–67, 2006. Available: https://internal-pdf://1424463921/164] s11085-006-9013-2.pdf https://link.springer.com/article/10.1007/s11085-006-9013-2.

[22] M. M. De Oliveira Junior *et al*, "Effect of iron oxide debris on the reciprocating sliding wear of tool steels," *Wear,* vol. 426-427, pp. 1065–1075, 2019. Available: https://internal-pdf://1597987313/321] 1-s2.0-S004316481831634X-main.pdf https://doi.org/10.1016/j.wear.2018.12.047.

[23] C. Vergne *et al*, "Influence of oxides on friction in hot rolling: Experimental investigations and tribological modelling," *Wear,* vol. 260, *(9-10),* pp. 957–975, 2005. Available: https://internal-pdf://2739499821/322] 1-s2.0-S0043164805003923-main.pdf https://doi.org/10.1016/j.wear.2005.06.005.

[24] P. Lepesant *et al*, "A phenomenological model of the third body particles circulation in a high temperature contact," *Wear,* vol. 298-299, pp. 66–79, 2013. Available: https://internal-pdf://0444636793/323] 1-s2.0-S0043164812002979-main.pdf https://doi.org/10.1016/j.wear.2012.08.019.

[25] T. Skoczkowskia *et al*, "Technology innovation system analysis of decarbonisation options in the EU steel industry," *Energy,* vol. 212, 2020. Available: https://internal-pdf://2953089721/61] 1-s2.0-S0360544220317965-main.pdf https://doi.org/10.1016/j.energy.2020.118688.

[26] M. Auinger *et al*, "Hydrogen accumulation and diffusion in cylindrical-shaped pipeline steels with coating defects," *Int J Hydrogen Energy,* vol. 48, *(88),* pp. 34454–34462, 2023. Available: https://internal-pdf://0205791500/175] 1-s2.0-S0360319923024990-main.pdf https://doi.org/10.1016/j.ijhydene.2023.05.181.

[27] N. Di Luozzo, M. Fontana and B. Arcondo, "Modelling of induction heating of carbon steel tubes: Mathematical analysis, numerical simulation and validation," *J. Alloys Compounds,* vol. 536, *(1),* pp. 564–568, 2012. Available: https://internal-pdf://2331886396/283] 1-s2.0-S0925838811023681-main.pdf https://doi.org/10.1016/j.jallcom.2011.12.084.

[28] X. Z. Zhang *et al*, "Comparative experimental study of hot-formed, hot-finished and cold-formed rectangular hollow sections," *Case Studies in Structural Engineering,* vol. 6, pp. 115–129, 2016. Available: https://internal-pdf://2506234960/98] 1-s2.0-S2214399816300200-main.pdf https://doi.org/10.1016/j.csse.2016.09.001.

[29] D. Stroud *et al*, "Industry 4.0 and the Road to Sustainable Steelmaking in Europe: Recasting the Future," 2024. Available: https://internal-pdf://3905417467/324] 978-3-031-35479-3.pdf https://link.springer.com/book/10.1007/978-3-031-35479-3.

[30] Q. Wu *et al*, "Defect Engineering in Wüstite: Unlocking Control Over Iron Morphologies in Gas-Solid Reduction," *Advanced Science,* vol. 12, *(22),* pp. e2416713–n/a, 2025. Available: https://onlinelibrary.wiley.com/doi/abs/10.1002%2Fadvs.202416713. DOI: 10.1002/advs.202416713.

[31] P. Mullinger and B. Jenkins, "The combustion process," in *Industrial and Process Furnaces : Principles, Design and Operation.*Anonymous 2014, Available: https://ifind.swansea.ac.uk/permalink/44WHELF_SWA/1jlslid/alma998192414202417.

[32] H. T. Abuluwefa, "Scale Formation in a Walking-Beam Steel Reheat Furnace." , McGill University, Montreal, Quebec, Canada, 1992.

[33] M. Auinger *et al*, "A novel laboratory set-up for investigating surface and interface reactions during short term annealing cycles at high temperatures," *Rev. Sci. Instrum.,* vol. 84, 2013. Available: https://internal-pdf://4054419055/84] 1.4817310.pdf https://doi.org/10.1063/1.4817310.

[34] R. L. Higginson, B. Roebuck and E. J. Palmiere, "Texture development in oxide scales on steel substrates," *Scr. Mater.,* vol. 47, *(5),* pp. 337–342, 2002. Available: https://internal-pdf://1527277457/47] 1-s2.0-S1359646202001549-main.pdf https://doi.org/10.1016/S1359-6462(02)00154-9.

[35] C. Wang *et al*, "Analysis of the Local Plastic Deformation of the Surface Oxide Layer formed on Low-Alloy High-strength Steel," *Transaction of the Indian Institute of Metals,* 2022. Available: https://internal-pdf://0478134631/48] Wang2022_Article_AnalysisOfTheLocalPlasti.pdf http://dx.doi.org/10.1007/s12666-021-02491-4.

[36] W. Melfo *et al*, "Experimental Study on Primary Scale Formation and Descalability on Steels Containing Ni and Ni+Si," *ISIJ Int,* vol. 53, *(5),* pp. 866–873, 2013. Available: https://internal-pdf://0478898772/199] 53_866.pdf https://www.jstage.jst.go.jp/article/isijinternational/53/5/53_866/_pdf/-char/en.

[37] C. Schluckner *et al*, "CFD-model to predict the local and time-dependent scale formation of steels in air- and oxygen enriched combustion atmospheres," *Appl. Therm. Eng.,* vol. 143, pp. 822–835, 2018. Available: https://internal-pdf://2951149304/27] 1-s2.0-S1359431118323354-main.pdf https://doi.org/10.1016/j.applthermaleng.2018.08.010.

[38] H. T. Abuluwefa, R. I. L. Guthrie and F. Ajersch, "Oxidation of low carbon steel in multicomponent gases: Part I. Reaction mechanisms during isothermal oxidation," *Metallurgical and Materials Transactions A,* vol. 28, pp. 1633â□“ 1641, 1997. Available: https://internal-pdf://3915342210/4]

Abuluwefa1997_Article_OxidationOfLowCarbon.pdf https://link.springer.com/article/10.1007/s11661-997-0255-7.

[39] H. T. Abuluwefa, R. I. L. Guthrie and F. Ajersch, "Oxidation of low carbon steel in multicomponent gases: Part II. Reaction mechanisms during reheating," *Metallurgical and Materials Transactions A,* vol. 28, pp. 1643â“ 1651, 1997. Available: https://internal-pdf://0347955338/5] Abuluwefa1997_Article_OxidationOfLowCarbon.pdf https://link.springer.com/article/10.1007/s11661-997-0256-6.

[40] V. Basabe and J. Szpunar, "Phase Composition of Oxide Scales during Reheating in Hot Rolling of Low Carbon Steel," *Steel Research International,* vol. 27, *(11),* pp. 818–824, 2006. Available: https://internal-pdf://3450910723/31] Basabe Scale.pdf Phase - Composition Oxide https://onlinelibrary.wiley.com/doi/epdf/10.1002/srin.200606467 of.

[41] J. S. Sheasby, W. E. Boggs and E. T. Turkdogan, "Scale growth on steels at 1200Â°C: rationale of rate and morphology," *Metal Science,* vol. 18, *(3),* pp. 127–136, 1984. Available: https://internal-pdf://0674571203/44] download.pdf https://doi.org/10.1179/msc.1984.18.3.127.

[42] M. Landfahrer *et al*, "Numerical and experimental investigation of scale formation on steel tubes in a real-size reheating furnace," *Int. J. Heat Mass Transfer,* vol. 129, pp. 460–467, 2019. Available: https://internal-pdf://1323497691/20] 1-s2.0-S0017931018341632-main.pdf https://doi.org/10.1016/j.ijheatmasstransfer.2018.09.110.

[43] U. Unver and H. M. Unver, "Comparison of Natural Gas Fired and Induction Heating Furnaces," *Progress in Exergy, Energy, and the Environment,* pp. 1009–1016, 2014. Available: https://internal-pdf://2085503540/51] 2721884808000735144WHELFSWA0031764.pdf https://doi.org/10.1007/978-3-319-04681-5_96.

[44] M. Munday and K. Turner, "Steel manufacturing in wales: Ensuring a sustainable and prosperous future," University of Strathclyde Institutional Academic Repository, 2020Available: https://internal-pdf://3706070821/Munday_Turner_CEP_2020_Steel_manufacturing_in_.pdf https://pureportal.strath.ac.uk/en/publications/steel-manufacturing-in-wales-ensuring-a-sustainable-and-prosperou.

[45] A. Zhang *et al*, "Numerical study on thermal performance and thermal stress of molten salt receiver tube based on induction heating," *Appl. Therm. Eng.,* vol. 235, 2023. Available: https://internal-pdf://3920049333/304] 1-s2.0-S1359431123013820-main.pdf https://doi.org/10.1016/j.applthermaleng.2023.121353.

[46] Y. Zhao *et al*, "Influence of half open coil structures on overall continuous induction heating of variable cross section pipe before quenching," *Appl. Therm. Eng.,* vol. 261, 2025. Available: https://internal-pdf://3671017675/303] 1-s2.0-S1359431124027431-main.pdf https://doi.org/10.1016/j.applthermaleng.2024.125075.

[47] N. Schmitz *et al*, "Towards CO2-neutral process heat generation for continuous reheating furnaces in steel hot rolling mills â“ A case study," *Energy,* vol. 224, 2021. Available: https://internal-pdf://0297687057/42] 1-s2.0-S0360544221004047-main.pdf https://doi.org/10.1016/j.energy.2021.120155.

[48] Z. Feng *et al*, "Flexible intelligent thermal management systems: Sensing devices, signals, and applications," *Nano Energy,* vol. 138, 2025. Available: https://internal-pdf://1731086298/308] 1-s2.0-S2211285525002010-main.pdf https://doi.org/10.1016/j.nanoen.2025.110842.

[49] B. Drobenko *et al*, "Rational approaches to high temperature induction heating," *Int. J. Eng. Sci.,* vol. 117, pp. 34–50, 2017. Available: https://internal-pdf://1869608584/284] 1-s2.0-S0020722516316391-main.pdf https://doi.org/10.1016/j.ijengsci.2017.05.001.

[50] M. Krzyzanowski and J. H. Beynon, "Modelling the boundary conditions for thermo**mechanical processing - oxide scale behaviour and composition effects**," *Modell Simul Mater Sci Eng,* vol. 8, *(6),* pp. 927–945, 2000. Available: https://internal-pdf://1732366222/19] M_Krzyzanowski_2000_Modelling_Simul._Mate.pdf https://doi.org/10.1088/0965-0393/8/6/312.

[51] L. Sun and W. Yan, "Prediction of wall temperature and oxide scale thickness of ferriticâ□“ martensitic steel superheater tubes," *Appl. Therm. Eng.,* vol. 134, pp. 171–181, 2018. Available: https://internal-pdf://2823142844/108] 1-s2.0-S1359431117374604-main.pdf https://doi.org/10.1016/j.applthermaleng.2018.01.127.

[52] T. Steel, "InstallÂ® plus 235 & inlineâ□¢ 265: Hot-part-2 PED & high temperature carbon steel tubes for building & industrial services," 2021Available: https://Tubes Inline & Steel Plus - internal-pdf://2495839765/Tata Install https://www.tatasteeleurope.com/construction/products/tube/conveyance 235 2.pdf.

[53] G. K. Burgess and P. D. Foote, "The emissivity of metals and oxides. IV. Iron oxide," vol. 12, pp. 83–89, 1915. Available: https://internal-pdf://3820995878/118] nbsbulletinv12n1p83_A2b.pdf https://archive.org/details/emiss1283891915249249unse/page/n1/mode/2up.

[54] J. Armitt *et al*, "Spalling of steam-grown oxide from superheater and reheater tube steels. technical planning study 76-655. final report," Central Electricity Research Laboratories, Leatherhead, Surrey, UK, 1978Available: https://internal-pdf://2740156145/229] download.pdf https://www.osti.gov/servlets/purl/5047517/.

[55] U. L. Tata Steel, "Advances being made through Electric Arc Furnaces," vol. 2025, 2024. Available: https://www.tatasteeluk.com/corporate/news/advances-being-made-through-electric-arc-furnaces.

[56] W. Xia *et al*, "Recent research progress on recycling metallurgical waste slag and strengthening directional recovery of impurity elements by applied electric field," *Chem. Eng. J.,* vol. 499, 2024. Available: https://internal-pdf://0391173666/364] 1-s2.0-S1385894724080537-main.pdf https://doi.org/10.1016/j.cej.2024.156562.

[57] &. R. Farahat *et al*, "Reduction of mill scale generated by steel processing," *Steel Grips,* vol. 8, pp. 88–92, 2010. Available: https://www.researchgate.net/publication/288874180_Reduction_of_mill_scale_generated_by_steel_processing.

[58] M. Dubar *et al*, "Multi-scale approach to high-temperature impact of oxides and worn geometries on tribological behaviour at the part-tool interface," *Wear,* vol. 570, 2025. Available: https://internal-pdf://3023367136/368] 1-s2.0-S0043164825002273-main.pdf https://doi.org/10.1016/j.wear.2025.205958.

[59] A. Raj *et al*, "Evaluating hydrogen gas transport in pipelines: Current state of numerical and experimental methodologies," *Int J Hydrogen Energy,* vol. 67, pp. 136–149, 2024. Available: https://internal-pdf://1338931705/326] 1-s2.0-S0360319924014137-main.pdf https://doi.org/10.1016/j.ijhydene.2024.04.140.

[60] H. Nykyforchyn *et al*, "Pipeline durability and integrity issues at hydrogen transport via natural gas distribution network," *Procedia Structural Integrity,* vol. 33, pp. 646–651, 2021. Available: https://internal-pdf://1378837299/328] 1-s2.0-S2452321621001669-main.pdf https://doi.org/10.1016/j.prostr.2021.10.071.

[61] J. Liu *et al*, "A comprehensive review on hydrogen permeation barrier in the hydrogen transportation pipeline: Mechanism, application, preparation, and recent advances," *Int J Hydrogen Energy,* vol. 101, pp. 504–528, 2025. Available: https://internal-pdf://3885983327/325] 1-s2.0-S0360319924055927-main.pdf https://doi.org/10.1016/j.ijhydene.2024.12.379.

[62] C. Tsiklios, M. Hermesmann and T. E. Muller, "Hydrogen transport in large-scale transmission pipeline networks: Thermodynamic and environmental assessment of repurposed and new pipeline configurations," *Appl. Energy,* vol. 327, 2022. Available: https://internal-pdf://2690586869/327] 1-s2.0-S030626192201354X-main.pdf https://doi.org/10.1016/j.apenergy.2022.120097.

[63] T. Rubben *et al*, "Scanning Kelvin probe force microscopy study of the effect of thermal oxide layers on the hydrogen release - Experiments and finite element method modelling," *Int J Hydrogen Energy,* vol. 48, *(87),* pp. 34067–34076, 2023. Available: https://internal-pdf://1051468561/341] 1-s2.0-S0360319923024382-main.pdf https://doi.org/10.1016/j.ijhydene.2023.05.142.

[64] L. Vecchi *et al*, "A modelling approach on the impact of an oxide layer on the hydrogen permeation through iron membranes in the Devanathan-Stachurski cell," *Electrochim. Acta,* vol. 286, pp. 139–147, 2018. Available: https://internal-pdf://1297538357/340] 1-s2.0-S0013468618317894-main.pdf https://doi.org/10.1016/j.electacta.2018.08.022.

[65] K. Stylidis, C. Wickman and R. Soderberg, "Defining Perceived Quality in the Automotive Industry: An Engineering Approach," *Procedia CIRP,* vol. 36, pp. 165–170, 2015. Available: https://internal-pdf://0849882554/329] 1-s2.0-S2212827115006034-main.pdf https://doi.org/10.1016/j.procir.2015.01.076.

[66] M. F. Hussin and B. Wang, "Industrial safety perception among post-graduate engineering students," *Knowledge-Based Syst.,* vol. 23, *(8),* pp. 769–771, 2010. Available: https://internal-pdf://4276668024/330] 1-s2.0-S0950705110000729-main.pdf https://doi.org/10.1016/j.knosys.2010.04.013.

[67] R. Amaya-Gomez *et al*, "An analysis of engineering students' risk perception to support process safety learning process," *Education for Chemical Engineers,* vol. 42, pp. 7–19, 2023. Available: https://internal-pdf://0790587948/331] 1-s2.0-S1749772822000252-main.pdf https://doi.org/10.1016/j.ece.2022.10.003.

[68] M. Cai *et al*, "Risk Perception and Product Safety in User-Centered Design," *ASME 2019 International Design Engineering Technical Conferences and Computers and Information in Engineering Conference,* vol. olume 7: 31st International Conference on Design Theory and Methodology, 2019. Available: https://internal-pdf://4114683301/334] 2893443495000735144WHELFSWA0037759.pdf https://doi.org/10.1115/DETC2019-98371.

[69] M. SchÃ¼tze, P. F. Tortorelli and I. G. Wright, "Development of a Comprehensive Oxide Scale Failure Diagram," *Oxidation Metals,* vol. 73, pp. 389–418, 2010. Available: https://internal-pdf://1781202266/115] s11085-009-9185-7.pdf https://link.springer.com/article/10.1007/s11085-009-9185-7.

[70] P. K. Imbrie and D. C. Lagoudas, "Morphological Evolution of TiO2 Scale Formed on Various 1D and 2D Geometries of Titanium," *Oxidation Metals,* vol. 55, *(4),* pp. 359–399, 2001. Available: https://internal-pdf://0119167552/160] A_1010368412822.pdf https://link.springer.com/article/10.1023/A:1010368412822.

[71] R. Dewfall, "Passivation Layers of Ultra-Advanced High Strength Steels and High Strength Steels." Eng. D, Swansea University, 2024.

[72] J. Richards, "The Effect of Cold Roller-Bending on the Mechanical & Geometric Properties of Steel Hollow Sections." Ph.D, Swansea University, 2019.

[73] M. Krzyzanowski, J. H. Beynon and D. C. J. Farrugia, "A pivotal role of secondary oxide scale during hot rolling and for subsequent product quality," in *Oxide Scale Behaviour in High Temperature Metal Processing*Anonymous 2010, Available: https://in HT behaviour processing.pdf internal-pdf://2262551539/Scale metal. DOI: 10.1002/9783527630318.

[74] M. Krzyzanowski and J. H. Beynon, "The tensile failure of mild steel oxides under hot rolling conditions," *Steel Research International,* vol. 70, pp. 22–27, 1999. Available: https://Th.pdf internal-pdf://3390640852/60] Steel - Research Krzyzanowski https://onlinelibrary.wiley.com/doi/pdf/10.1002/srin.199905596 2016.

[75] Z. Y. Jiang *et al*, "Analysis of tribological feature of the oxide scale in hot strip rolling," *Tribol. Int.,* vol. 43, pp. 1339–1345, 2010. Available: https://internal-pdf://2767975041/57] 1-s2.0-S0301679X10000022-main.pdf https://doi.org/10.1016/j.triboint.2009.12.070.

[76] P. A. Schweitzer, "Coatings," in *Corrosion Engineering Handbook. Corrosion of Linings and Coatings : Cathodic and Inhibitor Protection and Corrosion Monitoring,* 2nd ed.Anonymous 2007, Available: https://ifind.swansea.ac.uk/permalink/44WHELF_SWA/1jlslid/alma998473166202417.

[77] F. Matsuno, "Blistering and Hydraulic Removal of Scale Films of Rimmed Steel at High Temperature," *Iron and Steel Institute of Japan (ISIJ) International,* vol. 20, pp. 413–421, 1980. Available: https://doi.org/10.2355/isijinternational1966.20.413 al.pdf et Matsuno internal-pdf://2793122124/37].

[78] J. H. Lee *et al*, "Spallation analysis of oxide scale on low carbon steel," *Materials Science and Engineering: A,* vol. 676, pp. 385–394, 2016. Available: https://internal-pdf://1501231201/28] 1-s2.0-S0921509316310759-main.pdf https://doi.org/10.1016/j.msea.2016.09.012.

[79] N. N. Kalasin, S. Yenchum and T. Nilsonthi, "Adhesion behaviour of scales on hot-rolled steel strips produced from continuous casting slabs," *Materials Today: Proceedings,* vol. 5, *(3),* pp. 9359–9367, 2018. Available: https://internal-pdf://3478939609/26] 1-s2.0-S221478531732134X-main.pdf https://doi.org/10.1016/j.matpr.2017.10.111.

[80] M. Kendall *et al*, "In Situ Thermogravimetric Analysis of Curved Surfaces During High-Temperature Oxidation," *Materials,* vol. 18, *(11),* 2025. Available: https://internal-pdf://3792727575/materials-18-02463.pdf https://doi.org/10.3390/ma18112463.

[81] J. M. Hulley and R. Rolls, "High-Temperature Cohesion and Adhesion of Oxide Scales on Mild Steel," *The Journal of the Iron and Steel Institute,* vol. 208, 1970. Available: https://internal-pdf://0463166096/54] 38896789600002417.pdf.

[82] L. Xu *et al*, "Microstructure evolution and deformation mechanism along the thickness of heavy-wall ferrite-bainite dual-phase offshore pipelines by the progressive forming process," *J. Mater. Process. Technol.,* vol. 326, 2024. Available: https://internal-pdf://2047796878/190] 1-s2.0-S0924013624000736-main.pdf https://doi.org/10.1016/j.jmatprotec.2024.118355.

[83] A. M. Huntz and M. SchÃ¼tze, "Stresses generated during oxidation sequences and high temperature fracture," *Materials at High Temperatures,* vol. 12, *(2-3),* pp. 151–161, 1994. Available: https://internal-pdf://1116743801/211] 22884057_43506209740002417.pdf https://doi.org/10.1080/09603409.1994.11689481.

[84] S. Samal and S. K. Mitra, "Influence of Grain Shape, Size, and Grain Boundary Diffusion on High-Temperature Oxidation of Pure Metal Fe, Cu, and Zn," *Metallurgical and Materials Transactions A,* vol. 46, pp. 3324â□“ 3332, 2015. Available: https://internal-pdf://1466441525/186] s11661-015-2987-0.pdf https://doi.org/10.1007/s11661-015-2987-0.

[85] J. Takada *et al*, "Determination of diffusion coefficient of oxygen in Î³-iron from measurements of internal oxidation in Fe-Al alloys," *Metallurgical Transaction A,* vol. 17, pp. 221–229, 1986. Available: https://internal-pdf://1401506665/153] 41342630750002417.pdf https://link.springer.com/article/10.1007/BF02643898.

[86] N. B. Pilling and R. E. Bedworth, "The Oxidation of Metals at High Temperature," *Journal of the Institute of Metals,* vol. 29, pp. 529–591, 1923. Available: https://internal-pdf://3614294650/206] 22867214_43490882190002417.pdf.

[87] H. E. Evans, "The role of oxide grain boundaries in the development of growth stresses during oxidation," *Corros. Sci.,* vol. 23, *(5),* pp. 495–506, 1983. Available: https://internal-pdf://2772557822/207] 22874724_43498818230002417.pdf https://doi.org/10.1016/0010-938X(83)90099-9.

[88] D. J. Srolovitz and T. A. Ramanarayanan, "An elastic analysis of growth stresses during oxidation," *Oxidation Metals,* vol. 22, *(4),* pp. 133–146, 1984. Available: https://internal-pdf://1367798523/204] 22866719_43490626170002417.pdf https://doi.org/10.1007/BF00656901.

[89] D. R. Clarke, "Stress generation during high-temperature oxidation of metallic alloys," *Current Opinion in Solid State and Materials Science,* vol. 6, *(3),* pp. 237–244, 2002. Available: https://internal-pdf://2297916987/223] 1-s2.0-S1359028602000748-main.pdf https://doi.org/10.1016/S1359-0286(02)00074-8.

[90] D. R. Clarke, "The lateral growth strain accompanying the formation of a thermally grown oxide," *Acta Materialia,* vol. 51, *(5),* pp. 1393–1407, 2003. Available: https://internal-pdf://4011484012/222] 1-s2.0-S1359645402005323-main.pdf https://doi.org/10.1016/S1359-6454(02)00532-3.

[91] W. Noh *et al*, "Effects of the residual stress, interfacial roughness and scale thickness on the spallation of oxide scale grown on hot rolled steel sheet," *Materials Science and Engineering: A,* vol. 739, pp. 301–316, 2019. Available: https://internal-pdf://3535853280/29] 1-s2.0-S0921509318313261-main (1).pdf https://doi.org/10.1016/j.msea.2018.10.009.

[92] C. Wagner, "Diffusion and high temperature oxidation of metals," in *Atom Movements*Anonymous 1951, Available: https://internal-pdf://3704442491/194] 42506230860002417.pdf.

[93] Sch, ü and M. tze, "Mechanical properties of oxide scales," *Oxidation of Metals,* vol. 44, *(1-2),* pp. 29–61, 1995. Available: https://www.proquest.com/docview/1688521986. DOI: 10.1007/BF01046722.

[94] P. Hancock and J. R. Nicholls, "Application of fracture mechanics to failure of surface oxide scales," *Materials Science and Technology,* vol. 4, *(5),* pp. 398–406, 1988. Available: https://www.tandfonline.com/doi/abs/10.1179/mst.1988.4.5.398. DOI: 10.1179/mst.1988.4.5.398.

[95] P. Hancock, J. R. Nicholls and K. Mahmood, "The influence of imposed strain rate on fracture of surface oxides," *Corrosion Science,* vol. 35, *(5),* pp. 979,983–981,987, 1993. Available: https://dx.doi.org/10.1016/0010-938X(93)90316-9. DOI: 10.1016/0010-938X(93)90316-9.

[96] S. R. K. Iyengar and R. K. Jain, "Solution of equations and eigen value problems," in *Numerical Methods,*Anonymous 2009, Available: https://ifind.swansea.ac.uk/permalink/44WHELF_SWA/1jlslid/alma998288699302417.

[97] D.R. Clarke and W. Pompe, "Critical radius for interface separation of a compressively stressed film from a rough surface," *Acta Materialia,* vol. 47, *(6),* pp. 1749–1756, 1999. . DOI: 10.1016/s1359-6454(99)00078-6.

[98] G. Allegri, "A unified formulation for fatigue crack onset and growth via cohesive zone modelling," *Journal of the Mechanics and Physics of Solids,* vol. 138, pp. 103900, 2020. Available: https://dx.doi.org/10.1016/j.jmps.2020.103900. DOI: 10.1016/j.jmps.2020.103900.

[99] Y. Hidaka, T. Anraku and N. Otsuka, "Deformation of Iron Oxides upon Tensile Tests at 600â“ 1250Â°C," *Oxidation Metals,* vol. 59, pp. 97–113, 2003. Available: https://internal-pdf://0344357891/227] A_1023070016230.pdf https://doi.org/10.1023/A:1023070016230.

[100] A. S. Sabau and I. G. Wright, "On the estimation of thermal strains developed during oxide growth," *J. Appl. Phys.,* vol. 106, 2009. Available: https://internal-pdf://2228629419/120] 1.3157199.pdf https://doi.org/10.1063/1.3157199.

[101] J. Gavarri and C. Carel, "The complex nonstoichiometry of wÃ¼stite Fe1-zO: Review and comments," *Progress in Solid State Chemistry,* vol. 53, pp. 27–49, 2019. Available: https://internal-pdf://1988643339/101] 1-s2.0-S0079678618300281-main.pdf https://doi.org/10.1016/j.progsolidstchem.2018.10.001.

[102] K. Schneider and M. Rekas, "High temperature creep of metal oxides," in *InTech eBooks*Anonymous 2018, Available: https://library.biblioboard.com/viewer/1b8af2fb-f571-42fa-b674-28ae158dd7b0. DOI: 10.5772/intechopen.70876.

[103] R. M. Hazen and R. Jeanloz, "WÃ¼stite (Fe1-x O): A review of its defect structure and physical properties," *Rev. Geophys.,* vol. 22, *(1),* pp. 37–46, 1984. Available: https://February https://doi.org/10.1029/RG022i001p00037 -.pdf - internal-pdf://3179160996/125] 1984 Geophysics Reviews of.

[104] K. Dohda *et al*, "Tribology in metal forming at elevated temperatures," *Friction,* vol. 3, *(1),* pp. 1–27, 2015. Available: https://link.springer.com/article/10.1007/s40544-015-0077-3. DOI: 10.1007/s40544-015-0077-3.

[105] M. Schutze, "Deformation behaviour and deformation mechanisms in oxides," in *Protective Oxide Scales and their Breakdown*Anonymous 1997, .

[106] E. Jolles and C. Monty, "High temperature creep of Fe1−xO," *Philosophical Magazine. A, Physics of Condensed Matter. Defects and Mechanical Properties,* vol. 64, *(4),* pp. 765–775, 1991. Available: https://www.tandfonline.com/doi/abs/10.1080/01418619108213946. DOI: 10.1080/01418619108213946.

[107] B. Picque *et al*, "Mechanical behaviour of iron oxide scale: Experimental and numerical study," *Wear,* vol. 260, *(3),* pp. 231–242, 2006. Available: https://internal-pdf://1128042090/255] 1-s2.0-S0043164805003832-main.pdf https://doi.org/10.1016/j.wear.2005.03.037.

[108] J. I. Asperheim *et al*, "Numerical simulation of high-frequency induction welding in longitudinal welded tubes," *Journal of Mathematics in Industry,* vol. 14, *(10),* 2024. Available: https://internal-pdf://2503665351/305] s13362-024-00147-8.pdf https://doi.org/10.1186/s13362-024-00147-8.

[109] Y. Murakami, "Cracks in a circular plate or in a cylinder," in *Stress Intensity Factors Handbook,*Anonymous 1987, Available: https://internal-pdf://2523136119/232] 23121602_43752002740002417.pdf https://ifind.swansea.ac.uk/permalink/44WHELF_SWA/1jlslid/alma993372343402417.

[110] S. D. Antolovich, A. Saxena and W. W. Gerberich, "Fracture mechanics – An interpretive technical history," *Mechanics Research Communications,* vol. 91, pp. 46–86, 2018. Available: https://dx.doi.org/10.1016/j.mechrescom.2018.03.003. DOI: 10.1016/j.mechrescom.2018.03.003.

[111] W. Li *et al*, "Temperature-dependent elastic modulus model for metallic bulk materials," *Mech. Mater.,* vol. 139, 2019. Available: https://internal-pdf://3422150574/224] 1-s2.0-S0167663618303788-main.pdf https://doi.org/10.1016/j.mechmat.2019.103194.

[112] W. Koster, "Die TemperaturabhÃ¤ngigkeit des blastizitÃ¤tsmoduls reiner Metalle," *International Journal of Materials Research,* vol. 39, *(1),* pp. 1–9, 2021. Available: https://internal-pdf://2703062031/234] 23149465_43776243830002417.pdf https://doi.org/10.1515/ijmr-1948-390101.

[113] C. A. Schneider, W. S. Rasband and K. W. Eliceiri, "NIH Image to ImageJ: 25 years of image analysis," *Nature Methods,* vol. 9, *(7),* pp. 671–675, 2012. Available: https://www.nature.com/articles/nmeth.2089.pdf. DOI: 10.1038/nmeth.2089.

[114] S. Birosca and R. L. Higginson, "Phase identification of oxide scale on low carbon steel," *Materials at High Temperatures,* vol. 22, *(4),* pp. 179–184, 2005. Available: https://internal-

pdf://1925761952/25] Phase_identification_of_oxide_.pdf https://www.proquest.com/scholarly-journals/phase-identification-oxide-scale-on-low-carbon/docview/1243348952/se-2?accountid=14680.

[115] B. Weiss *et al*, "Structural and morphological changes during reduction of hematite to magnetite and wustite in hydrogen rich reduction gases under fluidised bed conditions," *Ironmaking Steelmaking,* vol. 38, *(1),* pp. 65–73, 2011. Available: https://internal-pdf://0604682665/352] weiss-et-al-2011-structural-and-morpholo.pdf https://doi.org/10.1179/030192310X12700328926065.

[116] K. He, Z. Zheng and Z. Chen, "A numerical investigation on the hydrogen reduction of wÃ¼stite using a 2D mesoscale method," *Int J Hydrogen Energy,* vol. 47, *(12),* pp. 8118–8129, 2022. Available: https://internal-pdf://0675127987/351] 1-s2.0-S0360319921048540-main.pdf https://doi.org/10.1016/j.ijhydene.2021.12.154.

[117] J. Robertson and M. I. Manning, "Limits to adherence of oxide scales," *Materials Science and Technology,* vol. 6, *(1),* pp. 81–92, 1990. Available: https://internal-pdf://2532410999/221] 22954157_43615044430002417.pdf. DOI: 10.1179/mst.1990.6.1.81.

[118] H. Bidmus, J. Chau and K. Dechant, "Absolute Roughness of Pipes from Different Manufacturing and Treatment Methods and Impact on Pipeline Design," *PSIG Annual Meeting,* 2019. Available: https://onepetro.org/PSIGAM/proceedings-abstract/PSIG19/All-PSIG19/PSIG-1926/2124.

[119] P. P. Benham, R. J. Crawford and C. G. Armstrong, "Stress-strain relations," in *Mechanics of Engineering Materials*, 2nd ed.Anonymous 1996, .

[120] A. C. Kocabicak *et al*, "A deep neural network approach to predict dimensional accuracy of thin-walled tubes in backward flow forming plasticity process," *Journal of Manufacturing Processes,* vol. 141, pp. 59–80, 2025. Available: https://internal-pdf://2482917281/315] 1-s2.0-S152661252500194X-main.pdf https://doi.org/10.1016/j.jmapro.2025.02.044.

[121] T. Dutta *et al*, "Road Map of Semiconductor Metal-Oxide-Based Sensors: A Review," *Sensors,* vol. 23, *(15),* 2023. Available: https://internal-pdf://2356326152/335] Road-Map-of-Semiconductor-MetalOxideBase.pdf. DOI: 10.3390/s23156849.

[122] P. Kumbhakar *et al*, "Emerging 2D metal oxides and their applications," *Materials Today,* vol. 45, pp. 142–168, 2021. Available: https://internal-pdf://2743207766/336] 1-s2.0-S1369702120304508-main.pdf https://doi.org/10.1016/j.mattod.2020.11.023.

[123] K. G. Gareev, "Diversity of Iron Oxides: Mechanisms of Formation, Physical Properties and Applications," *Magnetochemistry,* vol. 9, *(5),* 2023. Available: https://internal-pdf://0518377983/337] magnetochemistry-09-00119.pdf https://doi.org/10.3390/magnetochemistry9050119.

[124] T. J. T. van Rooij, "Modelling of the Oxidation of Iron with Steam in COMSOL 5.5 and MATLAB." , Eindhoven University of Technology, Eindhoven, The Netherlands, 2022.

[125] X. Dong, X. Feng and K. W. Hwang, "Oxidation stress evolution and relaxation of oxide film/metal substrate system," *J. Appl. Phys.,* vol. 112, 2012. Available: https://internal-pdf://0831204692/119] 1.4736934.pdf https://doi.org/10.1063/1.4736934.

[126] C. Asensio-Jimenez *et al*, "Effect of Specimen Thickness on the Oxidation Rate of High Chromium Ferritic Steels: The Significance of Intrinsic Alloy Creep Strength," *Oxidation Metals,* vol. 79, pp. 15–28, 2012. Available: https://internal-pdf://0558584462/250] s11085-012-9323-5.pdf https://doi.org/10.1007/s11085-012-9323-5.

[127] B. Ilschner, B. Reppich and E. Riecke, "High-temperature steady-state creep and atomic disorder in ironII oxide," *Discussions of the Faraday Society,* vol. 38, pp. 243–25, 1964. . DOI: 10.1039/df9643800243.

[128] O. A. Zambrano, J. J. Coronado and S. A. Rodriguez, "Mechanical properties and phases determination of low carbon steel oxide scales formed at 1200 Â°C in air," *Surface and Coatings Technology,* vol. 282, pp. 155–162, 2015. Available: https://internal-pdf://0084879952/55] 1-s2.0-S0257897215303248-main.pdf https://doi.org/10.1016/j.surfcoat.2015.10.028.

[129] G. D. West, S. Birosca and R. L. Higginson, "Phase determination and microstructure of oxide scales formed on steel at high temperature," *J. Microsc.,* vol. 217, *(2),* pp. 122–129, 2005. Available: https://internal-pdf://3076683279/9] https://doi.org/10.1111/j.1365-2818.2005.01409.x Microscopy - 2005 Phas.pdf WEST Journal of.

[130] R. Y. Chen and W. Y. D. Yeun, "Review of the High-Temperature Oxidation of Iron and Carbon Steels in Air or Oxygen," *Oxidation Metals,* vol. 59, pp. 433–468, 2003. Available: https://internal-pdf://4034006109/3] Chen-Yeun2003_Article_ReviewOfTheHigh-Temp.pdf https://link.springer.com/article/10.1023/A:1023685905159.

[131] S. Foorginezhadab *et al*, "Recent Advances in Sensing and Assessment of Corrosion in Sewage Pipelines," *Process Saf. Environ. Prot.,* vol. 147, pp. 192–213, 2021. Available: https://internal-pdf://0537710289/53] 1-s2.0-S0957582020317262-main.pdf https://doi.org/10.1016/j.psep.2020.09.009.

[132] P. Wang *et al*, "Enhancing oxide scale growth and adhesion via electrochemically regulating ion diffusion," *Journal of Materials Science & Technology,* vol. 158, pp. 133–144, 2023. Available: https://internal-pdf://0913201798/170] 1-s2.0-S1005030223002748-main.pdf https://doi.org/10.1016/j.jmst.2023.02.032.

[133] P. B. Entchev, D. C. Lagoudas and J. C. Slattery, "Effects of non-planar geometries and volumetric expansion in the modeling of oxidation in titanium," *Int. J. Eng. Sci.,* vol. 39, *(6),* pp. 695–714, 2001. Available: https://internal-pdf://0549157890/143] 1-s2.0-S0020722500000537-main.pdf https://doi.org/10.1016/S0020-7225(00)00053-7.

[134] P. De *et al*, "Role of porosity and diffusion coefficient in porous electrode used in supercapacitors â□" Correlating theoretical and experimental studies," *Electrochemical Science Advances,* vol. 3, *(1),* 2023. Available: https://Electrochemical 2022 - De.pdf https://doi.org/10.1002/elsa.202100159 internal-pdf://1371183031/178] Adv Science.

[135] H. Evans *et al*, "The influence of a titanium nitride dispersion on the oxidation behavior of 20%Cr-25%Ni stainless steel," *Oxidation Metals,* vol. 12, pp. 473–485, 1978. Available: https://api.semanticscholar.org/CorpusID:135705778.

[136] J. Wang *et al*, "Effect of microstructure and microtexture evolution of oxide layer over J82B steel on mechanical descaling properties," *Materials Today Communications,* vol. 37, 2023. Available: https://internal-pdf://0264771587/353] 1-s2.0-S2352492823017701-main.pdf https://doi.org/10.1016/j.mtcomm.2023.107079.

[137] D. Poirier *et al*, "High Temperature Oxidation of Steel in an Oxygen-enriched Low NOX Furnace Environment," *IFRF Combustion Journal,* 2006. Available: https://internal-pdf://1343152361/79] High_Temperature_Oxidation_of_Steel_in_a.pdf https://www.academia.edu/19759388/High_Temperature_Oxidation_of_Steel_in_an_Oxygen_enriched_Low_NOX_Furnace_Environment.

[138] A. Paul, "The Kirkendall Effect in Solid-State Diffusion." , Eindhoven University of Technology, Eindhoven, The Netherlands, 2004.

[139] Anonymous "Definition and classification of grades of steel," 2000. Available: https://EN 10020-2000--2022-03-11--09-50-22 AM].pdf internal-pdf://4285271714/BS https://bsol.bsigroup.com/Bibliographic/BibliographicInfoData/000000000030015678.

[140] R. E. Smallman and A. H. W. Ngan, "Phase diagrams and alloy theory," in *Modern Physical Metallurgy,* 8th ed.Anonymous 2014, Available: https://ifind.swansea.ac.uk/permalink/44WHELF_SWA/144jshv/alma998192493702417.

[141] Anonymous "Welded steel tubes for pressure purposes - Technical delivery conditions (Part 2: Electric welded non-alloy and alloy steel tubes with specified elevated temperature properties)," 2019. Available: https://PM].pdf 10217-2-2019--2022-01-06--02-30-34 EN internal-pdf://2539206761/BS https://bsol.bsigroup.com/Bibliographic/BibliographicInfoData/000000000030438140.

[142] J. Philibert, "Diffusion and drift in alloys and compounds," in *Atom Movements: Diffusion and Mass Transport in Solids.*Anonymous 1991, Available: https://ifind.swansea.ac.uk/permalink/44WHELF_SWA/1sssfk8/alma998611634202417.

[143] D. C. Lagoudas and Z. Ding, "Numerical computation of metal oxidation problems on bounded domains," *Int. J. Eng. Sci.,* vol. 36, *(4),* pp. 367–381, 1998. Available: https://internal-pdf://2452212394/201] 1-s2.0-S002072259700075X-main.pdf https://doi.org/10.1016/S0020-7225(97)00075-X.

[144] Z. S. Basinski, W. Hume-Rothery and A. L. Sutton, "The lattice expansion of iron," *Proceedings of the Royal Society A,* vol. 229, pp. 459–467, 1955. Available: https://internal-pdf://0712589242/237] basinski-et-al-1997-the-lattice-expansio.pdf https://doi.org/10.1098/rspa.1955.0102.

[145] J. B. Wachtman *et al*, "Exponential Temperature Dependence of Young's Modulus for Several Oxides," *Physical Review,* vol. 122, *(6),* 1961. Available: https://internal-pdf://2983703108/278] PhysRev.122.1754.pdf https://doi.org/10.1103/PhysRev.122.1754.

[146] O. L. Anderson, "Derivation of Wachtman's Equation for the Temperature Dependence of Elastic Moduli of Oxide Compounds," *Physical Review,* vol. 144, *(2),* pp. 553–557, 1966. Available: https://internal-pdf://0512496931/279] PhysRev.144.553.pdf https://doi.org/10.1103/PhysRev.144.553.

[147] G. N. Vigilante *et al*, "Elevated Temperature Properties of Steels," 1996. Available: https://internal-pdf://3469466835/307] ADA317919.pdf https://ntrl.ntis.gov/NTRL/dashboard/searchResults/titleDetail/ADA317919.xhtml.

[148] V. A. Drebushchak, "Thermal expansion of solids: review on theories," *Journal of Thermal Analysis and Calorimetry,* vol. 142, pp. 1097–1113, 2020. Available: https://internal-pdf://1941890896/236] s10973-020-09370-y.pdf https://link.springer.com/article/10.1007/s10973-020-09370-y#Sec18.

[149] Z. Zhang, "The characteristics and reduction of wustite," in *Iron Ores and Iron Oxides*, B. Kumar, Ed. 2023, Available: https://directory.doabooks.org/handle/20.500.12854/135114. DOI: 10.5772/intechopen.1001051.

[150] Q. Wu *et al*, "Softening and Melting of Wüstite: Insights from a Multiscale Study," *Metall Mater Trans B,* vol. 55, *(5),* pp. 3034–3041, 2024. Available: https://link.springer.com/article/10.1007/s11663-024-03242-8. DOI: 10.1007/s11663-024-03242-8.

[151] R. S. Molla, "A Study on Manufacturing of Deformed Bar (G 60-400W) at Elite Iron and Steel Industries." , International University of Business Agriculture and Technology, 2018.

[152] I. Jung, "Overview of the applications of thermodynamic databases to steelmaking processes," *Calphad,* vol. 34, *(3),* pp. 332–362, 2010. Available: https://internal-pdf://3470982967/13] 1-s2.0-S0364591610000441-main.pdf.

[153] H. Pauna *et al*, "Optical emission spectroscopy as a method to improve process automation of electric arc furnaces and ladle furnaces," *14th IFAC Workshop on Intelligent Manufacturing Systems*

IMS 2022, vol. 55, 2022. Available: https://internal-pdf://0750533825/99] 1-s2.0-S2405896322001744-main.pdf. DOI: 10.1016/j.ifacol.2022.04.173.

[154] W. J. Quadakkers, J. Zurek and M. Hansel, "Effect of water vapor on high-temperature oxidation of FeCr alloys," *The Journal of the Minerals, Metals & Materials Society,* vol. 61, pp. 44–50, 2009. Available: https://internal-pdf://0286086891/359] s11837-009-0102-y.pdf https://link.springer.com/article/10.1007/s11837-009-0102-y.

[155] M. Woodcox, J. Young and M. Smeu, "Ab initio investigation of the temperature-dependent elastic properties of Bi, Te and Cu," *Journal of Physics: Condensed Matter,* vol. 32, *(48),* 2020. Available: https://internal-pdf://2216968690/356] Woodcox_2020_J._Phys.__Condens._Matter_3.pdf.

[156] M. Hayakawa, J. B. Cohen and T. B. Reed, "Measurement of the Lattice Parameter of Wustite at High Temperatures," *J Am Ceram Soc,* vol. 55, *(3),* pp. 160–164, 1972. Available: https://internal-pdf://0743448474/240] 23228791_43840117530002417.pdf https://doi.org/10.1111/j.1151-2916.1972.tb11243.x.

[157] J. Redden, "Chapter 9: Sequences, series, and the binomial theorem," in *Advanced Algebra*Anonymous 2012, Available: https://open.umn.edu/opentextbooks/textbooks/1248.

[158] X. G. Lu, M. Selleby and B. Sundman, "Assessments of molar volume and thermal expansion for selected bcc, fcc and hcp metallic elements," *Calphad,* vol. 29, *(1),* pp. 68–89, 2005. Available: https://internal-pdf://0684907383/121] 1-s2.0-S0364591605000362-main.pdf https://doi.org/10.1016/j.calphad.2005.05.001.

[159] X. G. Lu, M. Selleby and B. Sundman, "Theoretical modeling of molar volume and thermal expansion," *Acta Materialia,* vol. 53, *(8),* pp. 2259–2272, 2005. Available: https://internal-pdf://3042822868/122] 1-s2.0-S1359645405000613-main.pdf https://doi.org/10.1016/j.actamat.2005.01.049.

[160] O. M. Fabrichnaya and B. Sundman, "The assessment of thermodynamic parameters in the Feî—¸O and Feî—¸Siî—¸O systems," *Geochim. Cosmochim. Acta,* vol. 61, *(21),* pp. 4539–4555, 1997. Available: https://internal-pdf://0284550829/68] 1-s2.0-S0016703797002561-main.pdf https://doi.org/10.1016/S0016-7037(97)00256-1.

[161] Y. M. Kozlovskii and S. V. Stankus, "The linear thermal expansion coefficient of iron in the temperature range of 130â□“ 1180 K," *Journal of Physics: Conference Series,* vol. 1382, 2019. Available: https://internal-pdf://3942401761/225] The_linear_thermal_expansion_coefficient.pdf. DOI: 10.1088/1742-6596/1382/1/012181.

[162] P. P. Benham, R. J. Crawford and C. G. Armstrong, "Appendix C: Table of mechanical properties of engineering materials," in *Mechanics of Engineering Materials*, 2nd ed.Anonymous 1996, .

[163] S. R. K. Iyengar and R. K. Jain, "Numerical differentiation and integration," in *Numerical Methods,*Anonymous 2009, Available: https://ifind.swansea.ac.uk/permalink/44WHELF_SWA/1jlslid/alma998288699302417.

[164] M. Jackson, "Periodic table Advanced : Atomic, Physical, Chemical Properties & Natural Isotopes," 2015. Available: https://ifind.swansea.ac.uk/permalink/44WHELF_SWA/1jlslid/alma998360496202417.

[165] W. C. Young, R. G. Budynas and A. M. Sadegh, "Stress and strain: Important relationships," in *Roark's Formulas for Stress and Strain,* 8th ed.Anonymous 2012, Available: https://www.accessengineeringlibrary.com/content/book/9780071742474/chapter/chapter2.

[166] I. Saeki *et al*, "In situ measurement of Youngâ□□s modulus of FeO scale formed on pure iron at 973â□“ 1273 K by acoustic resonance method," *Corros. Sci.,* vol. 53, *(1),* pp. 458–463, 2011. Available: https://internal-pdf://1796665933/214] 1-s2.0-S0010938X10004889-main.pdf https://doi.org/10.1016/j.corsci.2010.09.057.

[167] M. E. Fitzpatrick *et al*, "Determination of residual stresses by X-ray diffraction (measurement good practice guide no. 52)," National Physical Laboratory, Teddington, Middlesex, UK, 2005Available: https://internal-pdf://1875910112/242] mgpg52.pdf https://eprintspublications.npl.co.uk/2391/1/mgpg52.pdf.

[168] A. Sarmast *et al*, "Residual stress analysis in industrial parts: a comprehensive comparison of XRD methods," *J. Mater. Sci.,* vol. 58, pp. 16905–16929, 2023. Available: https://internal-pdf://2932192872/258] s10853-023-09069-z.pdf https://link.springer.com/article/10.1007/s10853-023-09069-z.

[169] P. Scherrer, "Bestimmung der GrÃ¶Ã□e und der inneren Struktur von Kolloidteilchen mittels RÃ¶ntgenstrahlen," 1918. Available: https://internal-pdf://4270382912/259] log15.pdf https://resolver.sub.uni-goettingen.de/purl?252457811_1918|log15.

[170] C. Suryanarayana and M. G. Norton, "Precise lattice parameter measurements," in *X-Ray Diffraction: A Practical Approach.*Anonymous 1998, Available: https://ifind.swansea.ac.uk/permalink/44WHELF_SWA/1sssfk8/alma998525880302417.

[171] H. M. Yin and P. Prieto-Munoz, "Stress transfer through fully bonded interface of layered materials," *Mech. Mater.,* vol. 62, pp. 69–79, 2013. Available: https://internal-pdf://1411742371/260] 1-s2.0-S0167663613000483-main.pdf https://doi.org/10.1016/j.mechmat.2013.03.007.

7 Appendices

Appendix 1: Methodology for quantifying oxide mechanical state, comprising thermal-, growth-, and manufacturing-related sources of stress.

Thermal Stress in the Oxide

Thermal stress was described by Huntz and Schütze in Equation 7.1 (where $\boldsymbol{E}, \boldsymbol{v}, \boldsymbol{\alpha}$, and $\boldsymbol{\delta}$ are the Elastic modulus, Poisson ratio, coefficient of thermal expansion, and thickness respectively). Elastic modulus and coefficient of thermal expansion are dependent on temperature, $\boldsymbol{T}$, due to increased atomic vibrations and change of lattice parameters with temperature [155].

$$\boldsymbol{\sigma_{ox,T}} = -\int_{T_f}^{T_i} \frac{\frac{\boldsymbol{E_{ox}(T)}}{\boldsymbol{(1-v_{ox})}}[\boldsymbol{\alpha_{ox}(T) - \alpha_m(T)}]}{\boldsymbol{1 + \frac{\delta_{ox}}{\delta_m}\frac{E_{ox}(T)}{E_m(T)}\left(\frac{1-v_m}{1-v_{ox}}\right)}} \boldsymbol{dT}$$

Equation 7.1

The oxide and metal elastic moduli temperature dependence can be expressed using Equation 7.2 and Equation 7.3, derived from linear gradient, $\boldsymbol{m}$ ('$\boldsymbol{ox}$' = oxide, '$\boldsymbol{m}$' = steel), and y-axis intercept, $\boldsymbol{E^0}$, values calculated using Li et al's data [111]. Their results agreed with results determined by other authors [112].

$$\boldsymbol{E_{ox}} = \boldsymbol{m_{ox}T} + \boldsymbol{E_{ox}}^{\boldsymbol{0}} \left[m = -0.0506 GPa.K^{-1};\ E_{ox}{}^{0} = 148 GPa\right]$$

Equation 7.2

$$\boldsymbol{E_m} = \boldsymbol{m_m T} + \boldsymbol{E_m}^{\boldsymbol{0}} \left[m = -0.0815 GPa.K^{-1};\ E_m{}^{0} = 224 GPa\right]$$

Equation 7.3

Volumetric thermal expansion coefficient, $\boldsymbol{\beta}$, is directly proportional to linear thermal expansion coefficient, $\boldsymbol{\alpha}$, since $\boldsymbol{\beta = 3\alpha}$ for isotropic materials, and the temperature-dependent lattice parameter, $\boldsymbol{a}$, can be used to determine volume at a given temperature (see Equation 7.4) [148]. A discontinuous linear function for temperature-dependent lattice parameter of iron was determined based on data collated by Basinski et al in the temperature range 1173-1673K [144]. Temperature-dependent lattice parameter data for wüstite were based on data from Hayakawa et al [156]. With the metal and oxide both having a linear variation in $\boldsymbol{a}$ with temperature, $\boldsymbol{T}$, (see Equation 7.5) a binomial expansion [157] was applied to Equation 7.5 to obtain an expression for $\boldsymbol{a^3}$, i.e. $\boldsymbol{a^3} = (\boldsymbol{pT+q})^3$, for volume (see Equation 7.6) in Equation 7.4. Although empirical functions exist which define $\boldsymbol{\alpha}$ as a polynomial function of temperature with empirical coefficients on each term [158], [159], use of an analytical expression for $\boldsymbol{\alpha}$ provides a more numerically stable solution.

$$\boldsymbol{\alpha} = \frac{\boldsymbol{1}}{\boldsymbol{3V}}\frac{\boldsymbol{dV}}{\boldsymbol{dT}} = \frac{\boldsymbol{1}}{\boldsymbol{3V}}\frac{\boldsymbol{d(a^3)}}{\boldsymbol{dT}}$$

Equation 7.4

$$\boldsymbol{a = pT + q}$$

$$\begin{aligned}\big[\boldsymbol{p_{oxide}} &= 79.5 \times 10^{-6}\text{Å}.K^{-1}; \boldsymbol{q_{oxide}} = 4.25\text{Å}; \boldsymbol{p_{metal}} = 22.2 \times 10^{-6}\text{Å}.K^{-1}; \boldsymbol{q_{metal}} \\ &= 2.89\text{Å}\ (273 \le T < 1173K); \boldsymbol{p_{metal}} = 82.0 \times 10^{-6}\text{Å}.K^{-1}; \boldsymbol{q_{metal}} \\ &= 2.77\text{Å}\ (1173 \le T \le 1673K);\big]\end{aligned}$$

Equation 7.5

$$\boldsymbol{V = a^3 = p^3T^3 + 3q^2pT^2 + 3pq^3T + q^3}$$

Equation 7.6

Furthermore, although quoted thermal expansion coefficient values are evaluated for linear scenarios, the scale of expansion is assumed small enough compared to the overall tube curvature to be linear at-scale. The coefficient of linear thermal expansion, $\boldsymbol{\alpha}$, at the normalisation temperature, was derived for both the metal substrate (Fe fcc) and oxide using the same literature as was used to collate molar volume data for the thermodynamic database in Kendall et al's model [7], [158]-[161].
Table 7.1 outlines the temperature-dependent mechanical properties of the oxide (wüstite) and metal at ambient ($\boldsymbol{T} = 298K$) and normalisation ($\boldsymbol{T} = 1273K$) conditions.

Table 7.1: Mechanical properties, (Elastic modulus, $\boldsymbol{E}$, Poisson ratio, $\boldsymbol{v}$, coefficient of thermal expansion, $\boldsymbol{\alpha}$) of the steel substrate and wüstite phase oxide scale evolved at ambient (298K) and tube normalisation (1273K) temperatures, $\boldsymbol{T}$ (assuming isobarothermal conditions).

	Wüstite		**Metal**	
$\boldsymbol{T}$	**298**	**1273**	**298**	**1273**
E (GPa)	130	83.6	200	120
$\boldsymbol{v}$ **(-)**	0.36 [50]	0.36	0.3 [162]	0.3
$\boldsymbol{\alpha}$ **(K^{-1})**	17.7×10^{-5}	15.0×10^{-5}	7.5×10^{-6}	21.4×10^{-5}

Numerical integration was used to solve Equation 7.1 via the composite Simpson's rule [163]. In this case, the function, $\boldsymbol{f(T)}$, is the integrand in Equation 7.1 which describes the thermal stress in the oxide, $\boldsymbol{\sigma_{ox,T}}$, where the independent variable is temperature, $\boldsymbol{T}$, and the numerical interval, $\boldsymbol{h}$, is defined across the tube manufacturing normalisation temperature bounds of the normalisation temperature, $\boldsymbol{T_{test}}$, and ambient temperature, $\boldsymbol{T_{ambient}}$, across an appropriate even number of intervals, $\boldsymbol{2n}$, (see Equation 7.7) defined by a convergence study. For the maximum oxide thickness predicted by Kendall et al's Thermo-Calc© model (2.2mm) on a 15 **n.b.** tube [7], the optimal number of intervals was not definitively determined as it exceeded the 100 intervals stipulated.

$$\boldsymbol{\sigma_{ox,T}} = \int_{\boldsymbol{T_{ambient}}}^{\boldsymbol{T_{test}}} \boldsymbol{f(T)\,dT} = \frac{\boldsymbol{h}}{\boldsymbol{3}}(\boldsymbol{f_0} + \boldsymbol{4f_1} + \boldsymbol{2f_2} + \boldsymbol{4f_3} + \boldsymbol{2f_4} + \cdots + \boldsymbol{4f_{n-1}} + \boldsymbol{f_n})$$

$$\boldsymbol{where\ h} = \frac{\boldsymbol{T_{test}} - \boldsymbol{T_{ambient}}}{\boldsymbol{2n}}$$

Equation 7.7

Growth Stress in the Oxide

Geometric stresses are most commonly predicted using Manning's analysis of the effect of geometry on oxide scale integrity, which can be used to predict strain in the oxide [20]. It should be noted that densities for both metal and oxide can easily be obtained from the molar volume, $\boldsymbol{V_0}$, values collated for the model thermodynamic database via molecular weight, $\boldsymbol{M_r}$, values in the same way that density for wüstite was derived when converting between thickness and mass gain during in-situ oxidation experiments described in Kendall et al's work [80] (see Equation 7.8). For the molecular weight of wüstite, the non-stoichiometric contribution of iron ('$\boldsymbol{1-x}$') is taken to be 0.92 [103], [164]. Table 7.2 shows these values collated. The same molecular weight theories were used to obtain volume fraction data from the mole fraction derived from the model.

Table 7.2: Molecular weights, $\boldsymbol{M_r}$, and densities, $\boldsymbol{\rho}$, of metal and oxide used to calculate growth strains.

$\boldsymbol{M_{r_{oxide}}}$ **(g)**	67.38
$\boldsymbol{M_{r_{metal}}}$ **(g)**	55.85

ρ_{oxide} (g.cm^{-3})	5.91
ρ_{metal} (g.cm^{-3})	8.33

$$M\rho = \frac{M_r}{V_0}$$

Equation 7.8

In extending the analysis to curved surfaces (see Figure 7.1), it is assumed that curvature is unidirectional and uniform oxidation of smooth micro-planar interfaces is assumed. Hoop stress, σ_h, is introduced because of the need to translate the existing bulk scale. This can be related to the radial stress, σ_r, acting across the interface via Equation 7.9.

$$\varphi h \sigma_h \simeq R\sigma_r$$

Equation 7.9

Huntz and Schütze then translated this information into expressions for oxide hoop, ε_{ox}^{h}, and radial, ε_{ox}^{r}, strains (see Equation 7.10 and Equation 7.11) [83].

$$\varepsilon_{ox}^{h} = -\frac{M}{R\varphi}d$$

Equation 7.10

$$\varepsilon_{ox}^{r} \approx \frac{d}{R}\varepsilon_{ox}^{h}$$

Equation 7.11

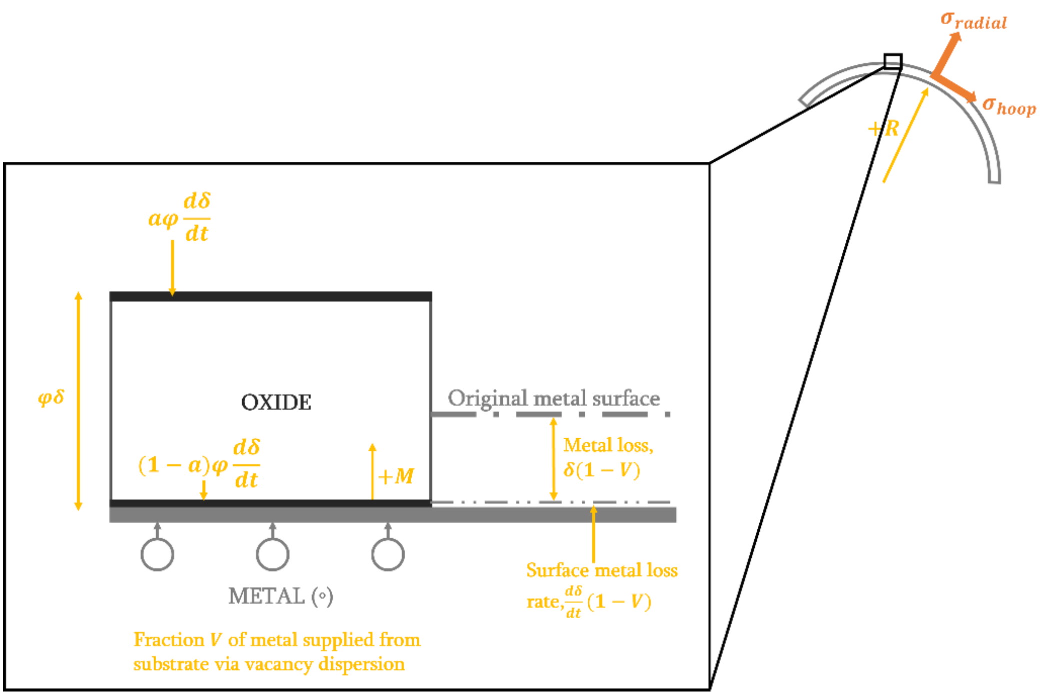

Figure 7.1: Dimensional theory for derivation of expression of geometric effect growth stress in oxide scale.

These strain values were converted to stress, $\boldsymbol{\sigma}$, using Equation 7.12 [90], [165] and a literature value of Elastic modulus, E, for wüstite measured using acoustic resonance (assuming isotropic properties)

[166]. The temperature dependence of Elastic modulus was accounted for using the method as in the thermal stress calculations.

$$\boldsymbol{\sigma} = \frac{\boldsymbol{E}}{\boldsymbol{1} - \boldsymbol{\upsilon}}\boldsymbol{\varepsilon}$$

Equation 7.12

Manufacturing Stress

Strain-induced elongations and contractions within a material's crystal lattice induce a change in interplanar spacing, causing a diffraction pattern shift [167]. Precise measurement of this shift allows the strain to be quantified. As such, the material's own interatomic planes can be used as internal strain gauges [167].

X-ray diffraction (**XRD**)-based measurements of residual stress were performed using the Pulstec μ-X360n apparatus at the University of Bristol was used comprising a chromium Kα ($\lambda = 2.2897$ Å) X-ray tube and 0.5mm collimator. Pre-normalised 15 **n.b.** tube samples were studied. Before taking any measurement, a stress-free iron reference sample was used to calibrate the X-ray machine. During all measurements, the **XRD** machine was positioned 39mm from the sample surface and held at an angle, $\boldsymbol{\psi}$, of 35±5° relative to the measurement surface. Samples were measured under computer control to a depth of 10μm which is well within the thickness of oxide observed on normalised samples in Kendall et al's work [80]. X-rays are exponentially attenuated by the sample material as soon as they are incident so the X-ray penetration depth is assumed to be where 63% of the reflection intensities originate from [168]. In the $\boldsymbol{cos\alpha}$ method, sample tilt, $\boldsymbol{\psi}$, and azimuthal, $\boldsymbol{\alpha}$, angle affect the penetration depth (for a given material and reflection angle). The measurement diameter on the surface was approximately 1.1mm. Each measurement provided a uniaxial measurement. For each site, two measurements were taken and a mean value calculated for each pair.

The technique uncertainty is dependent on the quality of the D-S ring and thus how the X-ray beam interacts with the sample's crystal structure. The D-S ring and residual stress peak for T1 is shown in Figure 7.2. Peak fitting followed a Lorentzian technique, suitable for symmetric deflections [169]. The D-S ring was divided into 500 points and each point is transformed into stress, to shift the D-S ring from its stress-free position. The mean result of all 500 points gives the final value for residual hoop and axial stresses, accompanied by their standard deviation. It is noted that there is some oscillation in the signal intensity around the D-S ring circumference which may be due to a minor preferential orientation in the random polycrystal structure of the oxide (see Figure 7.2) [170].

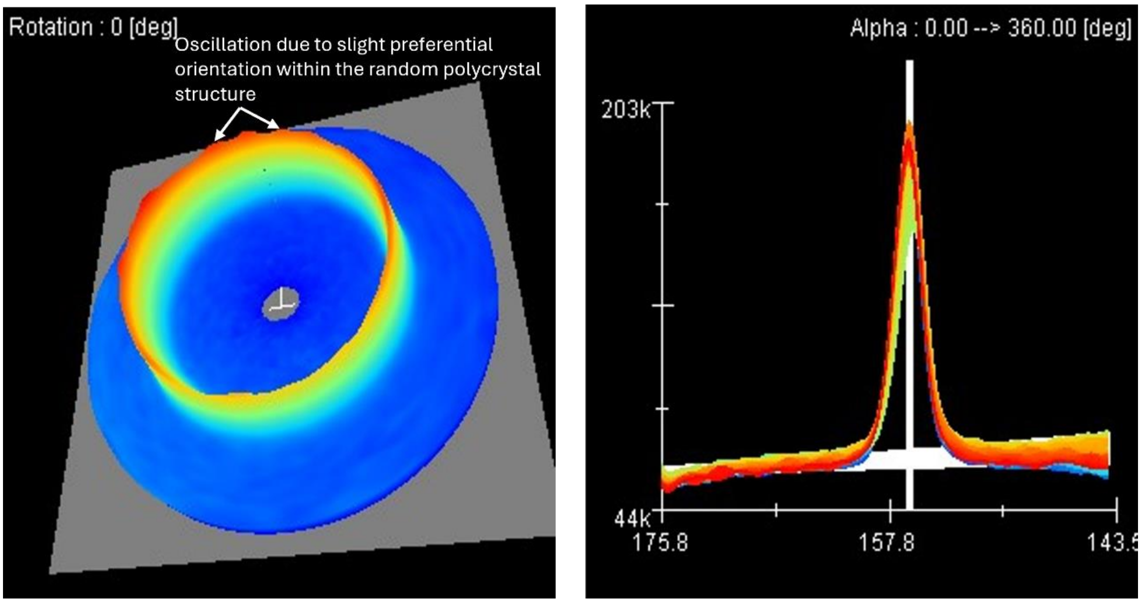

Figure 7.2: The diffraction Debye-Scherrer (D-S) ring (*left*) and peak at a diffraction angle at 156.396° (*right*) for the residual hoop stresses measured at (0°,71mm) on T1. (*Image generated by Chris Truman, University of Bristol*).

XRD was not only used to validate the stress state of the as-welded pipes, but also to obtain the lattice parameter, $\boldsymbol{\alpha}$, for corroboration with values used during temperature-dependent analysis of coefficient of thermal expansion. When a lattice parameter is used to predict a coefficient of thermal expansion which is expected to be more than $23.6 \times 10^{-6} K^{-1}$, as is the case for wüstite and steel (see 0), a maximum lattice parameter measurement accuracy of 0.06% is required [170]. Lattice parameter measurement is an indirect process which uses the sample's cubic structure $[\boldsymbol{hkl}]$ and interplanar spacing, $\boldsymbol{d}$, to calculate lattice parameter (see Equation 7.13). It should be noted that since the Bragg equation is used to calculate the interplanar spacing, the precision of the lattice parameter is dependent on $\boldsymbol{sin\theta}$ with the highest uncertainty for smallest angles (the Bragg angle in this case being $\boldsymbol{2\theta} = 156.396°$) [168]. During the experiments described in this work, the diffracted rays detected were emitted from the [211] atomic lattice plane. However, both the fact that a measurement was able to be taken from a mixed plane of odd and even Miller indices which added up to an even number, and the resulting calculation revealing a lattice parameter of 2.86Å, suggested that the inconsistent nature of the oxide adhesion meant that the ferritic steel substrate had been investigated (see Appendix 7).

$$\boldsymbol{a = d\sqrt{h^2 + k^2 + l^2}}$$

Equation 7.13

The tube, and its adhered oxide (an idealised assumption) is exposed to both mechanical loading and environmental stress during the manufacturing process. Layer theory [171] was used to plot the stress state of the oxide based on the **XRD** analysis on the steel substrate Figure 7.3. Although axial stress data is presented, hoop stress is used for application to the **AOSFD** as using 2D model data assumes no axial stress in relation to the oxide.

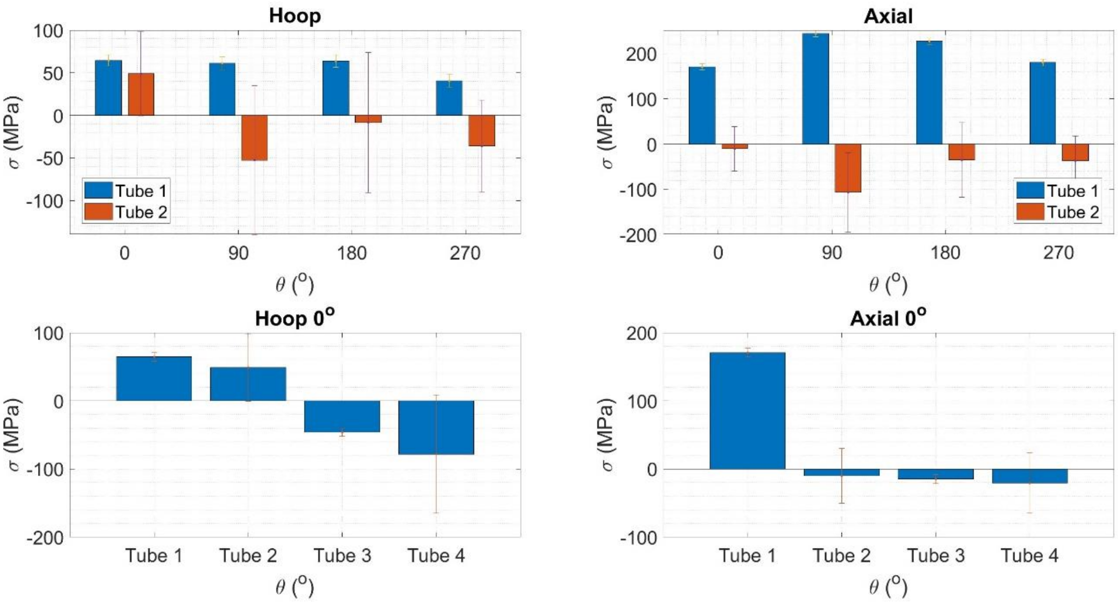

Figure 7.3: Hoop and axial stress, **σ**, state of full length (Tube 1 and Tube 2) and 25mm 15nb sectioned (Tube 3 and Tube 4) for oxide scale found on carbon steel conveyance tube samples before (Tube 1 and Tube 3) and after (Tube 2 and Tube 4) normalisation at weld (**θ** = 0°) and parent metal locations (**θ** = 90°, 180°, 270°).

Appendix 2: Oxide porosity measurements acquired using RGB image processing in open-source software ImageJ.